A

Ph.D. Thesis

on

DEVELOPMENT OF FLOW AND HEAT TRANSFER MODELS IN HYPERSONIC RAREFIED GAS DYNAMICS

Submitted by

SHESH NARAYAN DHURANDHAR

(Enrollment no: 14920034)

Under the Supervision of

Dr. Ankit Bansal

DEPARTMENT OF MECHANICAL AND INDUSTRIAL ENGINEERING

INDIAN INSTITUTE OF TECHNOLOGY ROORKEE

ROORKEE – 247667

UTTARAKHAND, INDIA

OCTOBER - 2019

Abstract: The Quantum Kinetic model used to predict the shock wave structure and the heat flux at the surface of the vehicle. The dsmcFoam solver is modified to include the Quantum Kinetic chemical reaction model for the hypersonic Martian re-entry. An open-source chemistry model based on Quantum-Kinetics (QK) is presented for the Direct Simulation Monte Carlo method. Chemistry modeling for the Martian atmosphere under rarefied reentry conditions are analyzed in this study. An eight-species (CO_2, N_2, CO, O_2, NO, C, N, and O) chemistry model is used to simulate the chemical reactions in the Martian environment. The QK model is based on the vibrational relaxation process of the molecule. A vibrational relaxation procedure for more than one vibrational modes is implemented to simulate various reactions in polyatomic molecules such as CO_2. The reaction rates are validated with previous data based on the total collision energy model of Boyd, Arrhenius rates as well as with the experimental data. The reaction rates obtained in this work are found to be in very good agreement with previous results for near-equilibrium and non-equilibrium conditions.

In this work, hypersonic reacting flow over the Crew Exploration Vehicle (CEV) is simulated using the Direct Simulation Monte Carlo method under the rarefied gas conditions. To account for high-temperature, non-thermodynamic equilibrium effects, the dsmcFoam solver is modified to include vibrational relaxation and chemical reactions. The chemical reactions are modeled using the Quantum Kinetics approach. This paper simulates the axisymmetric flow around the spacecraft in the Martian atmosphere. The chief constituent of the Martian atmosphere is CO2, which has four vibrational modes. We extend the relaxation and dissociation processes in the DSMC code to include all these modes. The chemical exchange reactions are considered only in the stretching mode of vibration. Our results show good agreement for the Earth's atmosphere with other published results for the Martian atmosphere.

Table of Contents

DSMC Application on The Martian Re-Entry Vehicle

List of Figures:

List of Tables:

Nomenclatures:

Acknowledgment:

I would like to thanks my

List of Publications:

Journals:

1. **Dhurandhar S. N.** and Bansal A., (2018) "Chemical Kinetics Study in Rarefied Martian Atmosphere Using Quantum Kinetics Model", *Physics of Fluids*, Vol. 30 (117104), pp. 1-9.
2. **Dhurandhar S. N.** and Bansal A., (2019) "Martian Entry Study with Direct Simulation Monte Carlo and Quantum Kinetics", *Journal of Spacecraft and Rockets*. (Under Review)
3. **Dhurandhar S. N.** and Bansal A., (2019) "Application and comparative analysis of Radiative Heat Transfer Models in predicting heat flux of a Pulverised Coal-Fired Furnace", *Journal of Heat Transfer*. (Under Review)

International Conferences:

4. **Dhurandhar S. N.** and Bansal A., (2016) "Energy deposition in supersonic flow past a hemisphere using OpenFOAM", *6th International Congress Computational Mechanics and Simulation, IIT Bombay, India.*
5. **Dhurandhar S. N.**, Dhankar P. and Bansal A., (2017) "Relaxation and Reaction Model for Gases in Rarefied Flows", *24th National and 2nd International ISHMT-ASTFE Heat and Mass Transfer Conference, BITS Pilani, Hydrabad, India.*
6. **Dhurandhar S. N.**, Kumar N. and Bansal A., (2019) "Comparison of Radiative Heat Transfer Models for the Martian Re-entry Vehicle", *9th International Symposium on Radiative Transfer, Athens, Greece.*
7. Kumar N., **Dhurandhar S. N.** and Bansal A., (2019) "Comparison of Radiation Models on Turbulent Non-Premixed flame DLR-A", *9th International Symposium on Radiative Transfer, Athens, Greece.*

Chapter 1
INTRODUCTION

Space vehicle entering the Martian atmosphere may achieve 5-10 km/s speeds. During the re-entry time, the peak temperature on the surface of the vehicle can reach 1500 K, and the shock layer temperature can be reached as high as tan's thousands kelvin.

1.1 Motivation and Background

When the space vehicle enters into any planetary atmosphere, it needs to pass through various regimes from the free molecular regime to the continuum regime. For over 40 years many countries have been sending robotic emissaries to Mars atmosphere sometimes successfully, often not to learn about the planet and whether it has ever been a habitat. In the past decades the NASA and European spacecraft in which three orbiter and three landers have been sent to the Martian atmosphere. The data from the spacecraft were patched together to get information about the Martian past and present, but, we still the human explorers are yet to reach the Martian atmosphere.

The space vehicle entering to the planetary atmosphere at high-speed requires to withstand large aerodynamic forces, as well as significant heating. When the vehicle enters the planetary atmosphere at hypersonic speed, the shock layer formed in front of the vehicle due to the collision of the molecules. In the collision process, the kinetic energy of the molecule is dissipated into the thermal energy of the molecules. The molecular species have external energy in the form of translational energy (due to random motion of atoms), and internal energy in the form of rotational energy (due to angular motion of the particle around the centroid), vibrational energy (due to atom in the molecule are in the periodic motion) and electronic energy (due to the motion of the electron within the molecule). At lower entry speed the shock layer is relatively small and the variation in temperature along the shock layer is less and, only rotational and translational modes of the gas-particle are exited. In the hypersonic shock layer, the vibrational modes of the molecules also become excited and the chemical reactions (dissociation and exchange) takes place. The Quantum Kinetic chemical reaction probability depends upon the translational and vibrational energy state of the colliding particles.

The Navier-Stokes equation which simulates the flow in the continuum regime failed to predict flow at rarefied gas flow conditions. The governing equation which relates the shear stress and the heat transfer to other variables breaks down in the transition regimes, there is the situation when the average distance traveled by the particle between two consecutive collisions increased. The Boltzmann equation of kinetic theory describes the flow in the continuum, transition, and rarefied gas regimes. The Boltzmann equation is integro-differential type equation proposed by Boltzmann in 1872, which can not be easily solved by analytically or numerically method. Bird introduced a method to simulate the particles named as DSMC (Direct Simulation Monte Carlo) method, which can solve the Boltzmann equation.

1.2 The re-entry flow regimes:

When the space vehicle enters into the Martian atmosphere, it undergoes not only different velocity regimes, hypersonic, supersonic, and subsonic but also undergo different flow regimes, free molecular flow, transition and continuum regimes.

There are three different flow regimes can be differentiated by the Knudsen number (k_n). The Knudsen number can be defined as the ratio of the mean free path (average distance traveled by the particles between two consecutive collisions) to the characteristic length of the system.

$$k_n = \frac{Mean\ free\ path\ of\ the\ collision}{Characteristic\ length\ of\ the\ system}$$

In the free molecular flow regime, the *Kn* varies from 10 to ∞. In this type of flow, the collision between the gas particles is very less as the average distance between the particles is very. The flow regimes can be described in three different regimes which are a continuum, transition, and free molecular flow regime. In the continuum flow regime, the gases are dense enough. This situation occurs at the highest altitude when the atmospheric air interacts with the space vehicle. In these regimes, the collision between the reflected particle from the surface and free stream particles are not likely to occur.

In transition regimes, the flow *kn* varies from 0.01 to 10. In this regime, neither the continuum assumption works not the free molecular flow assumption works. The continuum assumptions break down when the average distance traveled between the particles between two consecutive collisions is high compared to the characteristic length scale of the system. In this regime, the flow described by the Boltzmann equation of kinetic theory, which describes the flow in all three regimes. This situation occurs when the space vehicle enters deeper into the atmosphere. In this regime, the collision between the reflected particles from the surface and the free stream particles cannot be ignored. The aerodynamic forces on the vehicle and the heat flux at the surface of the vehicle increase rapidly with a decrease in the altitude and causing the large changes in the aerodynamic characteristic of the vehicle compared to the free molecular flow regime. In this regime, the strong shock waves are formed in front of the space vehicle, and in that situation, the thermodynamic and non-equilibrium chemical reactions become important to predict the accurate heat flux and pressure force on the surface of the vehicle. The degrees of freedom of the gases at that altitude becomes excited and the chemical dissociation, exchange and ionization reactions can take place [1], which leads to reduction in the bow shock temperature and the flow energy.

The value of *kn* varies from 0.01 to 0, in the continuum flow regime the average distance traveled by the particle between two consecutive collisions is very less. The Navier-Stokes equation is valid for this type of flow and in this type of flow, the gas particles are assumed dense enough that there is no gap between the particles (continuous flow). In this type of flow generally, the *kn* value ranges from 0 to 0.01. In these regimes, the flow is described by the temporal and spatial variation of properties represented in the macroscopic form (pressure, temperature, velocity, pressure and, density)

In the microscopic model or the molecular model, the gas particles are treated as the collection of particles where the position, energy, and velocity of the particles are described individually. Boltzmann equations

are required to solve for such type of system [2]. The Boltzmann equation can be analytically solved for the collisionless flow, where the *Kn* tends to infinite. The analytical solution of the Boltzmann equation for rarefied hypersonic flow problem is available, as this type of problem involves complex physical effects, like thermal radiation, chemical reactions, and which have not been incorporated in the basic Boltzmann equation. However, the analytical solution for the Boltzmann equation solution for the simple molecular models, one independent macroscopic variable and flow with small disturbance is possible. The Molecular Dynamics method uses the molecular properties of the species to solve the Boltzmann equation [3,4].

1.3 Radiative Heat Transfer in Martian Entry Vehicle Overview

The modeling of shock layer radiation is a very complicated task and requires a lot of computational time. Even for the Earth's atmosphere re-entry, the shock layer radiation phenomena is not well predicted. All the previous studies available on the radiation models are based on some assumptions to simplify the study and reduce computation cost. Anderson [5] presented a detailed survey of the radiation shock layer and found an important aspect of the design of space vehicles. The earliest investigation of radiative heat transfer study was done for the Lunar return vehicle. During the Apollo mission, various lots of resources were used to capture the aerothermal phenomena around the space vehicle. These predictions were supported by a number of shock-tube experiments and two flight tests (Flight I and Flight II). The main objective of the experiment was to gather sufficient data for the development of the theoretical model and calculate the heat transfer due to convection and radiation. The theoretical models [6,7] used for the comparison of data from the Fire II experiment, from the study it was found that the shock layer highly dissociated and the N and O were the most dominated species in the radiation field.

Later the planet like Venus [8], Mars [9–11], Jupiter [12–14], Neptune [15] and, Titan [16,17] atmosphere were explored for the possibility of aerocapture. Recently the mission of reentry into Earth's atmosphere returning from the Mars mission took lots of attention.

Sutton [8] studied the fully coupled radiation model to flow around the entry probe. In that study, the equilibrium chemistry model with non-gray radiative transport, and laminar and turbulent boundary layer used. In contrast to Earth's atmosphere, which consists of N_2/O_2 species the Venusian atmosphere contains 97% CO_2 and 3% of N_2 by volume. In the shock layer, which consists of CO_2 and N_2 species, the significant radiation takes place, even at the lower temperature. The main radiation source is CO (4+) band system in near ultraviolet, and CN (Violet and Red) and system, and C_2 swan band and radiation form the atomic species C and O. The radiative heating captured by the Venus aerocapture vehicle predicted 10 times higher than the Earth's atmosphere. Mars and Venus's atmosphere is very similar. A number of studies done [10,11,18,19] for the Martian aerocapture vehicle under the different entry conditions. In the Martian and Venus atmosphere where the CO2 is high, the radiative heat load is significant in the front as well as backside of the re-entry vehicle [18,20].

The Titan has an atmosphere of N2 and methane in a small amount. In the shock layer, the cyanogen radical (CN) is formed, which is the very strong radiator. The radiative heat transfer due to radiation is found to be five times the peak convective heat transfer in the Titan atmosphere using the three-

dimensional axis symmetry coupled radiation with CFD solver [17,21]. The radiation heating form the CN molecules was the main concerned during the ESA's Huygens probe entry into the Titan atmosphere, and the radiative heat flux predicted from the probe was more than 90 W/cm^2, which was more than two times the convective heat flux [22].

Recently, a lot of studies done on the radiative heat transfer, in relation to the Stardust vehicle [23–27] and to the Crew Exploration Vehicle [28,29]. Stardust is the fastest man-made reentry vehicle, which can achieve a maximum of 12.8 km/s speed. The stardust was launched in February 1999 and it returned to earth surface in January 2006 collecting dust and sample from the Comet wild 2. The coupled CFD-radiation carried out by Olynick et al. [24] for the prediction of the radiative heat load on the space vehicle. The radiative code was loosely coupled with the Navier-stokes and the material thermal response code, and the integrated radiative heat load was predicted was 7% of the total heat load. Bose et al [30] carried out the theoretical and experimental study for the shock layer radiation from the NASA Orion CEV returning from the Lunar and entering to the Earth's atmosphere. The spectrally resolved radiation intensity comparison made with the experimental work (Electric Arc Shock-Tube) and found that the peak heating radiative component is nearly equal to the convective heat load. The shock layer thickness predicted for the CEV was, large which results in large radiative heat load.

Radiative energy can travel the large distance, the energy from the shock layer is likely to escape from radiation energy and get absorbed in the outside region resulting in cooling the shock layer. The emitted energy may change the flow properties, resulting in cooling the shock layer and overall reduction of convective heat load. The reduction in the heat load in convective and radiative heat load depends upon the magnitude of coupling. The hypersonic flow around the spacecraft can be treated using a coupled or uncoupled approach. In the uncoupled approach, the flow field is assumed to be adiabatic and the effect of the radiation is not considered, the peak heat inside the shock layer may get reduced when considered radiation. A considerable amount of heat may escape from the shock layer due to radiation, resulting in an overall reduction in convective and radiative heat load [7,31]. However, the uncoupled approach requires very less computational time. Due to high the computational time the many researchers, prefer to uncoupled the solution method, which gives the estimation of the radiative flux onto the surface of the spacecraft.

In the coupled approach, the RTE (Radiative Transfer Equation) needs to solve along with the flow solver to account for the heat transfer by radiation mode and radiative cooling effect in the shock layer. The coupled radiative models are computationally very expensive, therefore; simple and approximate models used in most of the studies. A loosely coupled approach, in which radiative transfer equation not solved in every iteration of the flow, but the radiative properties are only updated after a number of flow iterations. However, coupled radiation study not considered in this work due to low computational resources.

In optically thin radiation case, the coupled studies are very much simplified, that requires the emission evaluation at each point in the flow field. The interaction of the radiation with the flowfield can be neglected, this approach was used by Wright et al. [21]. The result from this approach it was found that

the radiative heating rates were reduced by a factor of two and the convective heat load is reduced by 30% in the coupled approach for the Titan aerocapture mission. The loosely coupled methodology was used by Pace et al. [32]. The Nonequilibrium Air Radiation code (NEQAIR) coupled with the CFD code named Data-Parallel Relaxation (DPLR), and this coupled scheme was applied to the CEV returning from the Lunar. The result from the simulation was found that the radiation decreases the post-shock temperature, and shock standoff distance, and reduces the convective heat load to the spacecraft.

The presence of ablation material at the boundary of the spacecraft also affects the radiative transfer on the spacecraft. The heat shield of the spacecraft is mostly made of carbon-phenolic or carbon-ceramic materials, that decays through the pyrolysis process and produce a large number of gaseous products at the boundary surface. The product of the ablation of the TPS are found are CO, C_3, and other trace species; including HCN, CN, C and H [24]. The CN molecule, which is the most radiating species, found in the arc-jet experiment [33]. The ablation products concentrations are generally higher in the cooler boundary layer region; therefore, the ablation products may have higher absorption than emission. This results in lowering the radiation flux in boundary and large convective flux due to the hotter boundary layer. The carbon monoxide CO (4+) is the most important absorbing species among the ablation products.

Hoshizaki et al. [34] and Coleman [35] showed that absorption by ablation products may reduce the radiative heat flux on the spacecraft nearly a factor of two. Sutton et al. [36] found a 10 to 20% reduction in the attenuation of surface radiation due to ablation products for the Venus pioneer mission. Moss et al. [37,38] observed that the higher heating rates in-flight data for the Galileo missions and the Pioneer-Venus compared to prediction data. This disagreement in the predication data and in-flight data was due to the ablation that was not considered in the prediction work. This is important to incorporate the ablation and radiation model in the flow solver for the analysis of shock layer.

NASA is currently designing Crew Exploration Vehicle (CEV) as a replacement of space shuttle, for a manned mission to the international space station [39]. The CEV will be used as a command module for returning Astronauts to the Moon and will work as an Earth re-entry vehicle when returning from the moon or Mars.

1.4 Hypersonic Chemical Reaction Models

The study of a non-equilibrium chemical reaction is important for the rarefied hypersonic entry flow to understand the heat transfer from the vehicle. During the re-entry process, the temperature around the spacecraft can not be represented by the single temperature. Due to the presence of a high density of gas species, high pressure and, high temperature the prediction of the shock layer around the spacecraft becomes a very complicated process. A number of studies focused on the problem of high-temperature chemical kinetics in Earth's atmosphere [40–44] as well as another planetary atmosphere [9,10,45].

Early, the bird [46] introduced the gas chemical reaction model for the DSMC method, which uses the molecular properties and, molecular energy to model the gas-phase chemical reaction. The theoretical

and experimental model supported the theory of modeling gas-phase chemical reactions using the molecular property of the gases. Classical collision theory, which was an established model for the calculation of chemical reaction rates, extended to use the chemical reaction probability for the bimolecular chemical reaction. The model was extended to termolecular reaction; the important termolecular reaction in high temperature is recombination reaction.

The Boyd [47] used the DSMC model to model chemical reactions in a rarefied gas environment, the coupling of the vibrational energy of the molecule and the dissociation reaction is investigated. A new steric factor was introduced which includes the vibrational energy of the molecule for dissociation reaction. The result was compared for reentry blunt-body along the stagnation line and found that the surface quantity and the flow properties significantly affected by the steric factor. The calibration in the steric factor is required through experimental or theoretical data.

A chemical kinematics model implemented by Candler [48] for a mixture of the CO_2-N_2 gas for the 2D CFD method. The two-temperature model for eight chemical species presented for thermochemical non-equilibrium study. The Navier- Stokes equations expanded to include the multiple chemical species and the energy modes. The thermal non-equilibrium observed due to fast vibrational relaxation of CO_2 and the CO molecules creates high non-equilibrium at a higher energy level at which CO dissociates.

Two separate experiments were conducted by Fishburne et al. [49] to predict the reaction rate for the reaction for the formation of CO_2. In the first experiment the mixture of CO and O_2 was introduced into shock tube and in the second experiment high-temperature mixture of CO_2, CO and O_2 passed through supersonic expansion nozzle. The study focused to calculate predict the chemical kinetics for the Martian entry vehicle.

Gallis et al. [50] proposed a chemical kinetics model that predicts the chemical reaction rate for equilibrium and non-equilibrium reactions in the upper atmosphere. The proposed model was in good agreement with the Arrhenius rate for near-equilibrium condition and experimental model and theoretical models which are far from equilibrium. This model was summarized in the report by Gallis et al. [51] and equilibrium reaction rates calculated without using the macroscopic reaction-rate information. The model is capable to predict the reaction rates for the arbitrary non-equilibrium reaction. This model was in good agreement with the Park's model for near-equilibrium condition and for far-from-equilibrium condition difference in the result found to be very high.

The non-equilibrium thermochemical model was developed by Park et al. [10] for the CO_2-N_2 mixture for the prediction of radiative heat flux on the surface of reentry vehicle entering into the Martian atmosphere. The prediction of radiative heat flux was consistent with the experimental data. The dissociation of CO_2 and the approach of vibrational temperature towards the translational temperature was observed to be very fast behind the shock wave. The chemical equilibration becomes slow due to the slow dissociation of the CO molecule.

The physical model for dissociation and recombination reaction and phenomenological model for chemical exchange reaction is presented by Bird [52], the models are based on the vibrational energy states of the colliding molecules and do not require the experimental-based data. The model is then applied to hypersonic reentry vehicles and found a good agreement with the TCE model.

The Kinetic-Theory approach was extended by Liechty et al. [53] by including the charged particle reaction and electronic energy levels of the particles. The extension includes the ionization reaction, endothermic and exothermic reactions with charged particles, exothermic associative ionization reactions. These model does not require the macroscopic reaction rates to calibrate adjustment parameters, instead, they use the energy level of the colliding molecules to predict the reaction probability. The predicted reaction rates were in good agreement with the Arrhenius reaction rates for the near-equilibrium conditions.

Recently Gimelshein et al. [54] used Total Collison Energy to model chemical reactions in the rarefied gas environment, the models include the internal degrees of freedom and detailed balance for chemical reaction and discussed some numerical limitation of the model. The numerical problem with the TCE model is that sometimes the reaction probability becomes more than one due to the total collision cross-section, in this case, the equilibrium reaction rate coefficient predicted by the DSMC method underpredict the reference coefficient.

The aerothermal study for the Mars entry mission is reviewed by Wright et al. [19]. The heating of the surface of the vehicle due to convective heat, radiative heat from the shock layer and localized heat due to penetration or other effect are reviewed. The flight data from Viking, Pathfinder mission are used for the validation of the model, and an argument is presented to obtain additional flight data. Presently there is no validation model to predict the shock layer radiation for the Martian atmosphere reentry vehicle, and similarly for the Earth's atmosphere. The uncertainty in the prediction of convective heat flux was due to surface catalysis in a CO_2 environment.

1.5 RTE Solution Methods

The Radiative heat transfer calculation between the surfaces separated by a vacuum or transparent medium is comparatively easy when compared with the presence of absorbing or emitting medium. Most of the engineering problems where the surfaces are separated by the absorbing or emitting medium. In the rarefied environment, the space between the shock layer and the surface of the spacecraft consisted of the gases. The Radiative transfer equation should incorporate all the gas radiation at all the atmospheric conditions. The solving of the RTE for three-dimensional flow and incorporating all the gas radiation is computationally very expensive. Most of the researchers used a simple one-dimensional problem and applied the detailed line-by-line solution method or used the full geometry with an approximate spectral treatment method depends upon the problem specified. The standard tangent slab approach was applied by Wright et al. [21] for the prediction of radiative heat flux on the Titan aerocapture aero heating problem. The tangent slab method calculates the radiative heat flux at the stagnation point, however; this method yields the conservative value of heat flux as this method assumes a layer infinite width and neglects the curvature effect of the boundary layer.

1.6 Spectral Models for Radiative Properties

1.7 Project Objective

The objective of this project is to development of the DSMC code for the rarefied hypersonic Martian re-entry vehicle, and study the chemical and thermal non-equilibrium. In this study the flow around the hypersonic re-entry vehicle is analyzed, the heat flux and the aerodynamic pressure on the surfaces of the vehicle are predicted. The initial flow condition is defined in the form of free-stream temperature, velocity, species number density, and pressure.

In the present study, the Quantum Kinetic chemical reaction model is used to calculate the non-equilibrium chemical reaction during the hypersonic re-entry. The model is applied in the regime where the mean free path for the particle is high and continuum solver (Navier-Stokes) gives a poor approximation.

The DSMC method aimed primarily to use in the transition regime, in the transition regime the aerodynamic heating and the pressure load on the surface highly depend on the rarefaction of the atmosphere.

The main objective of the thesis is described:

1.
2.
3.
4.
5.

1.8 Thesis Outline

Chapter 2 presents an exhaustive review of the literature in the broad area of the DSMC model and the implementation of the DSMC for the rarefied gas study. The collision models in the DSMC discussed the application of the DSMC chemical reaction model in different planetary atmosphere entry discussed. The literature on the radiative heat transfer model for the rarefied gas environment discussed.

Chapter 3 presents the basic DSMC model and implementation method for the vibrational relaxation process in DSMC. The Quantum-Kinetic chemical reaction model explained for the Martian atmospheric environment. The chemical reaction rates for the equilibrium and non-equilibrium condition calculated and presented. The procedure for modeling chemical dissociation, endothermic exchange, and exothermic exchange reaction explained. The procedure of detail balancing of various energy modes explained in detail.

Chapter 4 presents the application of the DSMC Quantum-Kinetic chemical reaction model in the Earth's atmosphere. The result for the Earth atmospheric model compared with the MONACO code for the validation of the code. The temperature contour, convective heat flux, species number density presented.

Chapter 5 presents the application of the DSMC model for the Martian re-entry vehicle. The DSMC model is applied over the two-dimensional Crew Exploration Vehicle. The species number density, pressure, velocity and three (translational, rotational, and vibrational) modes of temperature plot presented along the stagnation line. The temperature, mass fraction contour plotted for the two different entry velocity case. The convective heat flux on the surface of the CEV presented.
Chapter 6 presents the radiation models for the rarefied gas environment. The procedure for the implementation of the Imaginary Plane Model in OpenFOAM software is discussed. The spherical harmonic model (P_1) explained with and without the presence of the participating gas. The spectral model (Line-by-line and k-distribution) for the non-gray gas environment discussed.

Chapter 7 presents the application of the radiation model in the rarefied gas environment. The result obtained using the chemical kinetic model used to calculate the stagnation point radiative heat flux. The one-dimension line-by-line model used to calculate the radiative heat flux on the stagnation point. The k-distribution method used to calculate the radiative heat flux. Both the method uses the radiative properties of the gas mixture to calculate the radiative heat flux.

Chapter 8 highlights the summary of the research findings from the simulation. Outline specific conclusions are drawn from the simulation and suggest ideas and directions for future research.

Chapter 2
LITERATURE REVIEW

Palharini et al. [55] used DSMC solver to check the ability of the code for the low and high speed non reacting flows in simple and complex geometries. They applied the dsmcFoam solver for the case of Mars Pathfinder probe, and the results were in good agreement with the previous experimental and numerical data. Casseau et al. [56] used a two-temperature CFD (computational fluid dynamics) solver for the spacecraft re-entry analysis. They developed a new two-temperature CFD solver, *hy2Foam*, within the framework of the open-source CFD platform OpenFOAM for the prediction of hypersonic reacting flows. This solver, *hy2Foam*, has the capability to model vibrational-translational and vibrational-vibrational energy exchanges in an eleven-species air mixture.

White et al. [57] implemented the pressure-driven, implicit boundary conditions in an open source direct simulation Monte Carlo (DSMC) solver. DSMC simulations are conducted for gas flows with varying degrees of rarefaction along the micro-channels with both one and two 90-degree bends, and results are compared to those from the equivalent straight micro-channel geometry. Scanlon et al. [58] developed an Open source, parallel DSMC code to simulate 1-D, 2-D and 3-D complex problem. The code has capability to perform unlimited parallel processing and can be used in both steady and transient condition. A 3-D simulation was performed for the hypersonic flow over the flat-nosed cylinder for Kn 0.0474, Mach number 5.37 and temperature of the cylinder 300K. Results were compared with the analytical and experimental data, and found to be in good agreement. Dongari et al. [59] introduced a new power-law (PL) wall-scaling approach to investigate the nonlinear flow physics in the near-wall regions . This model incorporates Knudsen layer effects in near-wall regions by considering the boundary limiting effects on the molecular free paths. They also reported a new DSMC simulation results covering a wide range of Knudsen numbers and accommodation coefficients.

Kumar [60] conducted a conjugate thermal analysis of a typical reentry space capsule by coupling aparticle-based flow solver to a material thermal response solver. A 2-D parallel DSMC solver , capable of solving multispecies gas flows, is developed to solveFlow solution in the transitional flow regime. A one-dimensional thermal response solver is validated against the available data in the literature and found to be in good agreement. Chinnappan and Kumar [61] proposed a new computational model to conduct gas-granular flow dynamics within the framework of the direct simulation Monte-Carlo method. In this model, the regular procedures of the DSMC method is used to model the gas–gas collisions.

Ge et al. [62] proposed a spherical harmonics (PN) method, orders of P_N. The set of N(N+1)/2 three-dimensional second-order elliptic PDEs formulation and their Marshak boundary conditions for arbitrary geometries are implemented in the openFoam. To verify the model, four test cases with strongly varying radiative properties, including a 1D slab, a 2D square enclosure, a 3D cylindrical enclosure, and an axisymmetric flame, were analyzed. The results are compared with exact solutions and solutions from the photon Monte Carlo method (PMC). Ren et al. [63] applied a Photon Monte Carlo (PMC) method coupled with a line-by-line spectral model for the analysis of reacting swirling flow in an industrial gas turbine burner. Roy et al. [64] coupled the photon Monte Carlo (PMC) method to the multiphase spray combustion solver with a focus on resolving radiative heat transfer in the combustion simulations, and applied it for the simulations of high pressure Diesel spray combustion.

Ren and Modest [65] proposed a hybrid scheme for wavenumber selection. In this scheme, line by line method is coupled with the monte corlo method. The accuracy of the new method is established and its time requirements are compared against the well stablished previous methods.

Singh and Schwartzentruber [66] proposed a model ,based on surprisal analysis, for the non-equilibrium vibrational and rotational energy distributions in nitrogen. The model is utilizing data obtained from the direct molecular simulations (DMSs) of promptly heated nitrogen gas using an ab initio potential energy surface (PES) . Schwartzentruber et al. [67] summarized implementation of the DMSC method on the numerical simulation of dilute gas flows. DMS algorithms are detailed, and a number of new results relevant to the hypersonic flows are presented along with a summary of other recent results in the literature.

Feldick et al. [68] developed a one-dimensional tangent slab radiative transport solver to model radiation in non-equilibrium hypersonic flows. The results are compared with NEQAIR, an established radiation solver, and solver is found to be efficient, and also allow direct coupling to hypersonic CFD codes.

Li *et al.* [69] applied the DSMC Electronic Excitation Mode to Tangent Slab Radiation Calculation of Hypersonic Reentry Flows. They implemented excited levels of atomic N and corresponding electron impact excitation/de- excitation and ionization processes in DSMC. The model is then appied to the Starduct 68.9 km re-entry vehicle, and the found that when excitation models are included, flow has an observable change in the ion number densities and electron temperature. The radiatve heat flux at the stagnation point foiund to be 20 % different, were compared with Quasi Study State method.

Sohn et al. [70] developed the new databasing schemes for advanced radiation calculations of hypersonic nonequi-librium reentry flows. Since the flow is in nonequilibrium, a rate equation approach including both collisional and radiatively induced transitions is used to calculate the electronic state populations. The absoptiobn and emission coefficient of atomic O and N compared with Nonequilibrium Air Radiation (NEQAIR) and found good accuracy of the database. However; for diatomic species N^{+}_{2} , NO, N_2 and O_2, slight differences in the results observed.

Bhagat et al. [71] numericaly investigated the effect of Knudsen layer in high-speed flows in a rarefied flow regime. They reformed the conventional CFD solver based on the effective mean free path model to expand the validity of the Navier-Stokes-fourier requations or application in the slip-transition flow regime. The results (DSMC) were compared for the location of an oblique shock around the flat plate is accurately captured and overall, the Knudsen layer incorporation has exhibited good agreement with the DSMC.

Gijare et al. [72] studied the effect of the Knudsen layer on the surface heat transfer for the hypersonic flow applications in the slip and early transition flow regime. They investigated the high speed flow over a wedge and a circular cylinder for wide range of Knudsen numbers. The results were compared with the DSMC data, and found very good aggrement for Knudsen numbers, Kn=0.05 and 0.25.

Kumar et al. [73] developed a new multi-species, polyatomic, parallel, three-dimensional Direct Simulation Monte-Carlo (DSMC) solver named Non-equilibrium Flow Solver (NFS) for applications related to rarefied gas flows. The results for 2D and 3D external flow were compared with experimental data and those obtained in other numerical works and found very good agreement.

Gavasane et al. [74] analyzed the effect of rarefaction on the flow properties and the separation of the flow in the rarefied gas environment using the DSMC technique. They studied the flow separation, circulation and re-attachment of step flows. The Knudsen number (Kn) range selected to covers the slip and transition regime are from 0.0311 to 13.25.

Chapter 3
DSMC MODULES

3.1 The Boltzmann Equation

The Boltzmann describes the flow in all regime continuum, continuum-transition, and free molecular regimes. The Boltzmann equation is the integro-differential type equation proposed by Boltzmann in 1872. The limiting case of this equation yields for the continuum regimes where the mean free path is very small and the collisionless flow (free molecular flow). The Boltzmann equation can be written as

$$\frac{\partial}{\partial t}(nf) + c.\frac{\partial}{\partial r}(nf) + F.\frac{\partial}{\partial c}(nf) = \int_{-\infty}^{\infty}\int_{0}^{4\pi} n^2\,(f^* f_1^* - f f_1)\, c_r \sigma d\Omega dc_1$$

Where n is the number density of species and f represents the velocity distribution function, c is the molecular velocity, c_r is the relative velocity of the species, F represents the external force applies to the species, the superscript (*) represents the post-collision properties, f and f_1 represents the velocity function of two different types of molecules of class c and c_1 respectively, σ represent the collision cross-section, t time and Ω represents solid angle.

3.2 The Direct Simulation Monte Carlo Method

Bird developed the Direct Simulation Monte Carlo method in 1960 for the simulation of the flow in the kinetic scale [46]. During the year between 1960 and 1980, the DSMC method becomes one of the most important methods to simulate the hypersonic rarefied flow in the transition regime. The DSMC method is based on the physical concept of rarefied gases, and on the physical assumption that forms the basis for the derivation of the Boltzmann equation [2]. The DSMC method and Boltzmann equations are based on the classical kinetic theory of the gases, and the DSMC method is not directly derived from the Boltzmann equation.

In the DSMC model, each particle (molecule/atom) has velocity, position, and internal energy. The state of the particle modified and stored with time, as the particle initialized, move and participate in a collision, and interact with the boundary or surface inside the domain. The Direct Simulation Monte Carlo (DSMC) method is one of the most powerful methods for simulating the rarefied gas flow [75].

The DSMC method uses the kinetic theory of gases to simulate the flow at the molecular level. In this method, the motion of particles may be decoupled from particle-particle collision over a time step smaller than the mean free time between collisions. In the computational domain, the moving molecules/particles are tracked, and collisions and collision-generated transitions (rotational, vibrational relaxation as well as chemical reactions) are treated in a probabilistic manner. This method can precisely evaluate non-equilibrium gas behavior. Instead of complex deterministic procedures, the DSMC method employs stochastic tools that lead to higher accuracy and lower computational time. In the DSMC method, each simulated particle represents a large number of the real particle, as it is a time-consuming process to

consider all the real particles inside the domain and simulate collision. The simulated particle can vary from the thousand to million depending upon the flow problems.

The Direct Simulation Monte Carlo is the solver for the rarefied gas dynamics in the OpenFAOM software. Space vehicles enter into planetary atmospheres at hypersonic speed. NASA has carried out a number of missions to various planets of our solar system. Out of many missions to nearby planets, the Martian entry has captured a lot of importance. The typical low-density rarefied environment encountered during atmospheric entry of a spacecraft cannot be analyzed with the continuum models. In the rarefied environment, the constitutive relations for shear stress and heat transfer are not applicable. Furthermore, during high-speed atmospheric entry, a high-temperature shock layer is formed at the front of the spacecraft. The gases in this the shock layer undergo various types of chemical reactions to form atoms and ions. The presence of various gas species together with high temperatures leads to an extremely high heat transfer environment.

The study of non-equilibrium chemical reactions is very important for understanding the heat transfer to a hypersonic re-entry vehicle in the rarefied gas environment. Insufficient and inaccurate results may lead to inaccuracy in the design of a spacecraft. A number of studies have focused on the problem of high-temperature chemical kinetics in the Earth's environment [40–44] as well as other planetary environments [10,45]$^{-10}$. The Martian atmosphere mostly comprises of CO_2 with a small fraction of N_2. Thus, the chemical kinetics problem in the Martian environment at high temperatures is very different from that of the Earth's atmosphere[1]. During entry into the Martian atmosphere, the temperatures may reach as high as 8,500 K[76]. The dissociation of diatomic N_2 and triatomic CO_2 gases are two of the most important chemical reactions in the shock layer of a Martian atmospheric entry vehicle.

The Direct Simulation Monte Carlo (DSMC) method is a powerful method for simulating the rarefied hypersonic flow[75]. The DSMC method simulates the flow at the molecular level by using the kinetic theory of gases. In this method, moving particles/molecules are tracked across the computational domain, and collisions and collision-generated transitions (rotational, vibrational relaxation as well as chemical reactions) are treated in a probabilistic manner. The method can treat non-equilibrium gas behavior accurately. As opposed to the Molecular Dynamics (MD) method that employs complex deterministic procedures, the DSMC method employs stochastic tools that increase the accuracy of the results and decrease the computational time.

The high-temperature low-density conditions during spacecraft entry into an atmosphere are far from thermodynamic equilibrium; it is not possible to represent the flow conditions with a single temperature. The temperature around the vehicle depends on different kinetic conditions (rotational, vibrational and electronic relaxation/excitation of molecules) and various chemical reactions. The internal energy transfer between various modes is usually implemented with the phenomenological model introduced by Borgnakke and Larsen[77]. In this model, the probability of an inelastic collision determines the rate at which energy transfer takes place between translational and other internal modes. At the high-temperature hypersonic flow of gas mixture the energy exchange between the translational and other internal modes of energy violets the equilibrium when the characteristic time of kinetics and gas dynamics process is comparable. The non-equilibrium effect at this condition becomes important and for the correct prediction of the kinetics and gas-dynamic, the non-equilibrium process should be considered. At high-temperature shock waves, the

equilibrium achieves very shortly between translational rotational degrees of freedom compared to the translational end vibrational degrees of freedom[78]. Therefore

$$\tau_{rot} \ll \tau_{vib} \ll \tau_{react}$$

Here τ_{rot} , τ_{vib} and τ_{react} respectively are relaxation time for rotational, vibrational degrees of freedom and the characteristic time for the chemical reaction.

The high temperature in the shock layer of a hypersonic spacecraft leads to dissociation, ionization and exchange reactions and leads to chemical non-equilibrium. Due to low density in the rarefied media, the reaction rates are generally low and finite rate chemical kinetics need to be considered. To consider the effects of chemical reactions in the gas mixture, a number of models have been proposed for the DSMC method[43,44,79–83]. The Total Collision Energy (TCE) is a model based on the modified Arrhenius rate coefficient, and utilize quantities derived from macroscopic parameters. The model converts the conventional Arrhenius rate coefficients (defined in terms of macroscopic gas temperature) to collision probabilities based on collision energy at the microscopic level using the uses equilibrium kinetic theory. The TCE model was later extended to take into account the coupling between the vibrational energy and the collision-induced dissociation[84,85]. Boyd *et al.* applied the extended TCE model to calculate the exchange, dissociation and recombination reactions in rarefied gas flow conditions for the Earth's atmosphere[83]. Dhurandhar *et al.* used the TCE model to study the dissociation of CO under rarefied conditions[86].

For the particle-based DSMC method, a molecular level chemistry model is desired that estimates reaction rates using the kinetic theory and fundamental molecular properties only. Recently, Bird proposed the Quantum-Kinetics (QK) reaction model based on the fundamental properties of colliding particles, i.e., the total collision energy, the quantized vibrational levels, and the dissociation energies. The model connects the energy exchange processes with chemical reactions. This model has only a limited dependence on the macroscopic data and does not require the gas to be in a state of near thermodynamic equilibrium [82]. In contrast to the TCE model, the QK model is based on the quantum vibration theory.

In the original QK model, there was a problem with the detailed energy balance among rotational, translational and vibrational modes. It was observed that the three temperatures were not in equilibrium after the chemical exchange reactions with finite activation energy. Bird corrected this problem by implementing the detailed energy balance process[80], which ensures that the pre- and post-reaction distributions are matched. Liechty et al.[45] used the modified QK model to predict reaction rates in equilibrium and non-equilibrium conditions. In the equilibrium case, the temperature of the system does not change, as the post-reaction energy exchange is not implemented. On the other hand, in the non-equilibrium calculation, the system undergoes energy exchange, resulting in a change in the temperature of the system. They further extended the QK model by including the electronic energy transition. Furthermore, Liechty *et al.* studied the reactions between the charged particles and compared their results with the analytical results and Arrhenius rates.

Scanlon *et al.* employed the Quantum Kinetic model in the DSMC method to study chemical reactions in rarefied gas atmospheres[43]. They implemented this model into an open-source DSMC solver, OpenFoam, and compared their results for exchange and dissociation reaction rates with the analytical and experimental shock tube results.

In this paper, we study the chemical reactions in the Martian atmosphere under rarefied gas conditions. We have implemented the modified QK model in the *dsmcFoam*, an open-source software within the framework of OpenFoam. The relaxation and reaction processes in a CO_2 atmosphere are much more challenging because CO_2 is a polyatomic gas with up to four vibrational modes.

Kumbhakarna et al. [87] studied a detailed model of steady-state combustion of a pseudo-propellant containing cyclotrimethylenetrinitramine and triaminoguanidinium azotetrazolate. The chemical kinetics is represented by a global thermal decomposition mechanism with within the liquid by considering 18 species and 8 chemical reactions.

The design of space vehicles is a challenging process due to the extreme heating environment in the shock layer of the spacecraft at hypersonic speed. Various space research organizations have carried out a large number of missions for space re-entry into nearby planets as well as our own planet and the moon. The United States has successfully landed a number of manned missions on the lunar surface, and a number of unmanned probes on the surface of Mars. However, a number of challenges need to be overcome before crewed missions to nearby planetary bodies, including Mars, become possible. For Mars missions, robotic systems landed so far had a mass below 0.6 metric tons [88]. The future manned mission will require landing of significantly heavier (40-80 metric tons) and larger systems. Such spacecraft are likely to be subjected to extreme radiative heat loads [10,11,89].

Recently, re-entry study into the atmosphere of planet Mars has attracted a lot of attention. The Martian atmosphere is primarily made of CO_2 and N_2, and thus presents a more challenging design problem from the heat transfer point of view. In studying high-temperature, non-thermodynamic equilibrium shock layer heat transfer, the chemical reaction study presents one of the most important and challenging tasks. The chemical reaction study for the CO_2 gas is different from those for gases available in the Earth's atmosphere. The Earth's atmosphere mainly comprises of N_2 and O_2. The complication in studying the chemical reaction in CO_2 is due to it being a polyatomic gas with more than one vibrational modes of energy [90,91]; while in the case of O_2 and N_2, there is only one vibrational mode.

A number of studies [10,11,18,19] have examined the aerothermal environment for a Mars aero-capture vehicle under different entry conditions. In a CO_2 atmosphere, the radiative heat load was found to be significant not only on the front body but also on the after the body of the spacecraft [18][15, 17]. In the Martian atmosphere, the CO_2 gas dissociates while passing through the shock wave, resulting in the gas mixture of CO_2, CO, O_2, C and O. The chemical reactions includes the dissociation of the molecular species CO_2, O_2, and CO and chemical exchange reaction between the gas atoms and molecules. At hypersonic entry, if the temperature is less than 9,000 K, the ionization reactions can be neglected. The presence of a small amount of N_2 can alter the gas flow field in the shock layer. Therefore, a more realistic composition of the Martian atmosphere gas is considered (98.07% CO_2 and 1.93% N_2 by mass), and a chemistry model involving 9 chemical species and 11 reactions is used [10].

The Direct Simulation Monte Carlo (DSMC) method is one of the most powerful methods for simulating the rarefied gas flow [75]. The DSMC method uses the kinetic theory of gases to simulate the flow at the

molecular level. In this method, the motion of particles may be decoupled from particle-particle collision over a time step smaller than the mean free time between collisions. In the computational domain, the moving molecules/particles are tracked, and collisions and collision-generated transitions (rotational, vibrational relaxation as well as chemical reactions) are treated in a probabilistic manner. This method can precisely evaluate non-equilibrium gas behavior. Instead of complex deterministic procedures, the DSMC method employs stochastic tools that lead to higher accuracy and lower computational time.

A hypersonic spacecraft confronts high temperature and low-density conditions while entering the planetary atmosphere, which is far from thermodynamic equilibrium condition; and thus, the representation of the flow conditions with a single temperature is not possible. The different kinetic conditions (rotational, vibrational, and electronic relaxation/excitation of molecules) and various chemical reactions affect temperature around the vehicle. The equipartition of energy theorem is not valid in the non-equilibrium conditions, as some of the internal degrees of freedom of the particles may not be fully excited. Hence, the degree of excitation is evaluated by a separate temperature for each internal mode of energy. Borgnakke and Larsen [77] proposed that the internal energy transfer between various modes of energy is usually implemented in the DSMC method with the phenomenological model. According to this model, the probability of an inelastic collision determines the rate at which energy transfer takes place between translational and other internal modes.

A number of DSMC implementations are available in the research community. Some of these implementations are available free while others are restricted for use. Some of the popular implementations of the DSMC method are: MONACO [92], SMILE [93], DAC [94], PDSC [95] and dsmcFoam. One of the earliest DSMC codes was 'MONACO' developed by Dietrich *et al.,* 1996 [92]. Matsumoto *et al.* 1997 [96], performed the parallelization of the DSMC method, which led to the reduction of significant computational time. The 'SMILE' is a powerful software developed by Ivanov *et al.*, 1998 [93] for simulating rarefied gas flow in two-dimensional, three-dimensional and axis-symmetry internal and external flow. The code is based on Majoran Collision Frequency (MCF) [93].

An extremely important aspect of a DSMC code is the models of interaction of molecules during collisions. SMILE employs both conventional collision models of the DSMC method, which are standard for DSMC codes, and new effective models developed at the Computational Aerodynamics Laboratory of ITAM. A Variable Hard Sphere (VSH) model [46] and a Variable Soft Sphere (VSS) model [97] are used in SMILE to describe elastic collisions. A Larsen-Borgnakke (LB) model [77] is used to model inelastic collisions with the translation-rotation (TR) and translation-vibration (TV) energy transfer. Two different types of LB models are implemented in SMILE: a standard LB model with the continuous representation of internal energies and a modification of the LB model for the discrete (quantum) representation of internal energies [98]. Either constant or temperature-dependent relaxation numbers may be used in the models. For rotational relaxation, the temperature dependence is described by the relation derived in [99]; vibrational relaxation involves a dependence based on experimental data of Millikan and White [100] with a high-temperature correction of Park [101]. The chemical reactions are modeled using the Total-Collection-Energy (TCE) model. The model has two options: standard (for continuous internal energies) [46] and modified (for discrete internal energies) [102]. For discrete internal energies, it is also possible to use a model based on two-temperature kinetics [103]. These models allow modeling bimolecular reactions of dissociation and exchange. The chemical database contains the parameters of all models listed above for

more than 30 mono-, di-, and polyatomic chemical species. The gas-surface interaction modeling procedure uses a Maxwell model or a multiparametric Nocilla model.

In the simplest DSMC programs, the collision partner was chosen from the same cell. In the later implementations by Bird [46], the collision partners were chosen from a sub-cell. In the DS2V [104] program, the information of the immediately preceding collision partners is stored and the selected collision particles are not allowed to undergo collision in the immediately next collision sequence. It has been found that this trick reduces the overall error in the calculation of heat transfer and shear stress.

Moss *et al.* [105] performed a DSMC simulation for hypersonic re-entry of the Apollo capsule in the Earth's atmosphere. In this paper, they compared the DSMC results with the Navier-Stokes code, LAURA, for an altitude range of 65 km to 200 km. The DSMC simulation was found to be reliable from the free-molecular regime to an altitude of 100 km. Tseng *et al.* [85] employed the DSMC method to study hypersonic re-entry flow in the rarefied atmosphere. They simulated three different problems: a sphere, a blunt-body, and the Apollo spacecraft. The Total Collision Energy model was used for dissociation and exchange reactions; while the three-body collision model proposed by Boyd [85] was utilized to calculate the recombination reaction rate. Ozawa *et al.* [106] simulated the hypersonic flow over the stardust vehicle entering into the Earth's atmosphere using the SMILE DSMC code for 80 km altitude and a speed of 12.8 km/s. They compared their DSMC results with the results obtained from the DPLR finite volume code and found that the DSMC code predicted lower energy exchange rates between the translational and the internal energy modes as compared to CFD, which results in lower dissociation rate and degrees of ionization in the DSMC.

A number of numerical studies and experimental work have been published on the hypersonic flow in a convergent-divergent nozzle in the CO_2/N_2 atmosphere [107–109]. These models used the Navier-Stokes solver to study the thermo-chemical non-equilibrium flow.

For the Martian atmosphere, a hypersonic flow continuum solver was constructed and used by Bansal *et al.* [28] to simulate flow over the CEV space vehicle at a speed of 6.5 km/s. The shock layer thickness and the peak temperature were found to be 31 cm and 8,300 K, respectively. The CO_2 was observed to be fully dissociated and CO was reported to be the main gas involved in radiative heat transfer. A method to obtain coupled CFD-DSMC simulation for rarefied hypersonic re-entry of a blunt body was presented by Glass *et al.* [110]. The method was applied to the Martian Sample Return Orbiter as a demonstration. The Langley Aerothermodynamics Upwind Algorithm [111] code was used to perform the forebody CFD analysis. In this study, the Martian atmosphere was modeled as eight species, non-equilibrium gas. All the DSMC simulations were performed with the DAC code. Four different cases with Kn = 0.2, 0.02, 0.002 and 0.0004 were considered. The non-equilibirum thermodynamic conditions were observed in the wake region of the spacecraft.

Chemical dissociation, ionization and exchange reaction occurs in the high-temperature shock layer of a hypersonic spacecraft. The rarefied gas media leads to low reaction rates, and thus, finite rate reactions are required to be considered. A kinetic model for the Martian atmosphere was presented by Drake *et al.* [112] with free stream data from Viking, Pathfinder and other Mars Exploration Rovers. It was observed that CO_2

was almost completely dissociated in the high-temperature shock layer. Further, the presence of a small fraction of water vapor in the gas composition was found to significantly affect the dissociation of CO_2.

A number of models have been proposed for the DSMC method [43,44,79–83] to consider the effects of chemical reactions in the gas mixture. The Total Collision Energy (TCE) is a model which, utilizes the quantity derived from the macroscopic parameters, and is based on the modified Arrhenius rate coefficient. The model uses the equilibrium kinetic theory and converts the conventional Arrhenius rate coefficients (defined in terms of macroscopic gas temperature) to reaction probabilities based on collision energy at the microscopic level. This model was later extended to take into account the coupling between the collision-induced dissociation and vibrational energy [84,85]. The extended TCE model was applied by Boyd *et al.* to calculate the dissociation, exchange and recombination reactions for the Earth's atmosphere entry [83]. The TCE model was used by Dhurandhar *et al.* to study the dissociation of CO_2 under rarefied conditions [86].

Gallis *et al.* [50] proposed a molecular-level chemistry model and calculated the reaction rates for equilibrium as well as non-equilibrium reactions in the upper atmosphere. The model was found to be in good agreement with the Arrhenius rates with non-equilibrium conditions and various other theories and models.

The TCE model was extended by Nizenkov *et al.* [113] to polyatomic reactions for applications of (re-)entry into Martian and Titan's atmosphere. In this paper, dissociation of CH_4 with simple reservoir simulations was tested by the authors, and it was found that the reaction rate agreed well with the theoretical Arrhenius rates. The extended TCE model was then applied to study the reacting flow in Titan's atmosphere for the Huygens probe using the DSMC method. the conventional discrete LB model was improved by Sebastião *et al.* [114] in order to satisfy detailed balance in recombination and exchange reactions in reacting mixtures involving polyatomic molecules. The authors followed an empirical approach to specify the post-reaction vibrational states close to thermochemical equilibrium within the TCE framework.

A molecular-level chemistry model is desired for the particle-based DSMC method, which estimates reaction rates using only the kinetic theory and fundamental molecular properties. Recently, Bird proposed a Quantum-Kinetics (QK) reaction model based on the fundamental properties of colliding particles, i.e., the total collision energy, the quantized vibrational levels, and the dissociation energies. The model connects the energy exchange processes with the chemical reactions, has only a limited dependence on the macroscopic data, and does not require the gas to be in a state of near thermodynamic equilibrium [82]. The QK model is based on the quantum vibration theory as compared to the TCE model. There was a problem with the detailed energy balance among the translational, rotational, and vibrational energy modes in the original QK model. This leads to differences in temperatures after the chemical exchange reactions. Later, Bird implemented the detailed energy balance process to correct the problem [80]. The modified QK model was used by Liechty *et al.*[45] to predict reaction rates in equilibrium and non-equilibrium conditions. In the equilibrium case, the post-collision energy exchange of the system was not implemented, and on the other hand, in the non-equilibrium case, the system undergoes energy exchange, resulting in the change of the temperature of the system. The QK model was further extended to the electronic energy transition [53].

White C. *et al.* [115] implemented the QK technique in the dsmcFoam solver, including the vibrational and electronic energy modes, and chemical reactions. Scanlon *et al.* [43] used the modified dsmcFoam solver for the Earth's atmosphere. The problem with the detailed balance was minimized by modifying the activation energy of the reaction. This procedure utilized the reaction rate coefficients calculated from the Bird's Q-K code [75] and used those coefficients to calculate the reaction rate at equilibrium as well as in non-equilibrium conditions. They simulated hypersonic 2-D flow over a cylinder and found the result in good agreement with the MONACO code, which employs the TCE model.

Recently, Dhurandhar *et al.* have extended the Quantum Chemical Kinetic model to solve chemical reactions in rarefied hypersonic flow conditions encountered during the Martian atmosphere. The model has been developed within the framework of the open-source DSMC code, dsmcFoam. For polyatomic gases, they developed the vibrational relaxation model for more than one vibrational mode. They studied a large number of dissociation and exchange reactions, and the reaction rates for most of the reactions were found to be in good agreement with the previous experimental and theoretical results published in the literature.

In this work, we have modified the dsmcFoam code to include non-equilibrium chemical kinetics and a multi-mode relaxation model to simulate hypersonic flow around a Martian re-entry vehicle. The chemical reactions are modeled using the Quantum Kinetic model [6].

3.3 Vibrational Relaxation in Polyatomic Molecules

Molecular energy is stored in three modes: namely, vibrational, rotational and translational modes. Vibrational relaxation is a process where the vibrational energy of the gas—initially in the non-equilibrium condition—changes such that it reaches the thermal equilibrium condition after a sufficient number of collisions. In the vibrational relaxation model, energy exchange takes place between the translational and the vibrational modes of the particles. Vibrational relaxation is important for chemical reaction modeling in the DSMC method.

CO_2 has 4 vibrational modes and the other molecules like N_2, O_2, CO and NO have one vibrational mode. To consider vibrational relaxation in polyatomic molecules, two particles *P* and *Q* are randomly selected and the sum of pre-collision energy of the pair is calculated. First, the sum of the relative translation energy and the vibrational energy of the particle P is calculated as:

$$\varepsilon_{coll} = \frac{m_r\left|v_P^2 - v_q^2\right|}{2} + \left(i_{P,l} k\theta_{vib,P,l}\right) \qquad 3.1$$

where v represents the velocity of particles, m_r is the reduced mass of the pair of particles, $i_{P,l}$ is the vibrational energy state of a particle at mode l and $\theta_{vib,P,l}$ is the vibrational characteristic temperature of the molecule P and mode l. The maximum possible vibrational quantum number of particle P at mode l ($i_{max,P,l}$) is calculated as

$$i_{max,P,l} = \frac{\varepsilon_{coll}}{k\theta_{vib,P,l}} \quad 3.2$$

where k represents the Boltzmann constant = $1.38 \times 10^{-23} J/K$. Now, the vibrational collision number is calculated as

$$Z_v = \left(\frac{\theta_{diss}}{T_{tr}}\right)^{\omega}\left[Z_{ref}\left(\frac{\theta_{diss}}{T_{Zref}}\right)^{-\omega}\right]\left[\left(\frac{\theta_{diss}}{T_{tr}}\right)^{\frac{1}{3}}-1\right]/\left[\left(\frac{\theta_{diss}}{T_{Zref}}\right)^{\frac{1}{3}}-1\right] \quad 3.3$$

where T_{tr} represents the macroscopic translational temperature of the cell, T_{Zref} is the reference temperature, usually, this value is taken to be the characteristic vibrational temperature θ_{vib} of the species, and Z_{ref} represents the vibrational collision number at the reference temperature and is calculated as:

$$Z_{ref} = \left(\frac{V_1}{T_{zref}^{\omega}}\right)exp\left(V_2 T_{zref}^{-\frac{1}{3}}\right) \quad 3.4$$

where V_1 and V_2 are constants [46]. The inverse of the vibrational collision number is calculated from Eq. 3 and compared with a uniformly distributed random variable in order to decide the vibrational exchange. The post-collision vibrational collision number is randomly selected between 0 and $i_{max,P,l}$, and acceptance-rejection technique is used to set the final vibrational energy state of the particle:

$$Pr = \left(1 - \frac{i'_{P,l} k\theta_{vib,P,l}}{\varepsilon_{coll}}\right)^{1.5-\omega} \quad 3.5$$

If the probability calculated from the Eq. 5 is greater than the uniformly distributed random number between 0 and 1, the post-collision energy state of the molecule is set as $i'_{P,l}$ at mode l and the post-collision vibrational energy is reduced from the pre-collision energy. The procedure is repeated for all the vibrational modes of the particle P and the standard Larsen-Borggnakke [77] approach used to distribute the remaining energy into the rotational and translational modes of the particle. The same procedure is repeated for the particle Q.

In this case, we consider the vibrational relaxation of N_2. We consider a single adiabatic cubical box of side 10μm filled with N_2 gas. Initially, the rotational and translational temperatures of the gas are 20,000 K and the vibration energy of the molecule is assumed zero. The number density of the gas is set at 10^{22} m^{-3}. The vibrational characteristic temperature of N_2 is taken to be 3,371 K, the viscosity-temperature index ω = 0.74, diameter = 4.17×10^{-10} and mass =46.5×10^{-27} kg. The results obtained with our QK model implementation in the OpenFOAM software are compared with those obtained from the DS2V code[75]. It may be observed that both the codes give identical results, with an equilibrium vibration temperature of 14,720 K.

In this case, we consider the vibrational relaxation of N_2. We consider a single adiabatic cubical box of side 10μm filled with N_2 gas. Initially, the rotational and translational temperatures of the gas are 20,000 K and the vibration energy of the molecule is assumed zero. The number density of the gas is set at 10^{22} m^{-3}. The vibrational characteristic temperature of N_2 is taken to be 3,371 K, the viscosity-temperature index ω = 0.74, diameter = 4.17×10^{-10} and mass =46.5×10^{-27} kg. The results obtained with our QK model implementation in the OpenFOAM software are compared with those obtained from the DS2V code[75]. It may be observed that both the codes give identical results, with an equilibrium vibration temperature of 14,720 K.

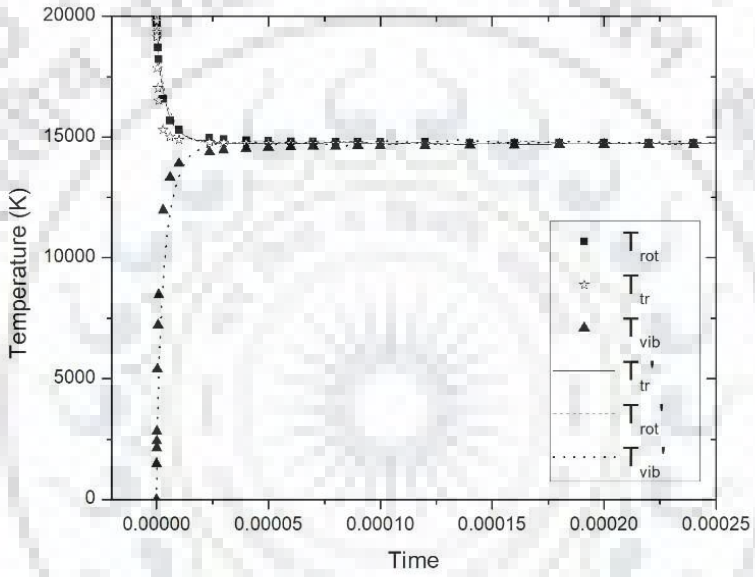

Figure 3.1 Vibrational relaxation of N2 gas

Next, the vibrational relaxation in O_2 is studied. For this study the characteristic vibrational temperature of O_2 taken as 2,256 K [75]. The vibrational relaxation of the O_2 molecule is similar to the N_2 molecule. The result of the vibrational relaxation of the O_2 shown in Figure 3.2. The initial temperature in the rotational and translational mode is taken as 20,000 and in the vibrational mode, the temperature is taken as 0 K. The final equilibrium temperature for the O_2 vibrational relaxation is around 14,603 K.

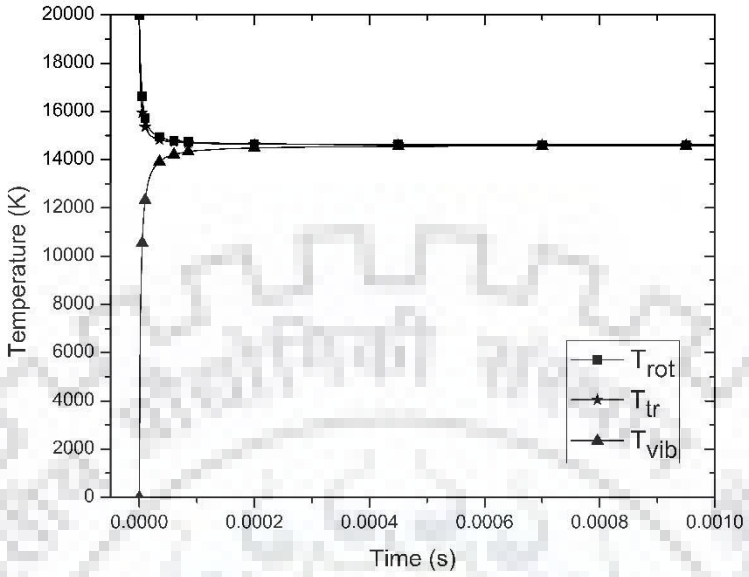

Figure 3.2 Vibrational relaxation of O2 gas

Next, the vibrational relaxation in CO_2 is studied. For this study, the vibration relaxation model was modified to include more than one vibrational mode. The case was studied with the same domain as given in the previous case. Initially, the domain temperature was taken as 10,000 K for the rotational and translational modes, and the energy of all the vibrational modes was assumed zero. The CO_2 molecule has four vibrational modes with one symmetry stretching, one asymmetry stretching and two bending modes[90]. The initial number density of the gas was set as 5.14×10^{21}. The vibrational characteristic temperatures for the four modes of CO_2 are taken as 1997, 3380, 960 and 960 K[90,91]. The viscosity-temperature index for the gas $\omega = 0.93$, diameter = 5.62×10^{-10} m and mass =73.1×10^{-27} kg. The simulation was performed with 100,000 simulated particles.

Figure 3.3 Vibrational relaxation of CO2 gas shows the distribution of temperatures with time. The temperatures shown with a prime represent the results obtained from the DS2V code. The equi-partition of energy is achieved after the sufficient number of collisions, and the temperature of all the modes comes to the equilibrium temperature of 4,370 K. The result obtained from the DS2V code [75] shows the final equilibrium temperature of around 4,240 K.

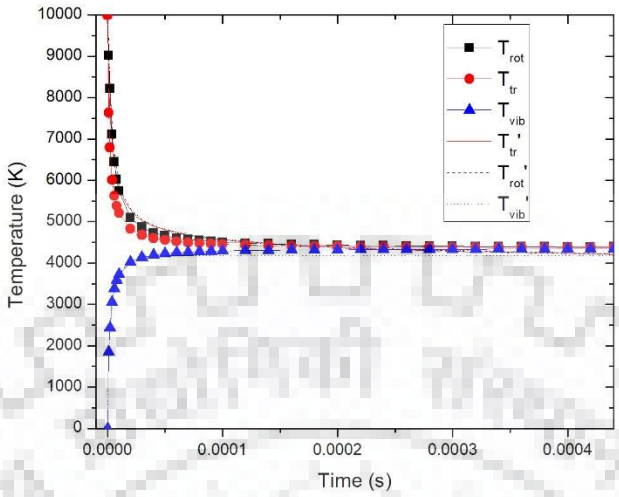

Figure 3.3 Vibrational relaxation of CO2 gas

Next, the vibrational relaxation in CO_2 is studied. For this study, the vibration relaxation model was modified to include more than one vibrational mode. The case was studied with the same domain as given in the previous case. Initially, the domain temperature was taken as 10,000 K for the rotational and translational modes, and the energy of all the vibration modes was assumed zero. The CO_2 molecule has four vibrational modes with one symmetry stretching, one asymmetry stretching and two bending modes[90]. The initial number density of the gas was set as 5.14×10^{21}. The vibrational characteristic temperatures for the four modes of CO_2 are taken as 1997, 3380, 960 and 960 K[90,91]. The viscosity-temperature index for the gas $\omega = 0.93$, diameter = 5.62×10^{-10} m and mass =73.1×10^{-27} kg. The simulation was performed with 100,000 simulated particles.

As shown in Figure 3.4, the CO_2 molecule has four vibrational modes: one symmetric C-O stretching, one asymmetric C-O stretching, and two bending modes. The vibrational temperature in symmetric C-O stretching mode at wavenumber 1333 cm^{-1} is 1997 K, in asymmetric C-O stretching mode at wavenumber 2349 cm^{-1} is 3380 K and in bending mode at wavenumber 667 cm^{-1} is 960 K. [90,91].

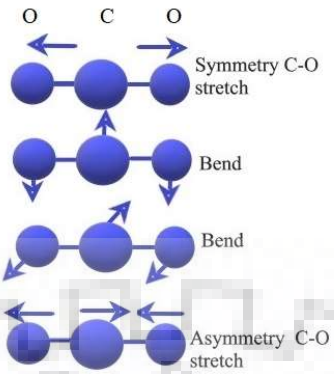

Figure 3.4 Vibrational Modes of CO2

3.4 Total Collision Energy Model

3.5 Quantum-Kinetic (QK) Chemical Reaction Model

In this work, the QK model is applied to the Martian atmosphere (CO_2 and N_2) with an eight species model. The gaseous species considered in the high-temperature shock layer of a Martian reentry vehicle are CO_2, N_2, O_2, NO, CO, O, N, and C. The reaction model comprises of a number of dissociation and exchange reactions.

3.5.1 Dissociation reaction

A dissociation reaction occurs when two species (at least one of them is molecule) collide with each other. The dissociation reaction does not require calculating the reaction probability; rather it depends on the sum of the energy of colliding particles. Consider dissociation reaction AB + C → A + B + C, wherein particle AB is a molecule and particle C is an atom. The collision energy of the pair of colliding particles is calculated with Eq. 3.1. For the molecule AB, the maximum possible post-collision vibrational quantum number, i_{max}, is calculated from Eq. 3.2. The particle AB will dissociate if the ratio of the dissociation and the vibrational characteristic temperature satisfy the following relation

$$i_{max} > \frac{\theta_{diss}^{AB}}{\theta_{vib}^{AB}} \qquad 3.6$$

The dissociation reaction rate is given as

$$k_f(T) = gR_{coll}^{AB,C}\gamma(i_{max})^{AB,C} \qquad 3.7$$

where g is the degeneracy of the reaction in the case of a polyatomic molecule with the same characteristic vibration temperatures for different modes, R_{coll} is the collision rate parameter, and γ is the fraction of collisions with energy satisfying Eq .3.6. The collision rate parameter is given as:

$$R_{coll}^{AB,C} = \left(\frac{2\pi^{\frac{1}{2}}}{\sigma}\right)\left(r_{ref}^{AB} + r_{ref}^{C}\right)^2 \left(\frac{T}{T_{ref}}\right)^{1-\omega^{AB,C}} \times \left(\frac{2kT_{ref}}{m_r^{AB,C}}\right)^{1/2} \qquad 3.8$$

where r_{ref} is the reference radius of the gas species at temperature T_{ref}. The parameter γ is given as

$$\gamma(i_{max})^{AB,C} = \sum_{i=0}^{i_{max}-1} \left\{ Q\left[\left(\frac{5}{2} - \omega^{AB,C}\right), \left(\frac{(i_{max} - i)\theta_{vib}^{AB}}{T}\right)\right] \exp\left(-\frac{i\theta_{vib}^{AB}}{T}\right)\right\} / Z_v(T)^{AB} \quad 3.9$$

where $Q(a,b) = \lceil(a,b)/\lceil(a)$ is the incomplete Gamma function and Z_{vT} is the vibrational partition function of mode *v*.

$$Z_{vT} = \frac{1}{1 - \exp\left(\frac{\theta_v}{T}\right)} \quad 3.10$$

If the collision pair satisfies Eq. 3.6 and the molecule *AB* undergoes dissociation, the dissociation energy of the molecule *AB* is reduced from the total collision energy (ε_{coll}). The energy stored in the other vibrational modes of the molecule *AB* is added to the collision energy. If the product of dissociation of *AB* is a molecule, then the vibrational and rotational energy of the product molecule is set and the remaining energy is re-distributed into the translational modes of dissociated *AB* and *C* particles. The energy stored in the rotational mode of the particle *AB* is distributed in the relative translational energy of the dissociated particles *A* and *B*. This is graphically explained in Figure 3.5.

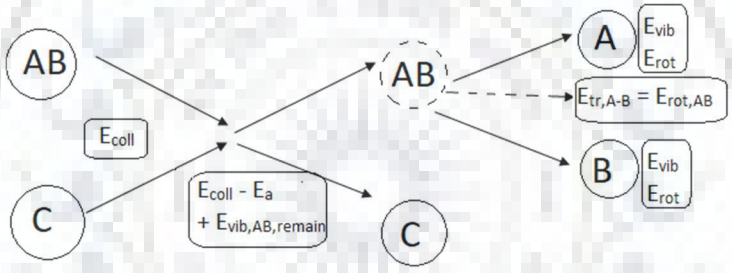

Figure 3.5 Dissociation and energy redistribution of CO2

The calculation of the probability of dissociation of any selected particle is explained in detail by Dhurandhar *et al.*. If a polyatomic molecule does not undergo dissociation in a particular vibrational mode, then the same procedure is repeated for other vibrational modes.

3.5.2 Endothermic and Exothermic Exchange Reaction

The exchange reaction between molecule *ABC* and atom D is written as:

$$ABC + D \rightarrow AB + CD$$

First, the total collision energy is calculated for the stretching mode (valence mode) of the molecule using Eq. 3.1 [116]. To calculate the probability of the exchange reaction for the collision between species *ABC* and D, we first check if the sum of relative translational energy of the colliding particles and vibrational energy of the colliding molecule is greater than the activation energy of the reaction.

$$E_c > E_a \quad 3.11$$

The activation energy for the endothermic and exothermic exchange reactions is adjusted to satisfy the detailed balance according to Scanlon *et al.* as [43], this is done to ensure both the reaction rates are consistent with the value predicted with the statistical mechanics. The activation energy for the forward endothermic and backward exothermic exchange reaction is adjusted as[5]:

$$E_f = |E_h|\left[1 + a\left(\frac{T}{273}\right)^b\right] \quad 3.12$$

$$E_b = |E_h'|\left[a\left(\frac{T}{273}\right)^b\right] \quad 3.13$$

where a and b are adjustment parameters and T is the macroscopic translational temperature. Before applying the QK model to the Martian atmosphere, we have validated the model with the cases studied by Bird[29]. The probability of the forward exchange reaction is given as

$$Pr = \frac{\left(1 - {E_a}/{E_c}\right)^{3/2-\omega}}{\sum_{i=0}^{i_{max}}\left(1 - \frac{ik\theta_{vib}}{E_c}\right)^{3/2-\omega}} \quad 3.14$$

The probability for backward exchange reaction is given as:

$$\Pr = a\left({T}/{273}\right)^b \exp\left(\frac{-E_b}{kT}\right) \quad 3.15$$

The reaction rate coefficient for the forward and the backward exchange reactions are given as

$$k_f(T) = R_{coll}\exp\left(-\frac{E_a}{kT}\right)/Z_v(T) \quad 3.16$$

$$k_r(T) = R_{coll}\exp\left(-\frac{E_b}{kT}\right)/Z_v(T) \quad 3.17$$

If the selected pair of particles is accepted for the exchange reaction, the activation energy for the given reaction is reduced from the total collision energy and the energy stored in other vibrational and rotational modes is added to this remaining energy. This total energy is now distributed into vibrational and rotational modes of the new molecules *AB* and *CD*. The vibrational energy state for molecule *AB* is set as

$$i_{vib,AB} = -\ln(Rn) \times T_{tr}/\theta_{vib,AB} \quad 3.18$$

Thus set, the vibrational energy of molecule *AB* is reduced from the total collision energy and if the remaining energy comes out less than zero, then the vibrational energy state of the particle *AB* is reduced by 1. The rotational energy of the molecule *AB* is set as

$$E_{rot,AB} = -\ln(Rn) \times K \times T_{tr,AB} \qquad 3.19$$

The set rotational energy is reduced from the total collision energy and if the remaining energy comes out less than zero, the rotational energy of *AB* is reduced by a factor of half [75]. The same procedure is repeated for the molecule *CD*.

Once the vibrational and rotational energies of both the molecules are set, the remaining energy is distributed in the relative translational energy of the product molecules *AB* and *CD*. This is explained graphically in Figure 3.6.

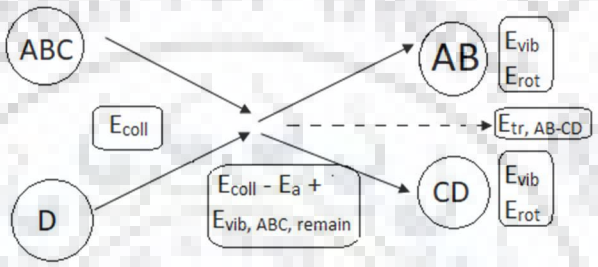

Figure 3.6 Exchange reaction and energy redistribution of CO2

The list of chemical reactions implemented in the QK model for the Martian atmosphere along with their Arrhenius parameters are given in Table 3.1

The chemical reactions considered in this work are selected based on the concentration of free stream species available in the Martian atmosphere [10]. Table 3.2 Parameters for the forward and backward exchange reaction shows the *a* and *b* value for the exchange reaction, these parameters are used in Eq. 3.12 and 3.13 for calculating the probability of exchange reaction.

Table 3.1 Chemical reaction list and their Arrhenius coefficient for reaction rate calculation

Reaction	Heat of formation E_h ($\times 10^{19}$), J	A	n	Activation energy ($\times 10^{19}$), J	Reaction Type	Source
$CO_2 + CO_2 \rightarrow CO + O + CO_2$	8.736	1.14×10^{-8}	-1.50	8.736	Dissociation	Ref [10]
$CO + CO \rightarrow C + O + CO$	17.810	3.82×10^{-10}	-1.00	17.810	Dissociation	Ref [10]
$CO + O \rightarrow C + O + O$	17.810	5.65×10^{-10}	-1.00	17.810	Dissociation	Ref [10]
$NO + NO \rightarrow N + O + NO$	10.424	1.00×10^{-10}	-1.00	10.424	Dissociation	Ref [43]
$NO + O \rightarrow N + O + O$	10.424	4.00×10^{-10}	-1.10	10.424	Dissociation	Ref [43]
$N_2 + N_2 \rightarrow N + N + N_2$	15.670	4.10×10^{-12}	-0.62	15.670	Dissociation	Ref [43]

$N_2 + N \rightarrow N + N + N$	15.670	1.00×10^{-11}	-0.68	15.670	Dissociation	Ref [43]
$O_2 + O_2 \rightarrow O + O + O_2$	8.197	5.33×10^{-11}	-1.00	8.197	Dissociation	Ref [43]
$O_2 + O \rightarrow O + O + O$	8.197	1.50×10^{-10}	-1.05	8.197	Dissociation	Ref [43]
$CO_2 + O \rightarrow CO + O_2$	3.838	3.48×10^{-17}	0.00	3.838	Endothermic	Ref [10]
$CO + O \rightarrow C + O_2$	9.554	6.48×10^{-17}	-0.18	9.5541	Endothermic	Ref [10]
$C + O_2 \rightarrow CO + O$	-9.554	3.32×10^{-17}	0.00	0.210	Exothermic	Ref [117]
$N_2 + O \rightarrow NO + N$	5.175	0.80×10^{-16}	0.00	5.175	Endothermic	Ref [43]
$NO + N \rightarrow N_2 + O$	-5.175	5.00×10^{-16}	-0.35	0.200	Exothermic	Ref [43]
$NO + O \rightarrow N + O_2$	2.719	2.30×10^{-19}	0.50	2.719	Endothermic	Ref [43]
$N + O_2 \rightarrow NO + O$	-2.719	4.00×10^{-15}	-0.39	0.200	Exothermic	Ref [43]

The adjustment parameters for the backward exchange reaction are given in Table 3.2:

Table 3.2 Parameters for the forward and backward exchange reaction

Reaction	a	b
C +O2 → CO + O	0.7665	0.7
NO + N → N2 +O	0.033	0.8
N + O2 → NO + O	0.100	0.1
$CO + O \rightarrow O_2 + C$	0.025	0.77
$N_2 + O \rightarrow NO + N$	0.150	0.15
$NO + O \rightarrow O_2 + N$	0.085	0.65

3.6 Chemical Reaction Rates:

In this case, the Bird's Quantum Kinetic model is applied to study chemical reactions in the shock layer of a hypersonic spacecraft under rarefied conditions. We again consider a single homogenous computational cubical cell of side 10 μm with 50,000 simulation particles. We consider only one reaction at a time for a given initial temperature. In the equilibrium case studied here, once a particle/molecule is accepted to undergo a reaction, it is marked with a flag. This is done so that the same particle is not selected again for the collision. Furthermore, the post-collision energy exchange is not implemented, as it will change the temperature of the system.

3.6.1 Dissociation reaction:

The dissociation reactions considered in the Martian atmosphere are those of dissociation of CO_2, CO, N_2, NO, and O_2. The O_2 has the lowest dissociation temperature while the CO has the highest dissociation temperature. The number density of the gas for all the cases is taken as 10^{22} m^{-3} and the temperature is varied from 4000 K to 20,000 K. The temperature of all the modes is kept same and constant, implying thermal equilibrium under an isothermal process.

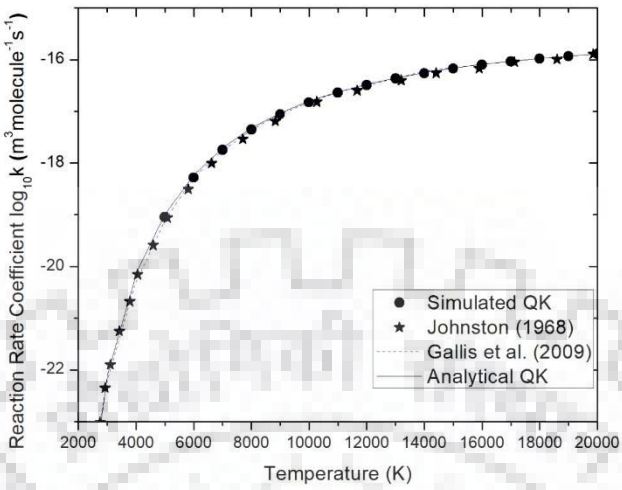

Figure 3.7 Dissociation rate coefficient for O2 + O2 → O + O + O2

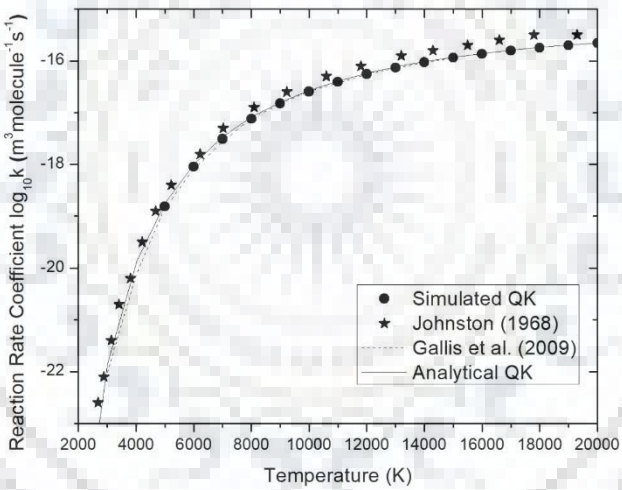

Figure 3.8 Equilibrium dissociation rate coefficient for O2 + O → O + O + O reaction

Figure 3.7 compares the equilibrium dissociation rate of O_2 from the present QK model with the earlier models. In this case, the colliding particle is also O_2. A good agreement is observed in the results for the entire temperature range. The reaction rate increases sharply for up to 10,000 K and then becomes almost stable. Figure 3.8 shows the dissociation rate of O_2 when the colliding particle is atomic oxygen. In this case also, good agreement is observed with the earlier models. The rates from Johnston[118] are based on the least square fit to earlier analytical as well as experimental shock tube data. On the other hand, the results of Gallis[50] are based on the molecular chemistry model.

Similarly, Figure 3.9 shows for the collision between nitrogen molecular and atomic nitrogen, the reaction rates calculated in the present study are in good agreement with the reaction rates calculated by Dunn *et*

al.[119] and Boyd [44]. However, there is slight disagreement with the rates given by Park *et al.*[120] Again, the difference in the rates is attributed to the temperature exponent used by Park.

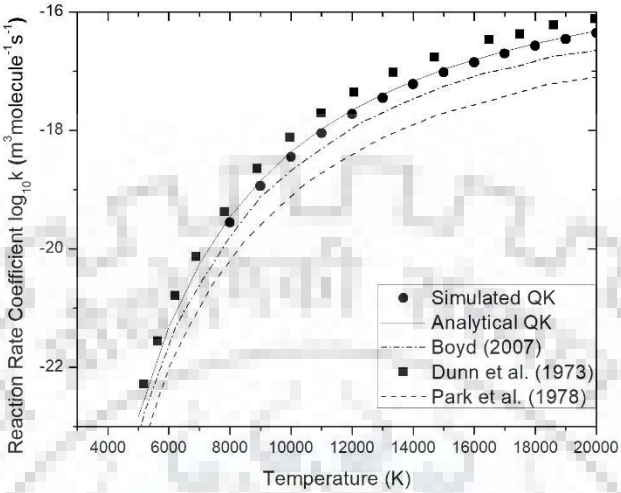

Figure 3.9 Dissociation rate coefficient for N2 + N → N + N + N

Similarly, Figure 3.10 shows the dissociation rates of N_2 [10,][75][,31]. In this case, the reaction rates obtained by Boyd[44] with the Total Collision Energy model are also given for comparison. Hanson *et al.*[121] experimentally studied the dissociation of undiluted nitrogen gas on the end wall of the shock tube. Dunn *et al.* [119] performed a theoretical study and compared the results with the in-flight data. There is some disagreement between the present rates and the rates given by Boyd at high temperatures. This is due to the temperature exponent used in the TCE model of Boyd. Bird also reported similar observations for the dissociation of notrogen[82].

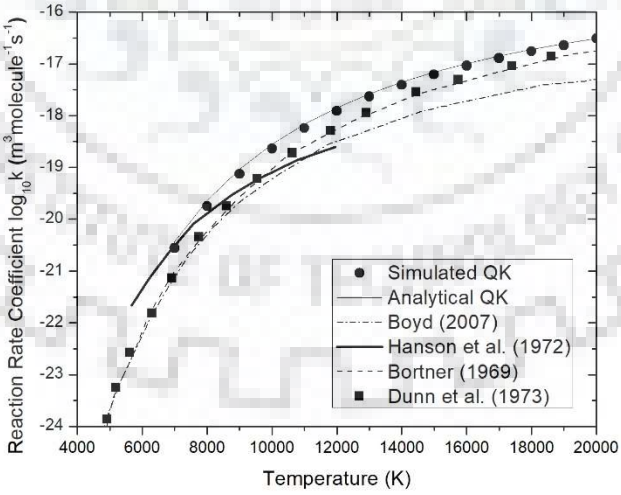

Figure 3.10 Equilibrium dissociation rate coefficient for N2 +N2 → N + N + N2 reaction

Figure 3.11 and Figure 3.12 show the dissociation of NO. There are very few studies available for the dissociation of NO[75,122–124], and that too was limited to temperature below 7500 K.

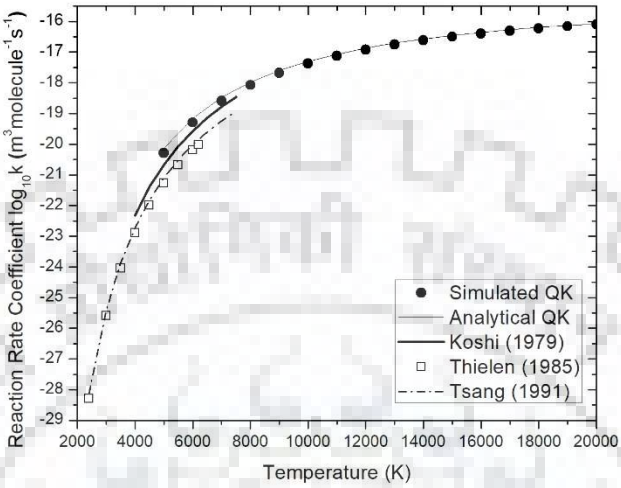

Figure 3.11 Equilibrium dissociation rate coefficient for NO + NO → N + O + NO reaction

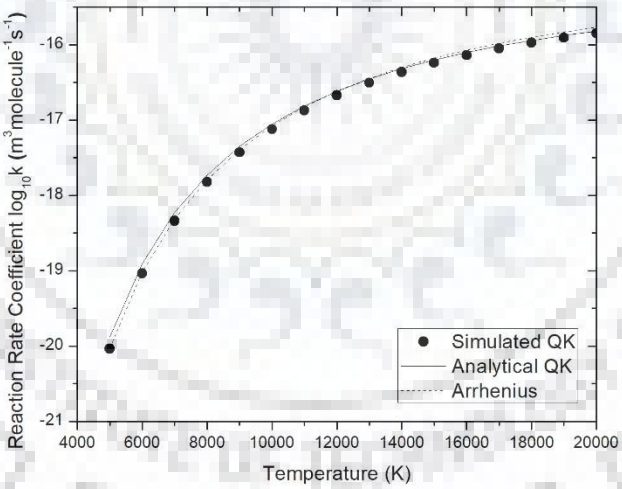

Figure 3.12 Equilibrium dissociation rate coefficient for NO + O → N + O + O reaction

Figure 3.13 and Figure 3.14 show the dissociation of CO[75]. Park *et al.*[10] has reviewed the reaction rate for the decomposition of CO in the Martian atmosphere. Overall, good agreement was observed between the present study, the QK analytical model, and the Park model for temperatures up to 12000 K. The rate coefficients reported by Park et al. are slightly higher at temperatures above 12000 K.

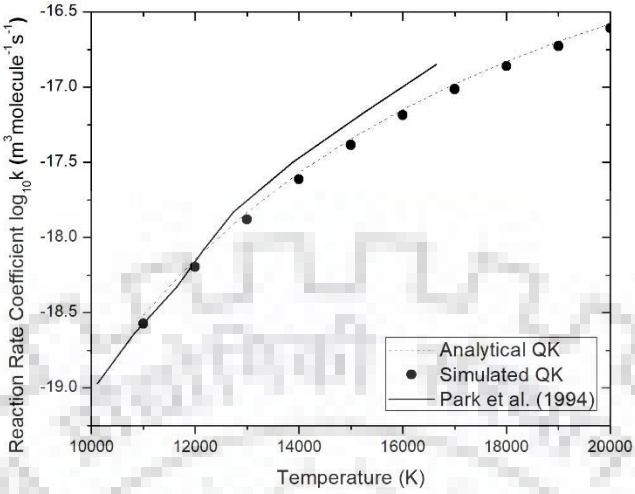

Figure 3.13. Dissociation rate coefficient for CO + O → C + O + O

Hanson *et al.* experimentally studied the dissociation of undiluted carbon monoxide for the temperature range 5,600 K to 12,000 K[125]. Chackerian studied the dissociation of CO heated by a shock wave[126]. The present study is in good agreement with the rate given by Hanson, Park *et al.* [10] and Chackerian.

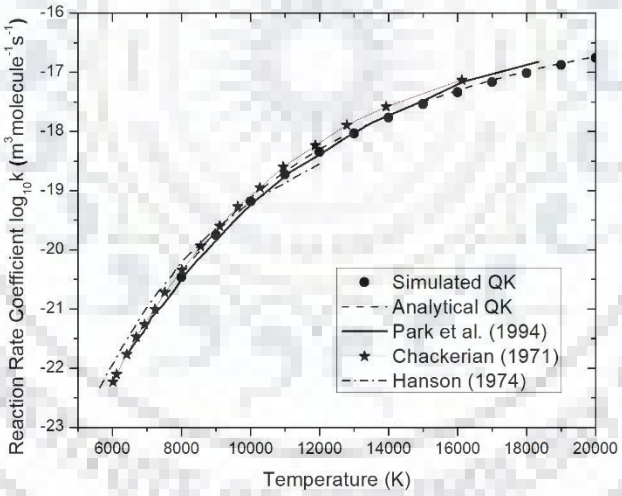

Figure 3.14 Dissociation rate coefficient for CO + CO → C + O + CO

Since CO_2 is the main constituent in the Martian atmosphere, its dissociation is the most important reaction in this study. The CO_2 gas has four vibrational degrees of freedom and the dissociation temperature of CO_2 is lower than CO, N_2, and O_2. Thus, CO_2 dissociates at much lower temperatures than all other gases considered in this study. Figure 7 compares the dissociation rate of CO_2 [10,127]. Our results show good agreement with the results of Park *et al.* The reaction rates calculated by Park are limited to 13,000 K. Burmeister *et al.* [127] calculated the dissociation rate of CO_2 for 2400 K to 4400 K temperature range behind a reflected shock wave. Davies *et al.* [128] measured the dissociation of diluted CO_2 in the mixture of CO_2 and Ar behind a reflected shock in the temperature range between 6,000 K to 11,000 K. Again, the

discrepancy is observed between the rates calculated using the analytical method and those obtained from the experimental data.

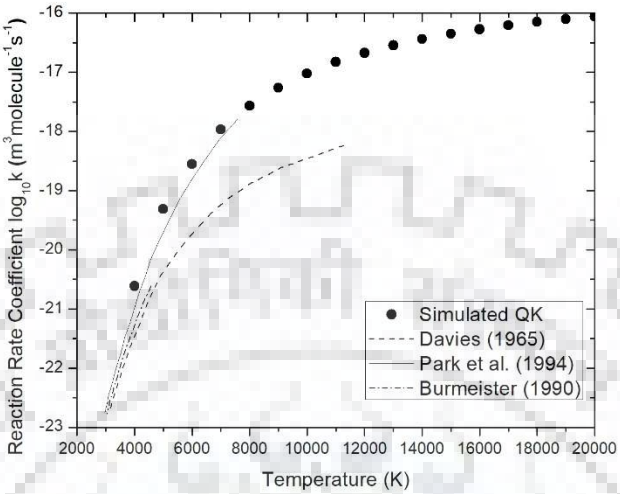

Figure 3.15 Dissociation rate coefficient for CO2 + CO2 → CO + O + CO2

3.6.2 Endothermic to exothermic reaction rate ratio:

In this part, the ratio of endothermic to exothermic reaction rates was calculated and compared with the statistical mechanism. The adjusted analytical QK is calculated for all the exchange reaction. The adjustment parameter *a* and *b* value given in Table 3.2 used for the calculation of the ratio.

Figure 3.16 shows the reaction rates for the CO exchange reaction are in good agreement with the statistical mechanism. Due to the high-adjusted activation energy for the CO reaction, the lower temperature for the CO reaction 12,000 K.

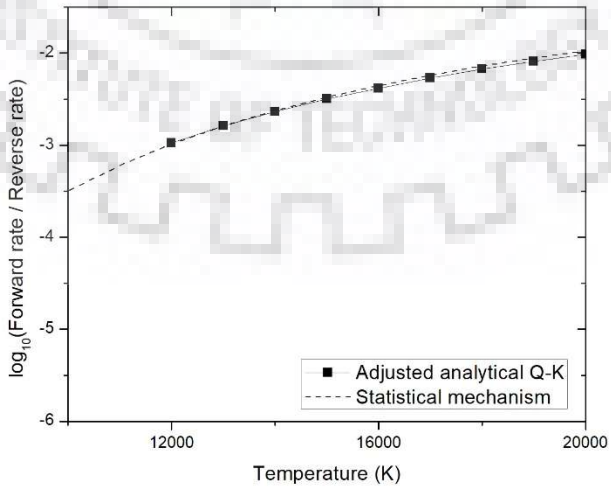

Figure 3.16 Endothermic to exothermic reaction rate for CO + O → C + O2

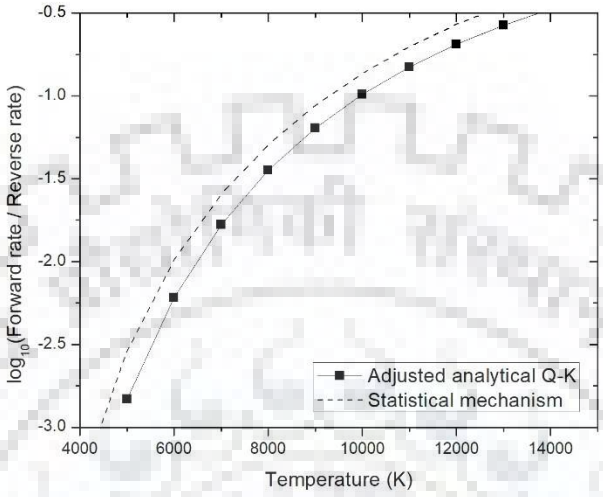

Figure 3.17Endothermic to exothermic reaction rate for N2 + O → NO + N

Figure 3.17 and Figure 3.16Figure 3.18 shows the ratio of the reaction rate for N_2 and NO exchange reaction. The ratio was compared with the statistical mechanism, and reasonable agreement found in both the cases.

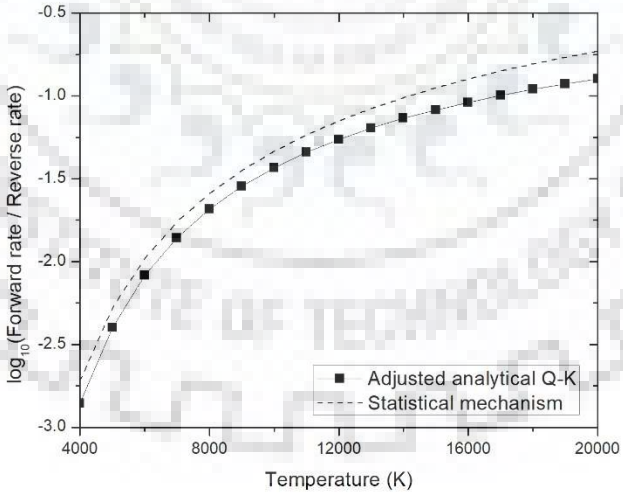

Figure 3.18 Endothermic to exothermic exchange reaction rate NO + O → N + O2

3.6.3 Endothermic exchange reaction:

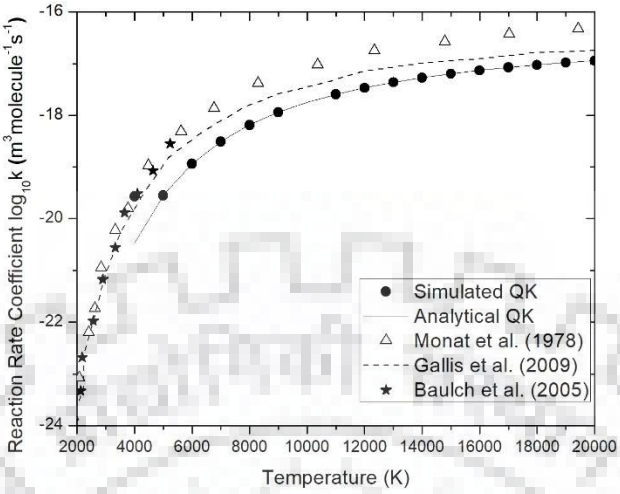

Figure 3.19 Endothermic exchange rate coefficient for N2 + O → NO + N

Figure 3.19Figure 3.22 presents the reaction rates for four endothermic exchange reactions. These reactions are studied under the same conditions as assumed for the cases of dissociation reactions. The mole fraction of the species in the initial mixture is taken to be the same. Figure 3.19 shows the reaction rate for the exchange reaction of N_2[75]. The comparison of reaction rate with the other models and previous data shows that the present model is able to calculate the reaction rates very accurately for the entire temperature range. The probability of the above reaction is very low below a temperature of 4000 K, and therefore, we have not calculated the reaction rates for temperatures below 4000 K.

Figure 3.20 and Figure 3.21 presents the reaction rates for three endothermic exchange reactions. These reactions are studied under the same conditions as assumed for the cases of dissociation reactions. The mole fraction of the species in the initial mixture are taken to be the same

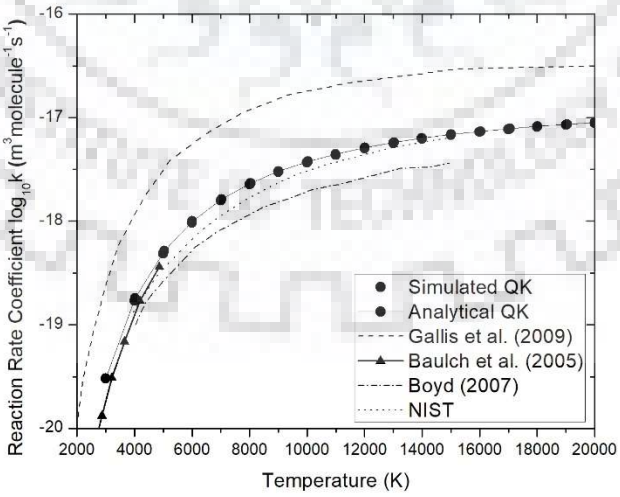

Figure 3.20 Endothermic exchange rate coefficient for NO + O → N + O2

The rates for the exchange reaction of NO are shown in Figure 3.20. At high temperatures, the data from all the sources agree well; however, at lower temperatures, the rates are given by Chernye *et al*[129] and Baulch *et al.* [130] are about an order of magnitude lower than those given by Gallis *et al* [50] as well as than those obtained in this study. Gallis *et al.* did not consider the adjustment of activation energy, shows a higher rate of reaction across all the temperatures.

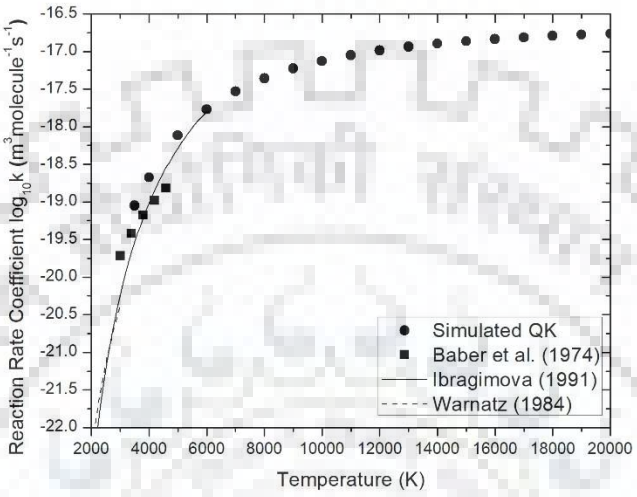

Figure 3.21 Endothermic exchange rate coefficient for CO2 + O → CO + O +O

Figure 3.21 shows the reaction rate for the endothermic reaction between CO_2 and O, and good agreement was observed with the values recommended by Ibragimova [131]. Further, for the same reaction, the reaction rate have been determined experimentally by Baber *et al.* [132] behind a reflected shock wave and by Warnatz [133] for the combustion applications.

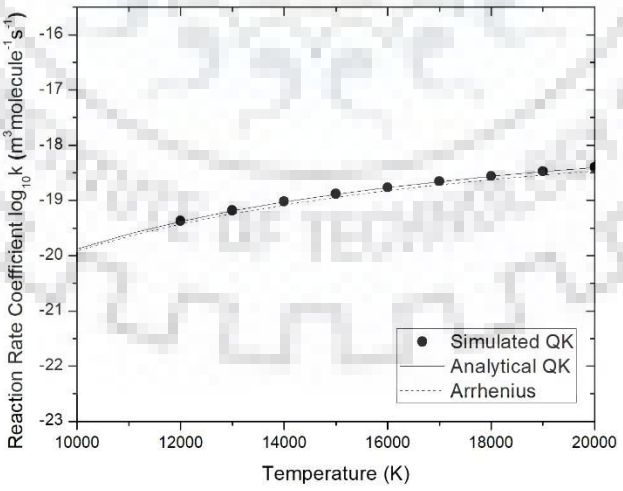

Figure 3.22 Endothermic exchange rate coefficient for CO + O → C + O2

Figure 3.22 shows the rates for the endothermic exchange reaction between CO and O. This reaction is an important reaction as the concentration of CO molecule is very high due to the dissociation of CO_2. The rates obtained in this work are compared with the analytical QK model and the Arrhenius reaction rates. The agreement between the models was found to be very good.

3.6.4 Exothermic exchange reaction:

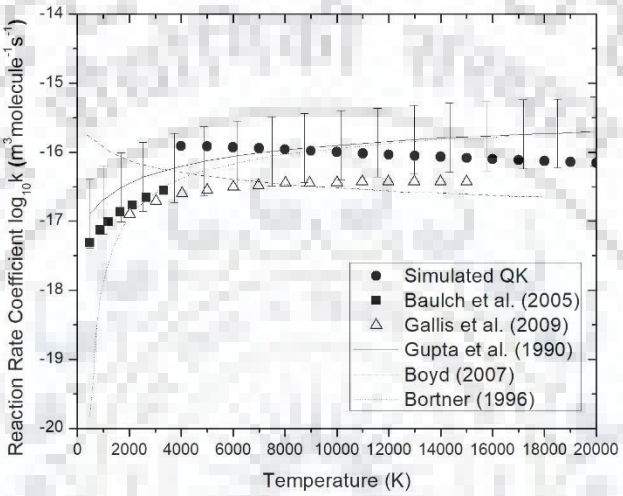

Figure 3.23 Exothermic exchange reaction rate coefficient for O2 + N → NO + O

Figure 3.23 shows the reaction rates for the exothermic reaction between O_2 and N[44,50,134]. In this case, the standard deviation of the reaction rate was found to be large as compared to other reactions studied in this paper. The experimental rates for this reaction have been reported by Bortner [135] and Baulch *et al.* [130].

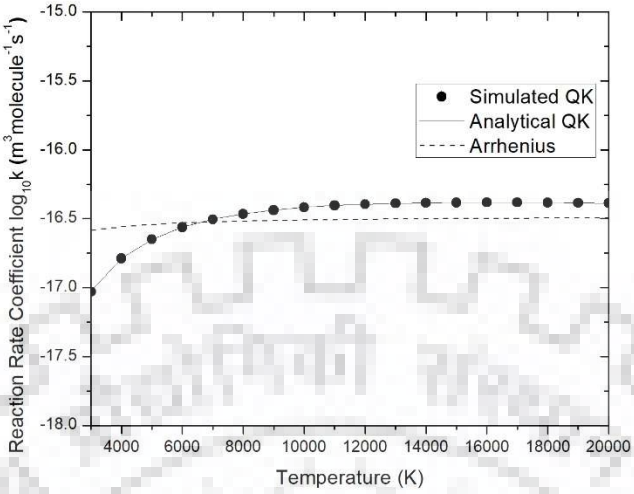

Figure 3.24 Exothermic exchange rate coefficient for C + O2 → CO + O

Figure 3.24 shows the reaction rates for the oxidation of carbon calculated by the QK model and compared with the rate calculated by the analytical QK method and Arrhenius reaction rate. The result is in good agreement with the results obtained from the analytical QK model and the Arrhenius reaction rate.

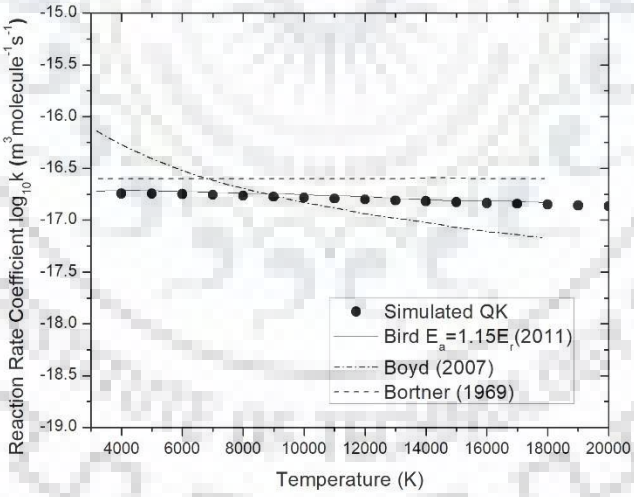

Figure 3.25 Exothermic exchange rate coefficient for NO + N → N2 + O

The reaction rates for the exothermic reaction between NO and N are shown in Figure 3.25. The results agree very well with those calculated by Bird [82]. Bird adjusted the activation energy of the reaction by a factor of 15 percent.

3.6.5 Non-equilibrium reaction rate:

All the reaction rates discussed so far involved the gases in thermal equilibrium. The modes of internal energy of the gases were in equilibrium and all the temperatures were the same. In the non-equilibrium case, the post-collision energy distribution among the molecules may lead to differences in energy distribution in various internal modes. Thus, in this case the temperatures of various modes may not be the same. Non-equilibrium reaction rates were calculated for the exothermic reaction between NO and N. The reaction rates shown in Figure 3.26. The temperature values in the figure represent the translational mode of energy. Overall, good agreement is observed with the reaction rates calculated by Gupta *et al.* [134] and Baulch *et al.*[130]. The rates reported by Monat *et al.* [136] are from a shock tube experiment while those of Gallis *et al.* [50] are based on the kinetic theory.

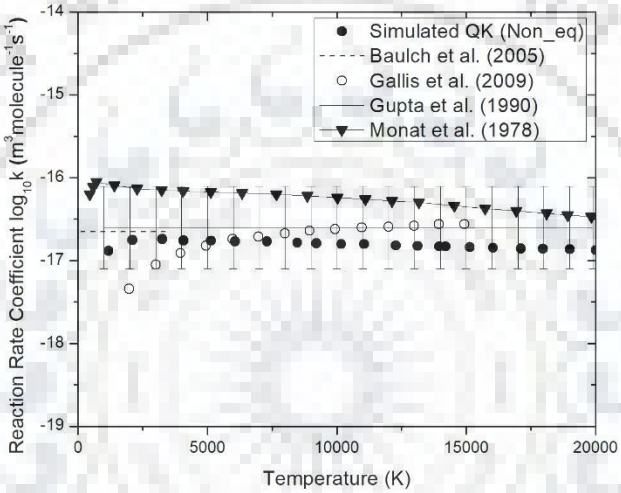

Figure 3.26 Non-equilibrium exothermic exchange rate coefficient for NO + N → N2 + O

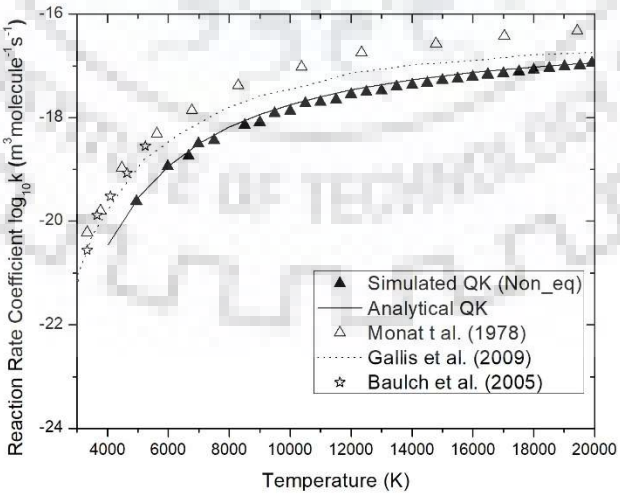

Figure 3.27 Non-equilibrium endothermic exchange rate coefficient for N2 + O → NO + N

Figure 3.27 shows the reaction rate for the exchange reaction of N_2[75]. The comparison of reaction rate with the other models and previous data shows that the present model is able to calculate the reaction rates very accurately for the entire temperature range. The probability of the above reaction is very low below a temperature of 4000 K, and therefore, we have not calculated the reaction rates for temperatures below 4000 K.

3.7 Non-equilibrium temperature Sampling

The sampling of rotational temperature from the energy of simulated molecules is already implemented in dsmFoam; however, the vibrational temperature was not implemented. The vibrational temperature sampling is very important in this study. The overall temperature of the sampling cell depends on the vibrational, rotational and translational temperature of the species available in the sampling cell. The overall vibrational temperature of a computational cell is based on the vibrational energy of each molecular species in the gas mixture in all of its various vibrational modes. The vibrational temperature of mode *l* of a species *P* given as [75]

$$T_{vib,P,l} = \frac{\theta_{vib,P,l}}{\ln\left(1 + \frac{\sum N_P''}{\sum i_{vib,P}''^{\,l}}\right)} \tag{3.20}$$

where $\theta_{vib,P,l}$ represents the characteristic vibrational temperature of species *P* in vibrational mode *l*, $\sum N_P''$ represents the total number of simulated molecules of species *P* and $\sum i_{vib,P}''^{\,l}$ represents the sum of vibrational levels of simulated molecules *P* in vibrational mode *l*. Similarly, the vibrational degrees of freedom of species *P* in mode *l* is given as

$$\tau_{vib,P,l} = 2\left(\sum i_{vib,P}''^{\,l}/N_P''\right)\ln\left(1 + \frac{\sum N_P''}{\sum i_{vib,P}''^{\,l}}\right) \tag{3.21}$$

The total number of vibrational degrees of freedom of species *P* is calculated by summing over all the vibrational modes as:

$$\tau_{vib,P} = \sum_{l=1}^{l=m} \tau_{vib,P,l} \tag{3.22}$$

The vibrational temperature of species *P* is calculated as:

$$T_{vib,P} = \frac{\sum_{l=1}^{l=m}(\tau_{vib,P,l}T_{vib,P,l})}{\tau_{vib,P}} \tag{3.23}$$

The effective vibrational degrees of freedom is calculated by averaging over all the molecular species:

$$\tau_{vib} = \sum_{p=1}^{q}\left(\tau_{vib,P}\sum N_P''\right)/\sum_{p=1}^{q} N_P'' \tag{3.24}$$

and the overall vibrational temperature is calculated as:

$$T_{vib} = \sum_{p=1}^{q} \left(T_{vib,P} \sum N_P'' \right) / \sum_{p=1}^{q} N_P'' \qquad 3.25$$

Chapter 4
APPLICATION OF DSMC MODEL IN EARTH'S RE-ENTRY

The Earth atmosphere mostly consists of N_2 and O_2 gases. For hypersonic entry of the spacecraft into the Earth atmosphere, spacecraft such as Stardust [24,25,27,137–139], Crew Exploration Vehicle[140] or MUSES [141] experience hypersonic non-equilibrium flow condition. The gases in the shock region of the spacecraft go through the chemical dissociation, exchange, and ionization process. This hypersonic non-equilibrium process generates a large amount of heat on the surface of the spacecraft, sometimes this large amount of heat can lead to radar communication breakout to the vehicle[142].

We first present the validation results of our model for flow over a cylinder in Earth's atmosphere. The freestream conditions for the test case are given in Table 4.1. To be consistent with the study of Scanlon *et al.,*[43], the value of the rotational and the vibrational collision numbers are set to 5 and 50, respectively. The geometry and the mesh of the test case are taken the same as that of the case considered by Scanlon *et al.* [43]. The cylinder wall is assumed to be fully diffused.

Table 4.1 Free stream conditions for flow over a cylinder [43]

Parameter	Value
Diameter of cylinder	2 m
Free stream velocity	6813 m/s
Free stream temperature	187 K
Temperature of cylinder wall	1000 K
N_2 Number density	1.13×10^{20} m^{-3}
O_2 Number density	3.031×10^{19} m^{-3}

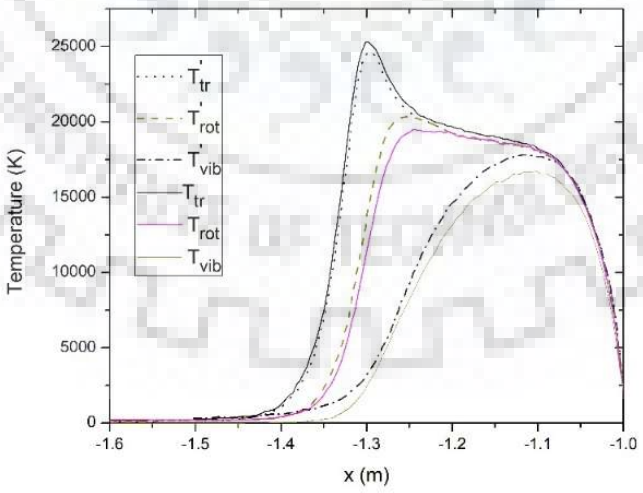

Figure 4.1 Temperature profile along the stagnation line for a non-reacting case

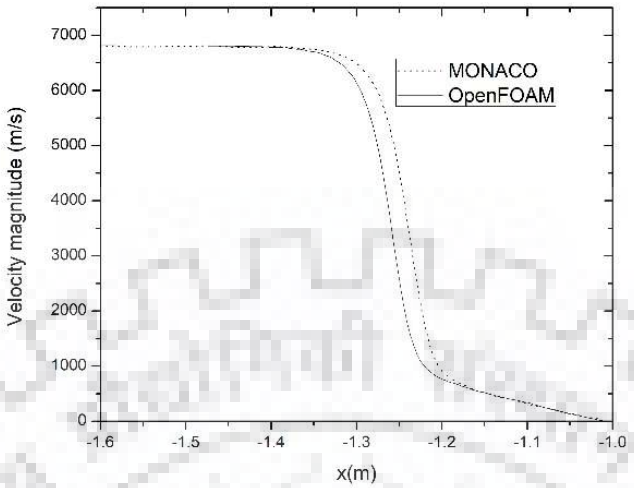

Figure 4.2 Velocity Plot

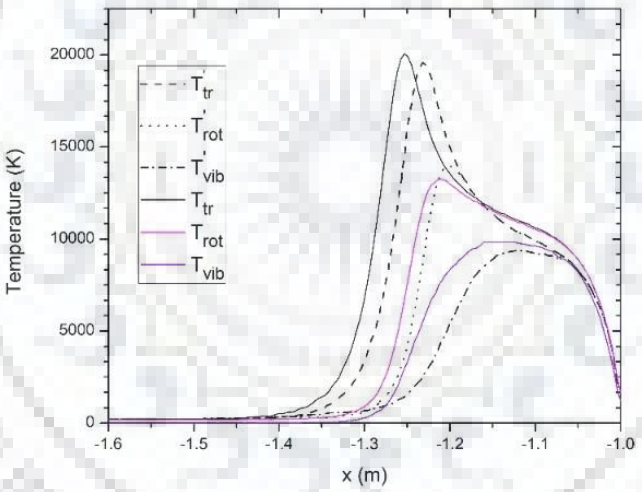

Figure 4.3 Temperature Plot for Reacting flow

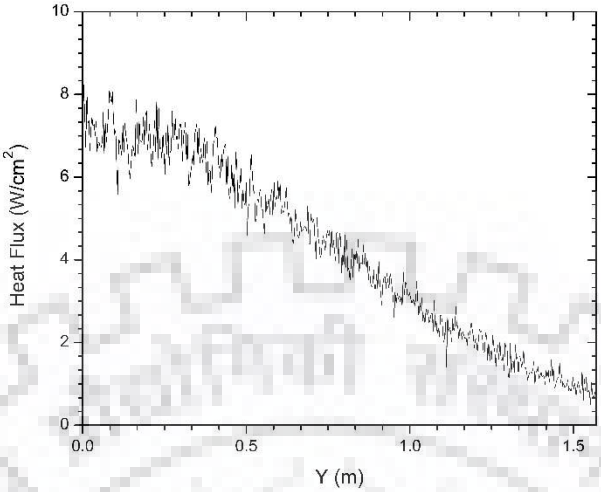

Figure 4.4 Heat flux on the surface of the cylinder

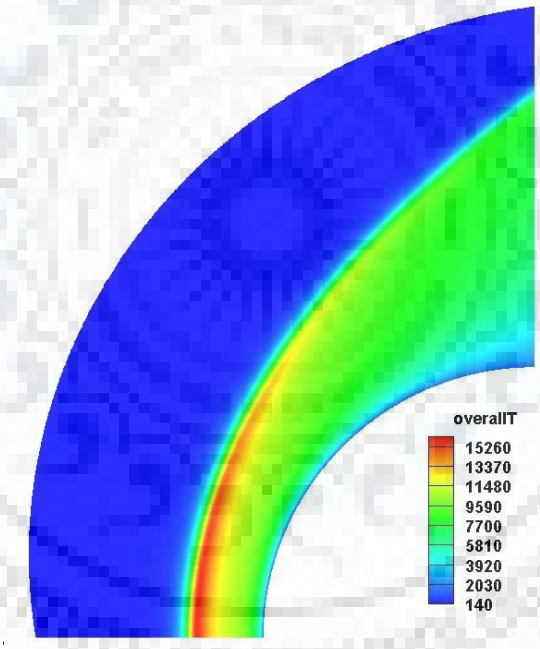

Figure 4.5 Overall Temperature contour over the cylinder

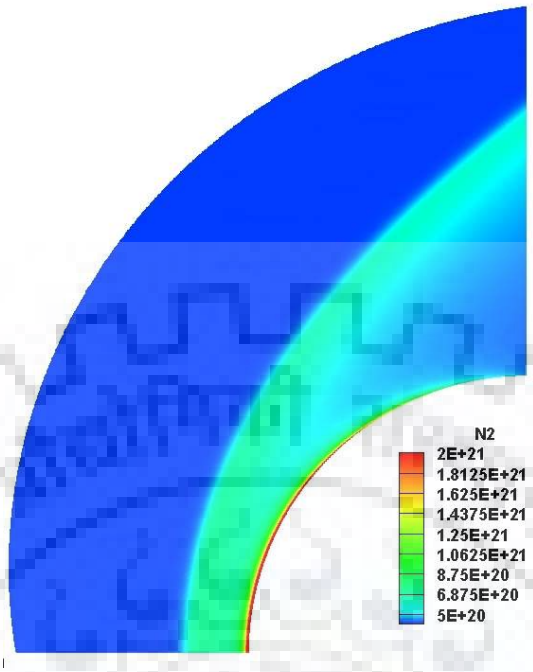

Figure 4.6 Contour of N_2 predicted using the Q-K model

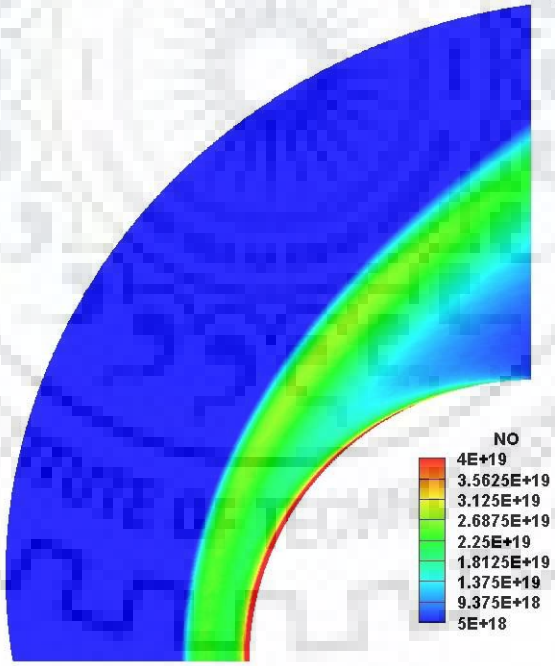

Figure 4.7 Contour of NO predicted using Q-K model

Figure 4.1 Temperature profile along the stagnation line for a non-reacting case shows the temperature profile along the stagnation line for the case with no chemical reaction. The solid lines represent our results while the dashed lines represent results obtained with the MONACO code by [92]. There is a good agreement with error within 5% in all the three temperature modes. The simulation was started with 2

million simulated particles and over 6 million simulated particles were used at the steady-state. The time step was set at $1 \times 10^{-7}\, s$. The maximum value of translational, rotational, and vibrational temperatures was found to be around 25,300, 19,500, and 16,600 K, respectively. The shock layer standoff distance is found to be 0.36 m from the stagnation point. There is a significant degree of non-equilibrium in the shock layer.

Figure 4.2 and Figure 4.3 presents the results for flow around the cylinder with chemical reactions. The MONACO code implements the TCE model; while in our code the QK model has been used. The QK model is superior to the TCE model, as unlike the TCE model the QK model does not depend on Arrhenius parameters and uses only the activation energy. The temperature plot along the stagnation line shows a similar pattern, with peak values of the maximum translational, rotational and vibrational temperatures found to be around 20,100, 13,300, and 9,900 K, respectively. The shock layer standoff distance is found to be of 0.253 m from the stagnation point.

There is a significant reduction in the peak temperatures in all modes of energy. There is an overall good agreement with the results obtained with the MONACO code; with peak temperatures matching with less than 6% error. However, the peaks in the two codes are shifted by a small distance and the shock layer thickness in the present case is slightly larger. A similar shift is observed in the plot of the velocity profile in Figure 4.2. This finding is consistent with the results reported by Scanlon *et al.* [43].

Chapter 5
DSMC APPLICATION ON THE MARTIAN RE-ENTRY VEHICLE

5.1 Non-equilibrium Chemistry Modeling in the Martian Atmosphere:

In our previous paper, we had already validated and presented reaction rates for the Martian atmosphere at a pressure of 10 pa and for a temperature range of 4000 K to 20,000 K using the QK method. These results comprise of non-equilibrium dissociation and exchange reaction rates for eight species models. To study the combined effect of various dissociation and exchange reactions given in Table 3.1, we consider a test case with a single homogenous isothermal cell of side $10\mu m$. The initially molar fraction of CO_2 and N_2 are taken as 0.97 and 0.03, respectively. The initial temperature and number density of the mixture in the cell are 20,000 K and $5.17354 \times 10^{21} m^{-3}$, respectively. The chemical reactions given in Table 3.1 are considered to study the combined effect of dissociation and exchange reaction. The time step for the iteration is taken as 10^{-10} sec, and a total of 50,000 particles were simulated. For internal energy exchange, the vibrational and rotational collision number were set as one. This is artificially done to achieve thermal equilibrium instantaneously. If the relaxation number is large it takes more time to achieve thermal equilibrium [99].

Figure 5.1 Non-equilibrium dissociation and exchange of the Martian air show the species number density fraction of various species with time. It may be observed that due to the high temperature in the shock layer, the molecular species are fully dissociated and the amount of species O is highest. The dissociation and exchange energy of CO_2 is relatively lower than other reactions, which leads to the rapid increase in the concentration of CO and O. The concentration of other species is two orders or more lower than CO. From a heat transfer point of view, the CO is the most important radiative gas in the mixture [10]. Due to the decrease in temperature with time and dissociation energy of CO being high, CO does not undergo much dissociation.

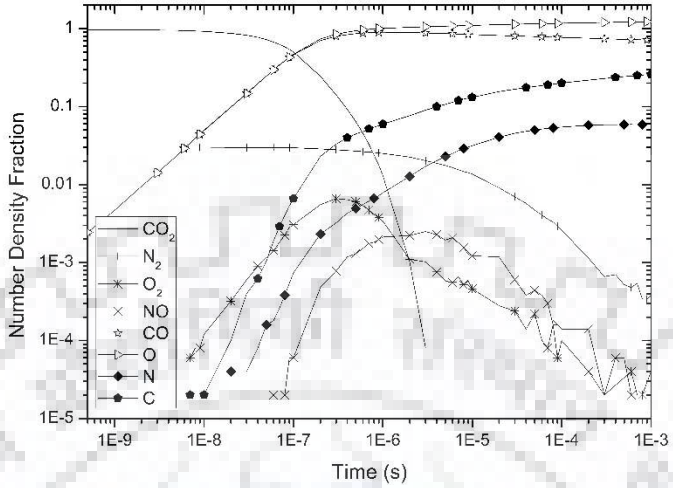

Figure 5.1 Non-equilibrium dissociation and exchange of the Martian air

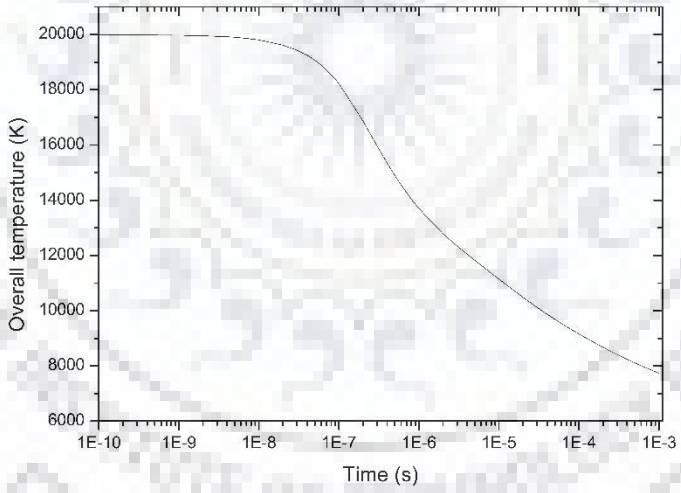

Figure 5.2 Overall temperature during the reaction from an initial temperature 20,000 K

5.2 Hypersonic Flow around a cylinder

In this section, we study a test case of hypersonic flow over a cylinder in the Martian atmosphere. The freestream conditions for the test case are taken from the work of Zuppardi [143] and are given in Table 5.1. The molar fraction of species are $X_{CO2} = 0.93399$, $X_{N2} = 0.04173$, $X_{CO} = 0.00108$, $X_{NO} = 0.00014$, $X_{O2} = 0.00176$ and $X_C = 0.00396$.

Table 5.1 Free stream condition for hypersonic flow over the blunt-body for Martian atmosphere [143]

Parameter	Value	unit
Free stream temperature	50	K
Number Density	3.026×10^{20}	molecule/m^3
Free stream velocity	4667	m/s
Mach number	41.8	
Altitude	90	km
Cylinder Radius	0.2	m
Knudsen Number	2.01×10^{-3}	

The rarefied flow was simulated on a mesh with a total of 90,000 computational cells. In the first study, the effect of chemical reactions was not considered and only rotational and vibrational relaxations were considered. The simulation was started with 1 million particles and it reached around 3 million particles at steady-state conditions. The time steps were taken as 1×10^{-7} s.

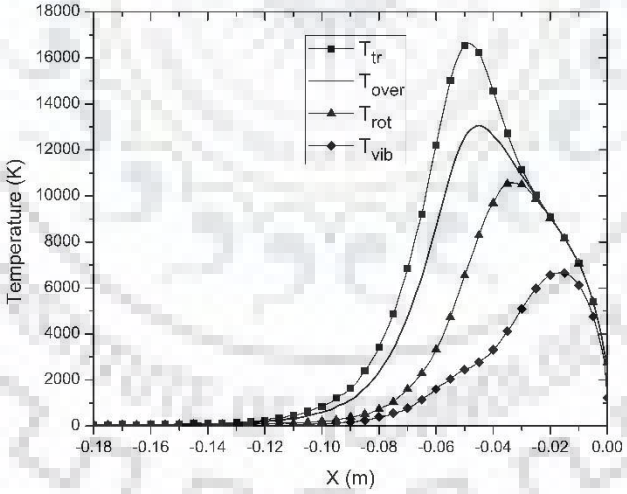

Figure 5.3 Profile of temperature along the stagnation line without chemistry model

Figure 5.1 shows the temperature plot along the stagnation line, the maximum value of translational, rotational, and vibrational temperatures were found to be around 16,640, 10,570 and 6,670 K, respectively. The shock layer standoff distance is located at a position of 0.1 m from the stagnation point.

In the second case, the effect of dissociation and exchange reactions were considered. All the chemical reactions, including backward reactions given in Table 3.1 Chemical reaction list and their Arrhenius coefficient for reaction rate calculation, were considered for the simulation.

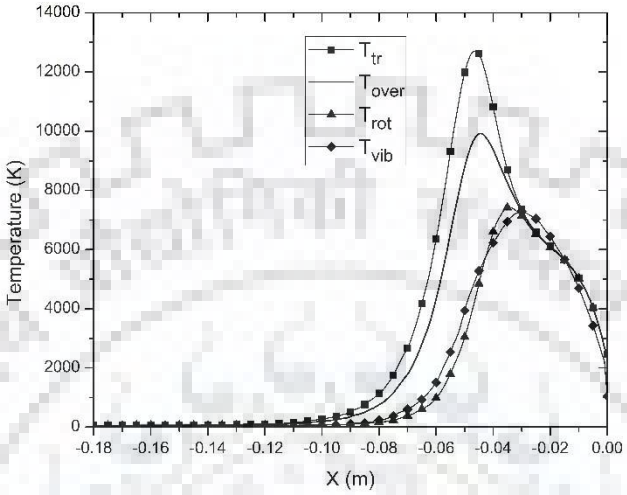

Figure 5.4 Profile of temperature along the stagnation line with chemistry model

Figure 5.4 shows the temperature plot along the stagnation line. The maximum value of translational, rotational, and vibrational temperatures were found to be around 12,720, 7,420, and 7,290 K, respectively. The shock layer standoff distance is located at a position of 0.9 m from the stagnation point. The chemical reactions tend to reduce all temperatures significantly, and only slightly reduce the shock layer thickness.

The convective heat flux over the surface of CEV is calculated using

$$\boldsymbol{q} = {}^{1}/_{2}\,\overline{mnc'^{2}\boldsymbol{c}} + \overline{n\varepsilon_{int}\boldsymbol{c}} \qquad 5.1$$

Where m and n represent the molecular mass and number density of the species, respectively. $\boldsymbol{c}$ and c' represents pre and post-collision velocity, respectively and ε_{int} represents the internal energy of the molecular species which is the sum of rotational (ε_{rot}) and vibrational energy (ε_{vib}) of the molecular species.

$$\varepsilon_{int} = \varepsilon_{rot} + \varepsilon_{vib} \qquad 5.2$$

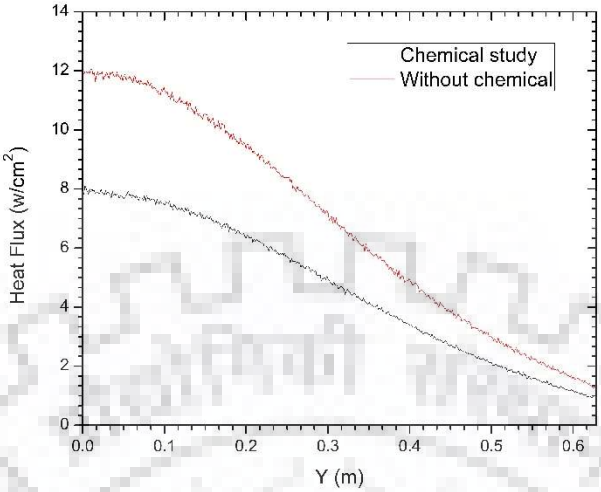

Figure 5.5 Heat flux on the surface of the cylinder from the stagnation point

Figure 5.5 shows the convective heat flux on the surface of the cylinder with and without including the chemical reaction. It can be observed that there is a significant reduction in the convective heat flux at the stagnation point. The energy required for the chemical reactions is obtained from the translational, rotational and vibrational energy modes of the molecules; more the endothermic exchange and dissociation reaction takes place more the difference will increase between these two curves.

5.3 Hypersonic Flow around a Crew Exploration Vehicle

The free stream condition for the Martian atmosphere re-entry is given in Table 5.2.

Table 5.2 Free stream condition for Martian atmosphere re-entry at the hypersonic speed [28]

Parameter	Value	unit
Free stream velocity	6500, 5000	m/s
Number Density	5.17358×10^{21}	molecule/m^3
temperature	140	K
Mach number	34, 26	
Molar Fraction		
CO_2	0.97	
N_2	0.03	

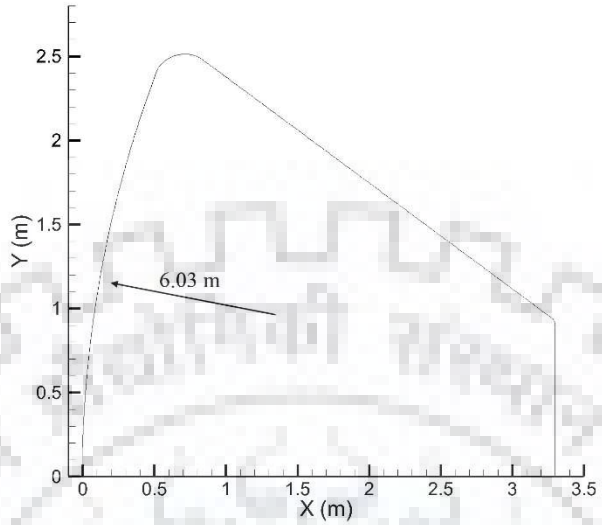

Figure 5.6 Configuration of Crew Exploration Vehicle (CEV)

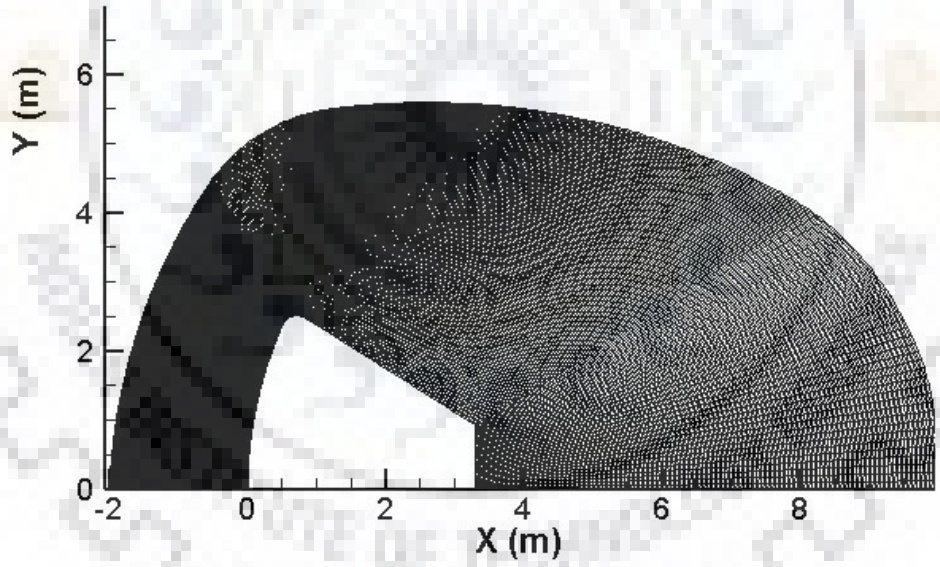

Figure 5.7 Mesh over CEV

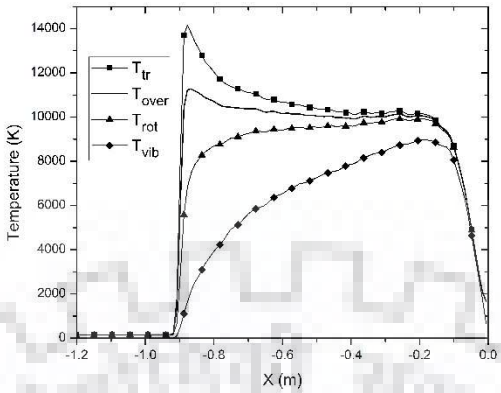

Figure 5.8 Temperature plot along the stagnation line without chemical reaction for 5 km/s re-entry speed

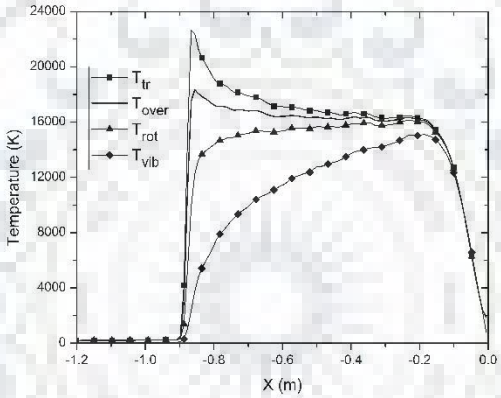

Figure 5.9 Temperature plot along the stagnation line without chemical reaction for 6.5 km/s re-entry speed

The configuration of the CEV used for the simulation is shown in Figure 5.6 and Figure 5.7 shows the computational mesh for the case.

We first study the case with rotational and vibrational relaxation and no chemical reactions. Two different speeds of the spacecraft were considered. Figure 5.8 and Figure 5.9 show the temperature plots along the stagnation line of the spacecraft for the two cases of free stream speed of 5.5 km/s and 6.5 km/s. The maximum translational, rotational and vibrational temperature for 6.5 km/s entry speed are 22,642, 16,124 and 15,094 K, respectively; while for 5 km/s entry speed these values are 14,168, 9,919 and 8,981 K respectively. The shock layer thickness for the two cases was found to be around 86 cm and 88 cm, respectively. Figure 5.10 shows the gauge pressure along the stagnation line for the two cases. The maximum pressure occurs at the stagnation point, and its value for the 6.5 km/s case is almost 1.5 times the value for the 5 km/s case. There is no significant change in the shock layer thickness for the two cases.

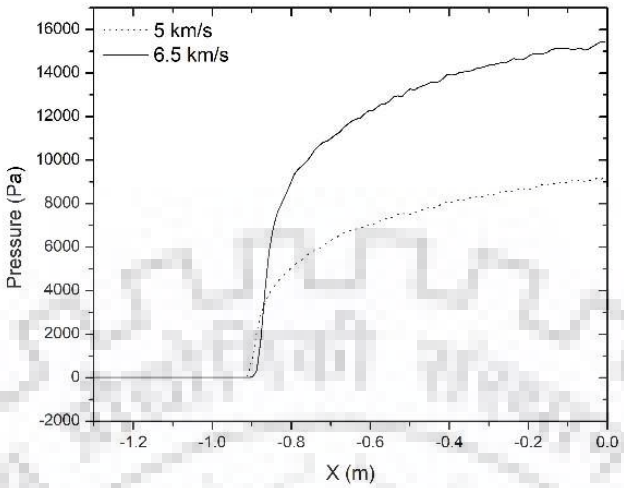

Figure 5.10 Pressure plot along the stagnation line

Next, we included the effect of chemical reactions into the flow problem. The effect of chemical reactions on the temperature in the shock layer has already been discussed for the case of the homogeneous cells. In the non-equilibrium shock layer, the temperature is maximum at some distance away from the stagnation point, followed by a plateau region with almost uniform temperature, and finally decreasing sharply at the wall. The sharp decline in temperature near the stagnation point leads to the recombination of atoms. However, due to the high degree of non-equilibrium and low residence time, the rate of recombination may be low. In this study, we have ignored the recombination reactions.

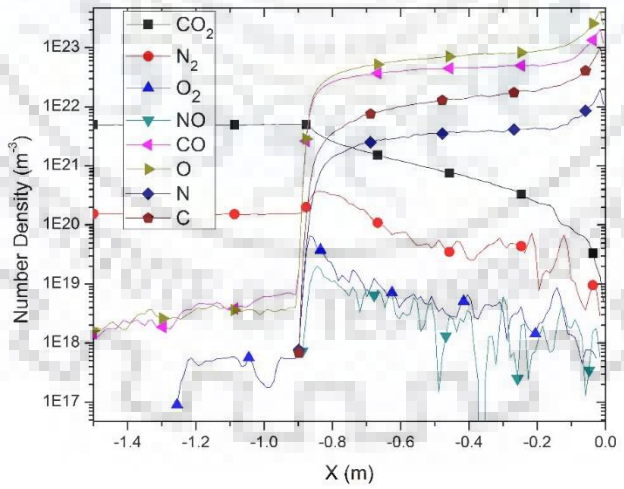

Figure 5.11 Number density plot along the stagnation line for 6.5 km/s entry speed

Figure 5.11 shows the number density plot of various species along the stagnation line. As expected, the number density of CO_2 decreases due to dissociation and exchange reaction, while that of CO and O

increases. The shock layer thickness remains unchanged when compared to the case of no chemical reactions for the same speed. The overall temperature in the shock layer peaks at a value of around 7,520 K, which is around 10,800 K lower than the case of no chemical reaction. Thus, there is a significant reduction in temperatures due to chemical reactions. Bansal *et al.* [28] did a similar study on the Martian reentry vehicle with similar geometry and free stream conditions. They observed an overall temperature of 8,200 K and a shock layer thickness of 30 cm. We observed that the DSMC code predicts lower temperatures and higher shock layer thickness than the continuum Navier-Stokes solver. Sohn *et al*. [144] observed similar trends for the Earth re-entry of stardust spacecraft with the SMILE and DPLR code [68]. The difference in the shock layer thickness and temperature is due to the different energy exchange/chemical reactions used in the DSMC and the CFD codes. The maximum values of molecule CO and O concentration within the shock layer are predicted close to those of that CFD results. Number densities of molecule CO and O are, however, observed to decrease near the surface because the DSMC method assumed a fully diffused surface condition. Figure 5.12 shows the contour plot of the overall temperature for the entry speed of 6.5 km/s.

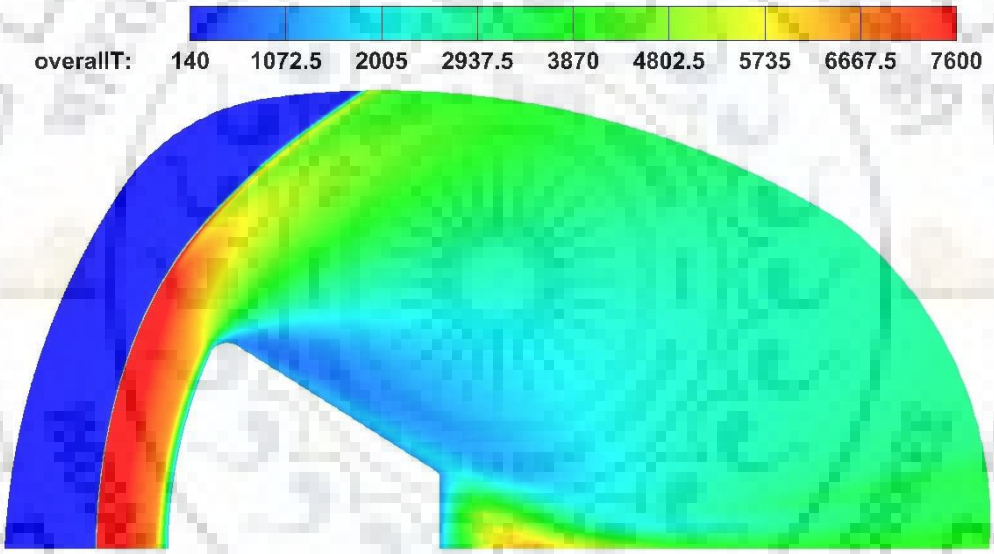

Figure 5.12 Contour plot of overall temperature for the entry speed of 6.5 km/s

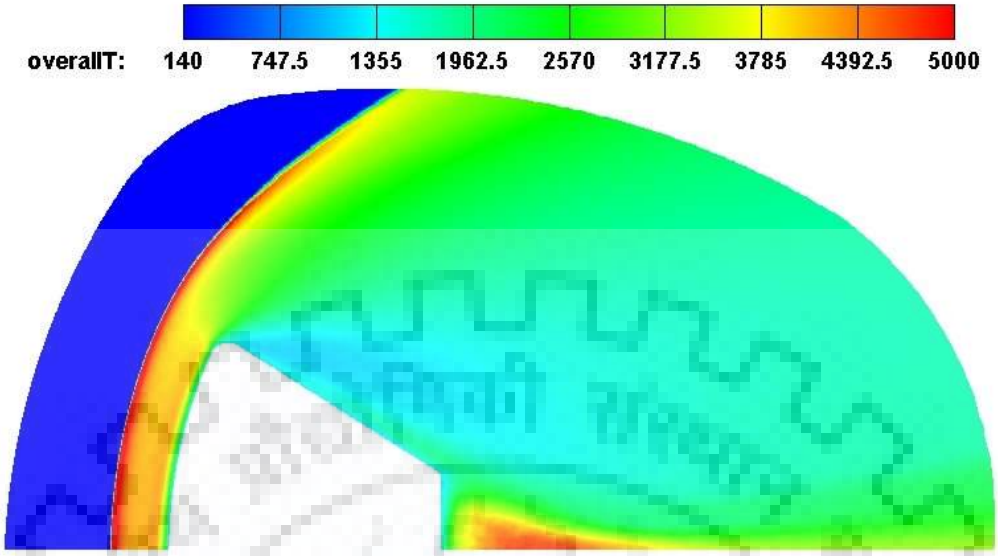

Figure 5.13 Contour plot of overall temperature for the entry speed of 5 km/s

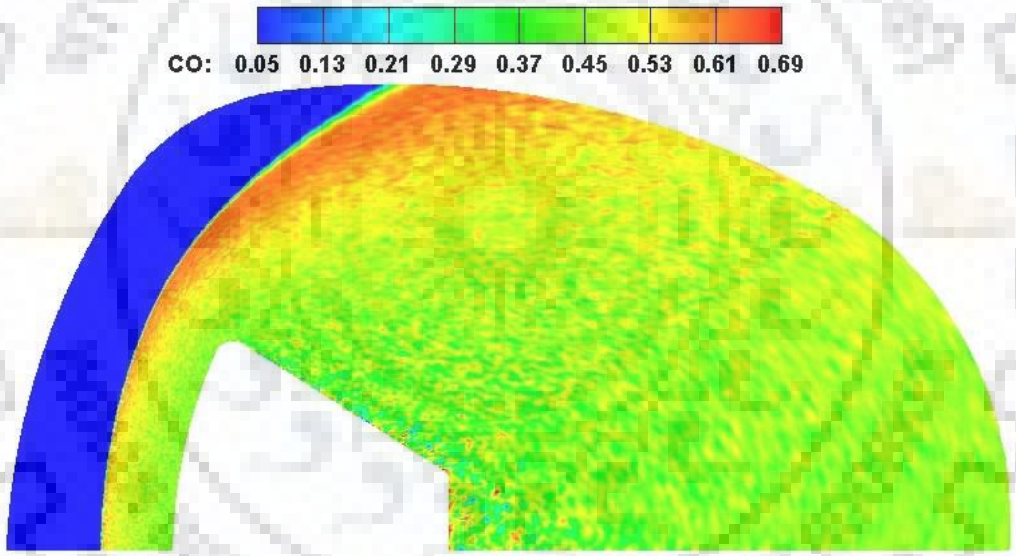

Figure 5.14 Contour of mass fraction of CO for 6.5 km/s entry speed

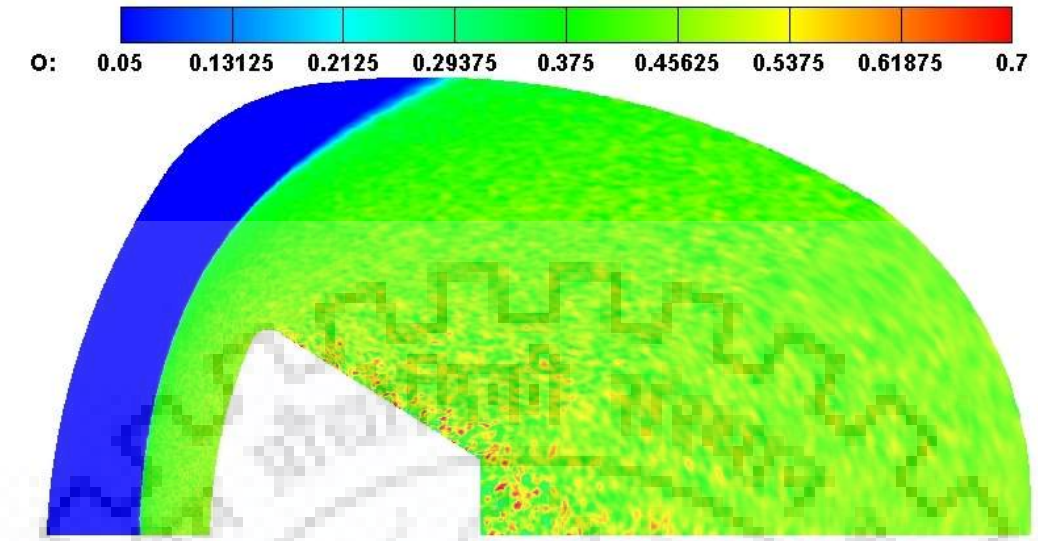

Figure 5.15 Contour of mass fraction of O for 6.5 km/s entry speed

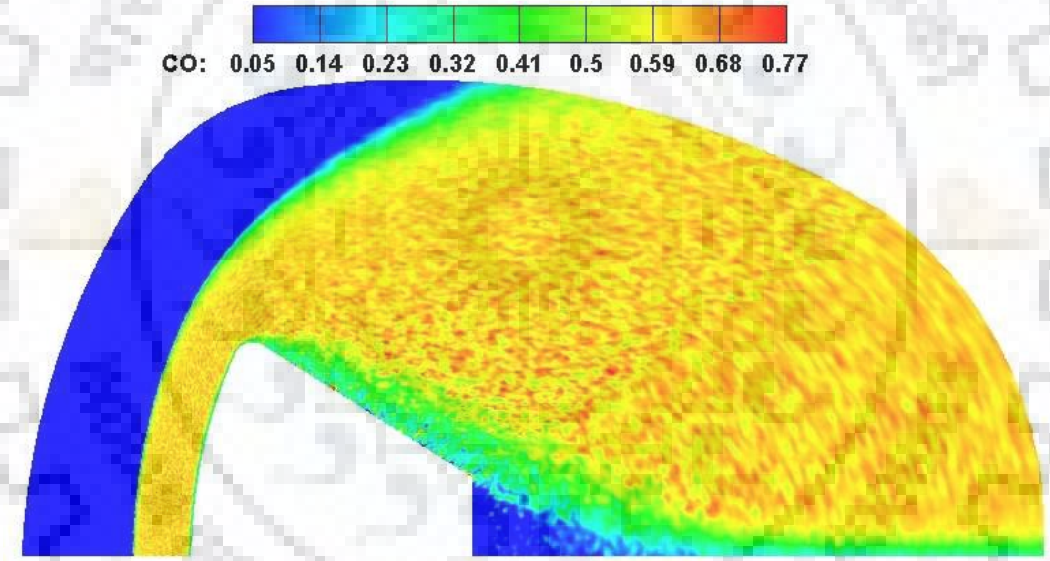

Figure 5.16 Contour of mass fraction of CO for 5km/s entry speed

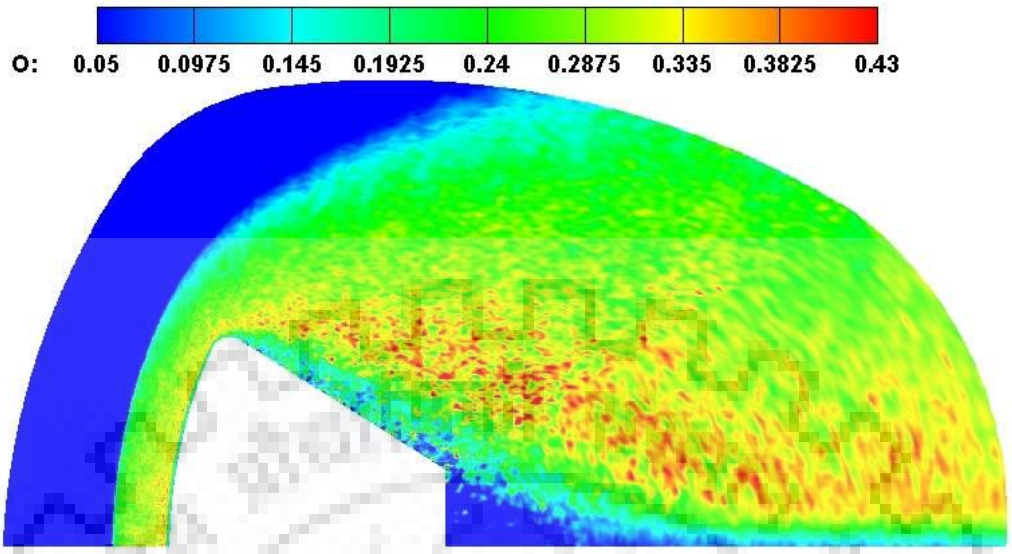

Figure 5.17 Contour of mass fraction of O for 5 km/s entry speed

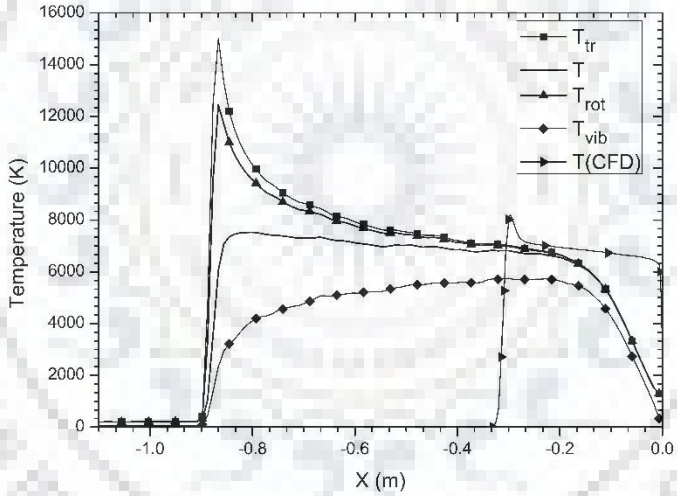

Figure 5.18 Temperature plot along stagnation line with chemical reaction 6.5 km/s entry speed

For the case of free stream velocity of 5 km/s, the temperatures in the shock layer are lower and, therefore, CO_2 is less dissociated. Figure 5.19 shows the number density of various species along the stagnation line. The shock layer thickness for this case is around 70 cm. Again, we observe significant CO in the shock layer, which may contribute to significant radiative heat transfer. However, in the CFD study done by Bansal *et al.* [28], the shock layer temperatures were observed to be higher for the same test case. Again, the maximum values of molecule CO and O concentration within the shock layer are predicted close to those of the CFD. The temperature variation along the stagnation line is shown in Figure 5.20, with a maximum value of the translational temperature of 9,150 K.

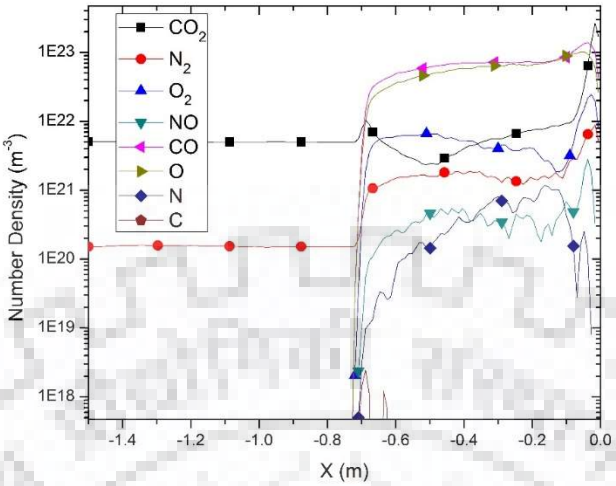

Figure 5.19 Number density plot along the stagnation line for entry speed of 5 km/s

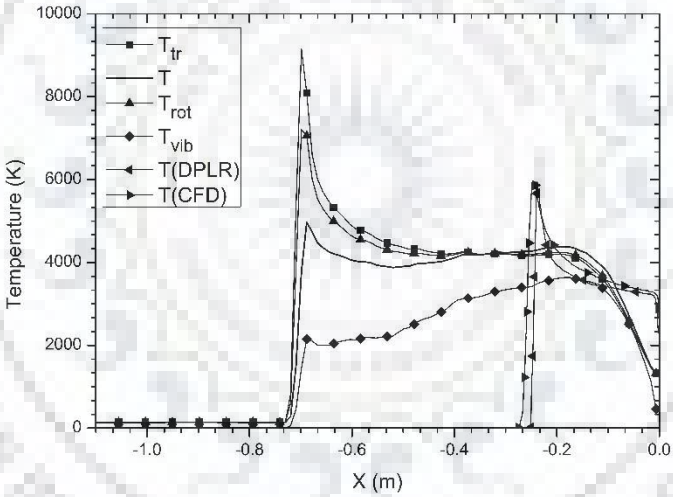

Figure 5.20 Temperature plot along the stagnation line with the chemical reaction for 5 km/s entry speed

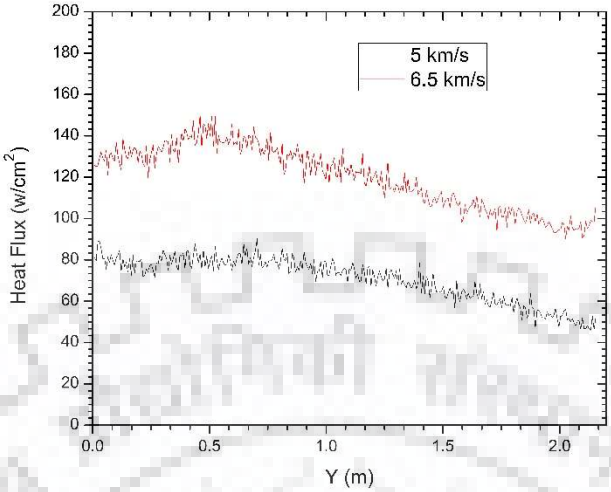

Figure 5.21 Heat Flux on the front surface of the CEV

Figure 5.21 shows the convective heat flux along the front surface of the CEV from the stagnation point. There is an increase in the heat flux values for distance up to 0.5 m followed by a continuous decline in values for both the cases. The maximum heat flux was found to be 150.0 and 90 W/cm^2 for 6.5 and 5 km/s case, respectively.

Chapter 6
RADIATION MODELS

Optimisation of large utility boilers is an imperative demand of the day. Current optimisation strategies are directed at extending the lifetime, increasing thermal efficiency and reducing the pollutant emissions from large furnaces. Coal is an important energy resource for meeting the further demand for electricity, as coal reserves are much more abundant than those of other fossil fuels. Efficient use of pulverised coal is crucial to the utility industry. To achieve higher combustion efficiency, the major influencing factors such as the particle size distribution, gas and particle temperatures, local heat release, local oxygen concentration, kinetic parameters for coal de-volatilization and char oxidation, radiative heat transfer, char properties should be understood thoroughly [145–148].

Pulverised coal-fired boiler furnace is one of the most crucial equipment in a typical thermal power plant; wherein the furnace has to facilitate and accommodate several disturbances such as variations in fuel quality, part load operations, coal blending options, slagging and fouling of heat transfer surfaces towards generating electric power under specified conditions.

With the recent supply-demand gap of coal, blending of Indian coal with imported coal, which is characterized by high volatiles, high moisture content, and high sulphur content, becomes almost unavoidable. This situation is even more challenging with the use of supercritical technology as bulk fluid temperature in furnace water walls increases throughout its height, which in turn affects the safe and allowable metal temperatures of the water wall.

Designing of the furnace for such conditions is very challenging and needs detailed mathematical models and techniques to predict the performance, safe limits of operation and compliance to the environmental guidelines. In addition, furnace performance has a great influence on important parameters like boiler efficiency, super-heater, and re-heater outlet temperatures and spray flows that have a great bearing on overall power plant efficiency.

A large number of approximate radiative transfer solvers have been develop for complex three-dimensional geometries. The inaccuracy in the solution of the radiative transfer equation (RTE) with approximate radiation models such as the discrete ordinate method, zonal method and the spherical harmonic method is discussed in detail in the textbook of Modest [149] and Howell [150].

The zonal method is one of the oldest numerical discrete mathematical methods to solve the radiative heat transfer Problem in industrial furnaces. Hottel and Cohen have created this model first in 1935 for analysing the radiation heat transfer in an enclosure containing grey gas with certain properties [151]. Later, Hottel and Sarofim [152] extended this method to more complex geometries. Ever since, this model has been widely used by researchers for modelling industrial radiative enclosures such as boiler furnaces [149,153].

The Zonal method works by dividing an enclosed chamber into a number of isothermal, isotropic and homogeneous surface and gas zones and assumes the radiative properties to be uniform in each zone. The amount of radiation exchange between each pair of zones is defined by using a special coefficients named “Direct Exchange Area”. If the temperature distribution is available, a radiative energy balance can be written for each zone. The radiative balance includes the radiative exchange between a given zone and

every other zone of the system [149]. The model returns heat fluxes to the surface zones and radiative energy source term for the volume zones. The net radiative heat energy is added to the overall energy balance in each zone.

To overcome the high computational cost of the Zonal method, the imaginary planes method (IPM) was developed [154–156]. The imaginary planes method is essentially a simplified zonal method. The radiation space is divided into zones in the same manner. If the enclosure is divided into one zone, the IPM method is equivalent to the zonal method. The volume zones are bounded by real surfaces along the walls of the enclosure and by "imaginary planes" in the radiation field. Each volume zone has a direct view only of its boundaries, i.e. direct radiation exchange takes place only inside the volume zones. The adjacent volume zones are linked through radiative fluxes crossing the imaginary planes.

The Imaginary Plane Method (IPM) was used by Charette et al. [154] to check the accuracy of the IPM method. Haidekker et al. [156] employed the IPM, zonal and the DOM method to 3-D complex enclosures with gray gas conclusion.

Combustion process produces combustion gases, such as water vapour, carbon dioxide, carbon monoxide, sulphur dioxide, nitrogen dioxide, and others. The partial pressures of these gases in the combustion products are determined by the type of the fuel used and the conditions of the combustion environment, such as fuel-air ratio, total pressure and ambient temperature. These gases do not scatter radiation significantly, but they are strong selective absorbers and emitters of radiant energy.

Molecular gases absorb and emit radiation over a range of narrow spectral lines, which may overlap and form so-called vibration-rotation bands. The resulting absorption coefficient spectrum oscillates wildly within each band, and is zero between bands. Similarly, absorption and scattering properties of particulates may also oscillate strongly across the spectrum. However, if particles of varying sizes are present, as is usually the case, the spectral oscillations tend to be damped out [149].

Employing detailed information of spectral extinction coefficient from high-resolution HITRAN [157] and HITEMP [158] databases, accurate determination of radiative fluxes and sources can be made. However, this requires approximately one million spectral evaluations for such "line-by-line" calculations, making them impractical for all applications except as benchmarks for the evaluation of more approximate models.

Hottel and Sarofim developed the concept of weighted-sum-of-grey-gases (WSGG) for applications of the zonal method [152]. In this method the non-grey gas is replaced by a number of grey gases, and the total heat flux is found by adding the fluxes of all grey gases. Modest [159] generalized the WSGG model for use with any arbitrary RTE solution method, although he assumed that the absorption coefficients are spatially independent (homogeneous media), while weights were allowed to depend on temperature. In its original form, the WSGG model suffers from serious limitations. In the original WSGG model, the absorption coefficients and weight factor for each grey-gas are found from total emissivity data, rather than from the detailed spectroscopic database. Only the weight functions are assumed to vary with temperature and the absorption coefficients are assumed to be independent of temperature. The WSGG parameters were evaluated for CO_2-H_20 and CO_2-H_20-soot mixture for fixed partial pressure ratios, P_{H2O}/P_{CO2}=1 or 2 (P_{H2O} and P_{CO2} are partial pressures of H_2O and CO_2, respectively,), which is typical for combustion of methane. For other fractions of partial pressures, the data for WSGG is not available. Further, the WSGG parameters were evaluated by minimization of least square error in the emissivity of a homogeneous gas column with length scale ranging from few centimetres to few meters [160–163].

There is simply no promise for parameters to be valid for inhomogeneous paths and larger length scales. Also, the method was limited to black boundaries and non-scattering medium.

The WSGG parameters should be tailored to the medium at hand, depending on composition, pressure levels, temperature levels, and length scale. Only if the fit is optimized will one be able to achieve acceptable accuracy. Unfortunately, the curve fit is a nonlinear one, and the curve fitting effort may become more involved than the heat transfer calculations themselves [149].

Today, the WSGG method can also be applied to reflecting (albeit grey) walls, to variable absorption coefficients (non-homogeneous path) as long as they obey the scaling approximation, and much more accurate WSGG parameters can be obtained from high-resolution databases.

Denison and Webb improved on the WSGG model by developing the Spectral-Line Based Weighted-Sum-of-Grey-Gases (SLW) model with absorption coefficients based on detailed spectral line data. In this model, the absorption coefficient is used as the basic radiative property rather than transmissivity or band absorptance. Denison *et al.* also extended the SLW model to non-isothermal and non-homogeneous media [164–168].

It was later demonstrated by Zhang and Modest that the WSGG and SLW models are step approximations to the smoother and more accurate full-spectrum *k*-distribution model [169]. It has been shown that, for a small spectral interval (narrow-band) in a homogeneous medium, the absorption coefficients can be reordered into a monotonic *k*-distribution, which yields exact results at a fraction of the computational cost required by line-by-line methods. The idea behind the reordering method is to replace the spectral integration over wavelengths with integration over the absorption coefficient. Recently, reordering concepts have been applied to the full spectrum and inhomogeneous media [170,171]. While the *k*-distribution method is exact for a homogeneous medium, errors may occur when applied to strongly inhomogeneous media. The problem of inhomogeneity is addressed by using one of two different approaches: the scaling approximation or the assumption of a correlated k-distribution [164,169,171–174].

The overall objective of this study is to develop the Imaginary Plane Model (IPM) in OpenFOAM for three-dimensional geometry of arbitrary shape and compare the results for a furnace with other solution methods such as the zonal and the P_1 method. The spectral properties of the participating gases are treated with the WSGG and the full spectrum k-distribution model.

1. Methodolog

In this section, we present the theory of the zonal and the IPM method. The zonal method has been applied extensively in various areas of heat transfer and the theory of this method is easily available in standard text on Radiative Heat Transfer. However, the IPM method has not gained much importance. Here we present the theory of both the methods for the sake of completeness and comparison between the two methods.

6.1 Zonal Method

In the zonal method, the computational domain is divided into a number of isothermal, isotropic and homogeneous surface and volume zones. The radiation exchange between each pair of zones is defined by a special coefficient named "Direct Exchange Area". The radiative balance includes the radiative exchange between a given zone and every other zone of the system [149]. The model returns heat fluxes to the surface zones and radiative energy source term for the volume zones. The energy balance for a surface zone is written as [149],

$$\sum_j \left(\frac{\delta_{ij}}{\epsilon_j} - \frac{(1-\epsilon_j)}{\epsilon_j} \frac{\overline{s_i s_j}}{A_j} \right) h_{sj} - \sum_j \frac{\overline{s_i g_j}\,\omega_j}{4\kappa_j V_j} h_{gj} = \sum_j \overline{s_i s_j}\,\epsilon_j E_{sj} + \sum_j \overline{s_i g_j}(1-\omega_j) E_{gj} \qquad \text{i=1→N} \quad 6.1$$

where we have eliminated the radiosity to obtain the above equations. The energy balance for a volume zone is written as,

$$-\sum_j \frac{\overline{s_j g_i}(1-\epsilon_j)}{\epsilon_j A_j} h_{sj} + \sum_j \left(\frac{\delta_{ij}}{(1-\omega_j)} - \overline{g_i g_j} \frac{\omega_j}{4\kappa_j V_j} \right) h_{gj} = \sum_j \overline{s_j g_i}\,\epsilon_j E_{sj} + \sum_j \overline{g_i g_j}(1-\omega_j) E_{gj} \qquad \text{i=1→K} \quad 6.2$$

where *N* is the total number of surface zones and *K* is the total number of volume zones. Note that in the above equation $h_s = \varepsilon A H_s$ and $h_g = \kappa V G$. Heat flux at the wall and source term for the volume zone are related as

$$Q_{si} = \epsilon_i A_i E_{si} - h_{si} \qquad 6.3$$

$$Q_{g_i} = 4\kappa_i V_i E_{g_i} - h_{gi}$$

Figure 6.1 shows the division of a computational domain into surface and volume zones. Energy emitted from a volume zone is taken as positive; while the energy absorbed in the volume is taken as negative. The zonal method incorporates the geometrical factors through the direct exchange areas (DEAs). The direct-exchange areas may be considered as a measure of the effect of the size and shape of the system as well as its radiative properties. The reflection from the wall and scattering within the medium is not take into account. They express numerically the way a zone sees another zone of the enclosure directly.

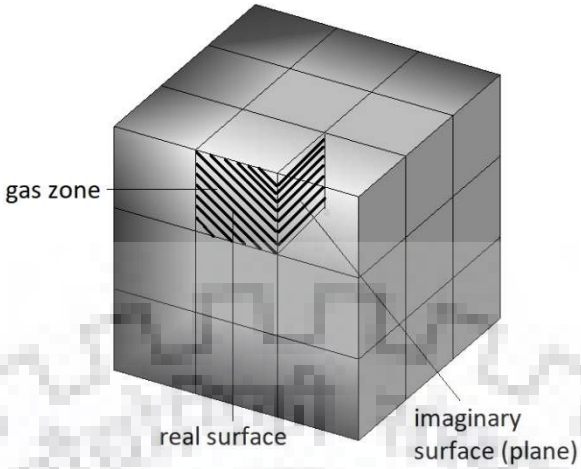

Figure 6.1 Schematic of Volume and Surface Zone

The expressions for energy balance and exchange areas are equally valid for grey absorption coefficient as well as on spectral basis. Unfortunately, the zonal method is not well suited for non-grey media. However, Hottel et al. [152] extended the Zonal method with the WSGG model to enable the treatment of real gases.

6.2 Imaginary Plane Model (IPM)

In this method, a volume zones is bounded by real surfaces along the walls of the enclosure and by "imaginary planes" in the radiation field, as shown in Figure 6.1. Each volume zone has a direct view of only its own boundaries, i.e. direct radiation exchange takes place only inside a single volume zone. The adjacent volume zones are linked through radiative fluxes crossing the imaginary planes.

Energy Balance: The total amount of radiant energy exchange from a real surface can be written as

$$Q_k = A_k(J_k - H_{ki}) \tag{6.4}$$

where J_k and H_k are outgoing and incoming radiant energy from and to surface *k*, respectively. Assuming there is only one isolated gas zone, the energy balance for a surface and a volume zone can be written as [149]:

$$\sum_j \left(\frac{\delta_{ij}}{\epsilon_j} - \frac{(1-\epsilon_j)}{\epsilon_j}\frac{\overline{s_i s_j}}{A_j}\right) h_{sj} - \frac{\overline{s_i g}\,\omega}{4\kappa V} h_g = \sum_j \overline{s_i s_j}\epsilon_j E_{sj} + \overline{s_i g}(1-\omega)E_g \qquad \text{i=1}\rightarrow N \quad 6.5$$

$$-\sum_j \frac{\overline{s_j g}(1-\epsilon_j)}{\epsilon_j A_j} h_{sj} + \left(\frac{1}{(1-\omega)} - \overline{gg}\,\frac{\omega}{4\kappa V}\right) h_g = \sum_j \overline{s_j g}\epsilon_j E_{sj} + \overline{gg}(1-\omega)E_g \tag{6.6}$$

Thus,

$$h_g = \frac{\sum_j \frac{\overline{s_j g}(1-\epsilon_j)}{\epsilon_j A_j} h_{sj} + \sum_j \overline{s_j g}\epsilon_j E_{sj} + \overline{gg}(1-\omega)E_g}{\frac{\beta}{\kappa}\left(1 - \overline{gg}\frac{\omega}{4\beta V}\right)} \quad 6.7$$

Substituting Eq. 6.7 into Eq. 6.5 and simplifying:

$$\sum_j \left(\frac{\delta_{ij}}{\epsilon_j} - \frac{(1-\epsilon_j)}{\epsilon_j}\frac{\overline{s_i s_j}}{A_j}\right) h_{sj} - \frac{\overline{s_i g}\omega}{4\kappa V}\left[\frac{\sum_j \frac{\overline{s_j g}(1-\epsilon_j)}{\epsilon_j A_j} h_{sj} + \sum_j \overline{s_j g}\epsilon_j E_{sj} + \overline{gg}(1-\omega)E_g}{\frac{\beta}{\kappa}\left(1 - \overline{gg}\frac{\omega}{4\beta V}\right)}\right] \quad \text{i=1}\rightarrow N \quad 6.8$$
$$= \sum_j \overline{s_i s_j}\epsilon_j E_{sj} + \overline{s_i g}(1-\omega)E_g$$

$$\frac{h_{si}}{\epsilon_i} + \sum_j \left(-\frac{(1-\epsilon_j)}{\epsilon_j}\frac{\overline{s_i s_j}}{A_j}\right) h_{sj} - \alpha\left[\sum_j \frac{\overline{s_j g}(1-\epsilon_j)}{\epsilon_j A_j} h_{sj}\right] \quad \text{i=1}\rightarrow N \quad 6.9$$
$$= \sum_j \overline{s_i s_j}\epsilon_j E_{sj} + \overline{s_i g}(1-\omega)E_g + \alpha\left(\sum_j \overline{s_j g}\epsilon_j E_{sj} + \overline{gg}(1-\omega)E_g\right)$$

where,

$$\alpha = \frac{\overline{s_i g}\omega}{4\beta V\left(1 - \overline{gg}\frac{\omega}{4\beta V}\right)} \quad 6.10$$

On simplifying Eq. 6.9**Error! Reference source not found.**

$$\frac{h_{si}}{\epsilon_i} - \sum_j \frac{(1-\epsilon_j)}{\epsilon_j A_j}\left(\overline{s_i s_j} + \alpha\overline{s_j g}\right) h_{sj} = \sum_j \left(\overline{s_i s_j} + \alpha\overline{s_j g}\right)\epsilon_j E_{sj} + \left(\overline{s_j g} + \alpha\overline{gg}\right)(1-\omega)E_g \quad \text{i=1}\rightarrow N \quad 6.11$$

Note here $h_s = \varepsilon AH$. Thus, the above equation can be written in terms of total incoming energy as:

$$A_i H_i - \sum_j (1-\epsilon_j)\left(\overline{s_i s_j} + \alpha\overline{s_j g}\right) H_j = \sum_j \left(\overline{s_i s_j} + \alpha\overline{s_j g}\right)\epsilon_j E_{sj} + \left(\overline{s_j g} + \alpha\overline{gg}\right)(1-\omega)E_g \quad \text{k=1}\rightarrow N \quad 6.12$$

$$A_i H_i = \sum_j \left(\epsilon_j E_{sj} + (1-\epsilon_j)H_j\right)\overline{s_i s_j} + \sum_j \alpha\overline{s_j g}\left(\epsilon_j E_{sj} + (1-\epsilon_j)H_j\right) \quad \text{k=1}\rightarrow N \quad 6.13$$
$$+ \left(\overline{s_j g} + \alpha\overline{gg}\right)(1-\omega)E_g$$

The above expression in terms of radiosity can be written as:

$$\frac{A_i(J_i - \epsilon_i E_{si})}{(1-\epsilon_i)} = \sum_j J_j \overline{s_i s_j} + \sum_j \alpha\overline{s_j g} J_j + \left(\overline{s_j g} + \alpha\overline{gg}\right)(1-\omega)E_g \qquad 6.14$$

$$A_i J_i = \epsilon_i A_i E_{si} + (1-\epsilon_i)\left\{\sum_j J_j \overline{s_i s_j} + \sum_j \alpha\overline{s_j g} J_j + \left(\overline{s_j g} + \alpha\overline{gg}\right)(1-\omega)E_g\right\} \qquad 6.15$$

where the following equality is assumed

$$J_i = \epsilon_i E_{si} + (1-\epsilon_i)H_i \qquad 6.16$$

Now, for an imaginary plane the incoming radiative energy can be calculated using the same expression; however, the outgoing radiation cannot be calculated as a contribution from emission and reflection of the incoming radiation. Since there is no real surface present, the outgoing radiation from any imaginary plane is simply the incoming radiation from the adjacent cells.

Linking Procedure: In Figure 6.2, the notation of the faces of a hexahedral zone is given, and the faces are numbered from one to six. In the figure, two zones A and B are connected by an imaginary face. The face 2 of zone *A* and face 4 of zone *B* are common. The energy balance at the imaginary faces dictates that the incoming radiative energy on face 4 of zone B is same as outgoing radiative energy from face 2 of zone A, i.e.

$$J_2^A = H_4^B; \qquad H_2^A = J_4^B \qquad 6.17$$

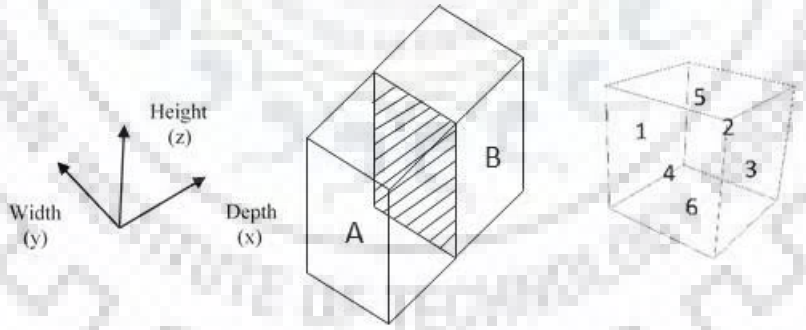

Figure 6.2 Linking between zones at imaginary surface

Thus, an energy balance for an imaginary surface can be written from Eq. 6.17 and Eq. 6.8 as:

$$\sum_j J_j \overline{s_i s_j} + \sum_j \alpha\overline{s_j g} J_j - A_2 J_4^B = -\left(\overline{s_j g} + \alpha\overline{gg}\right)(1-\omega)E_g \qquad 6.18$$

Eq. 6.15 and 6.18 can be assembled in a global matrix and solve for unknown outgoing radiative energy, J_k, for all real and imaginary surfaces. Once the radiosities are known for all surfaces, net radiative energy flux on real surfaces can be calculated from Eq. 6.4. The radiative source term in a volume zone is determined by adding net radiative heat rates on all surfaces (imaginary or real) of a zone as:

$$\nabla . q = \sum_{j=1}^{6} Q_j \qquad 6.19$$

The IPM method requires calculation of direction exchange area within a single volume zone and, therefore, simplified ray tracing algorithm in the individual zones is sufficient for the calculation of exchange areas. Computation of direct exchange areas using the Monte Carlo technique takes 95% of the computation time of the zonal method. The calculation time further increases with decreasing surface emissivity, but it is most influenced by the gas absorption coefficient.

Further, using more and more divisions the IPM method loses accuracy. The computational time increases only very slightly with the increase in number of zones, which is due to the iterative solution technique of the linear equations containing the imaginary fluxes. Hence, the IPM method is not suggested to be used in case of high number of zonal divisions [175]. The detailed procedure for the ray tracing using Monte Carlo Method is explained in Appendix A.

6.2.1 Monte-Carlo Ray Tracing

The calculation of direct exchange areas in an absorbing/scattering medium is not straightforward. Maruyama *et al.* [176] developed a ray tracing method for calculating view factors in arbitrary 3-D enclosures. The imaginary planes method requires ray tracing only within the individual cells. The Monte Carlo method is a statistical numerical method. An excellent discussion on the method is given in Siegel and Howell (1983). In this technique, radiation exchange modelled by the emission and absorption of discrete amounts of energy, called "energy bundles". Local energy flux can then be computed by knowing the number of these bundles arriving per unit area and time at some position. Since Monte Carlo methods are statistical methods, the results, when plotted against number of samples, will generally fluctuate randomly around the correct answer. If a set of truly random numbers used for the sampling, then these fluctuations will decrease as the number of samples increases. For each emitted bundle, we need to determine a point of emission, a direction of emission, and track the photon bundles until they hit the wall or get absorbed within the gas media. Upon impact of the bundle onto the enclosure wall, we need to decide whether the bundle reflected and, if so, into what direction.

6.2.1.1 Surface to Surface Direct Exchange Area

Point of emission: The walls of a parallelepiped are oriented along the coordinate planes. The general expression for point of emission requires three uniformly distributed random number. The x-coordinates of the point of emission selected as: $x = x_{\min} + R_{\mathrm{x}}(x_{\max} - x_{\min})$, and similarly for y and z-coordinate. For the non-rectangular and non-square (polygon) cell faces, considered a plane of emission normal to the z-axis. For the calculation of point of emission on the polygon, first created a rectangular box with the same maximum and a minimum value in x and y of the polygon box as shown in Figure 6.3(a). To check whether the point lies inside or outside the polygon, a line drawn by considering the selected point as an initial point and by taking increment in coordinate value. If the total number of intersection between the

line drawn and all the sides of the polygon is even in number then the selected point, lies outside of polygon face otherwise lie inside the polygon.

Selection of point of emission for the inclined plane: When the plane is inclined with the coordinate axis, then selection of the point of emission on the surface becomes complicated, as the selected point should be uniformly distributed over the plane. In this work, first a projected plane is determined as shown in Figure 6.3(b). The uniformly distributed points of emission are selected on the projected plane. Finally, the selected points are projected back again on the original inclined plane.

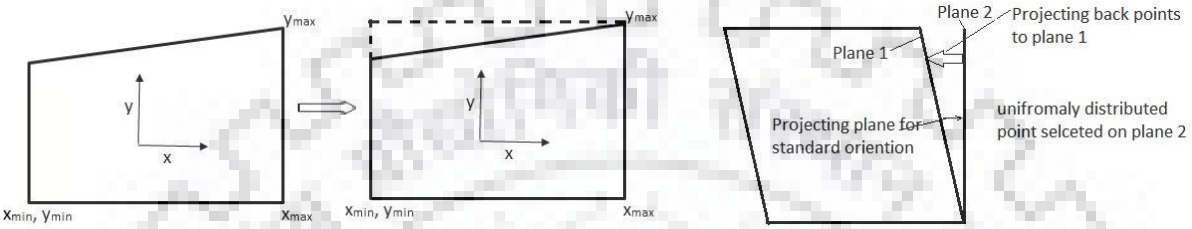

Figure 6.3 Selection of point of emission on a. Arbitrary face (left) b. Inclined plane (right)

Direction of emission: The direction of emission of an energy bundle into 3-D space depends on azimuthal angle, ψ, and the polar angle, ϑ, as shown in Figure 6.4.

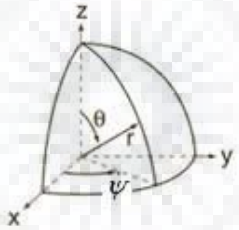

Figure 6.4 Direct of emission of a photon

Most real surfaces tend to be isotropic so that directional emittance does not depend on the azimuthal angle, ψ, and the choice of polar angle becomes independent of the azimuthal angle. Surfaces also tend to be a diffuse emitter. For such surfaces, the direction of emission can be deduced with two random numbers uniformly distributed as:

$$\psi = 2\pi R_{\psi}; \quad \theta = \sin^{-1}\sqrt{R_{\theta}} \tag{6.20}$$

Thus, the following vector can represent the direction of emission:

$$\bar{n} = \begin{bmatrix} n_x \\ n_y \\ n_z \end{bmatrix} = \begin{bmatrix} \cos\psi \sin\theta \\ \sin\psi \sin\theta \\ \cos\theta \end{bmatrix} \tag{6.21}$$

Emission from arbitrary plane: The Eq. 6.20(A1) and 6.21 (A2) will give the direction of emission of photon bundles from a plane parallel to the XY-plane, and vertical normal pointing in the -z direction. If the surface of emission is not aligned with the XY-plane, then the direction of emission needs to be rotated as well.

The direction of emission from the six faces of a cubical zone can be obtained with the following transformations in terms of face number and its normal axis direction.

$$\begin{aligned}
&\text{Face 1, +y} && \bar{d} = \begin{bmatrix} d_x \\ d_y \\ d_z \end{bmatrix} = \begin{bmatrix} n_y \\ -n_z \\ -n_x \end{bmatrix} && \text{Face 2, +x} && \bar{d} = \begin{bmatrix} d_x \\ d_y \\ d_z \end{bmatrix} = \begin{bmatrix} -n_z \\ -n_y \\ -n_x \end{bmatrix} \\
&\text{Face 3, -y} && \bar{d} = \begin{bmatrix} d_x \\ d_y \\ d_z \end{bmatrix} = \begin{bmatrix} -n_y \\ n_z \\ -n_x \end{bmatrix} && \text{Face 4, -x} && \bar{d} = \begin{bmatrix} d_x \\ d_y \\ d_z \end{bmatrix} = \begin{bmatrix} n_z \\ n_y \\ -n_x \end{bmatrix} \\
&\text{Face 5, +z} && \bar{d} = \begin{bmatrix} d_x \\ d_y \\ d_z \end{bmatrix} = \begin{bmatrix} n_x \\ n_y \\ -n_z \end{bmatrix} && \text{Face 6, -z} && \bar{d} = \begin{bmatrix} d_x \\ d_y \\ d_z \end{bmatrix} = \begin{bmatrix} n_x \\ n_y \\ n_z \end{bmatrix}
\end{aligned} \qquad 6.22$$

6.3 Spectral Models

6.3.1 Full-Spectrum k-distribution Method

The absorption coefficient *k* oscillates rapidly across the spectrum, attaining the same value many times (at different wavelengths). The *k*-distribution approach is a class of methods where the erratically-varying spectral absorption coefficients are reordered into monotonically increasing functions. These monotonic functions allow efficient integration of radiative intensity over the spectrum, thereby reducing the number of RTEs to be solved.

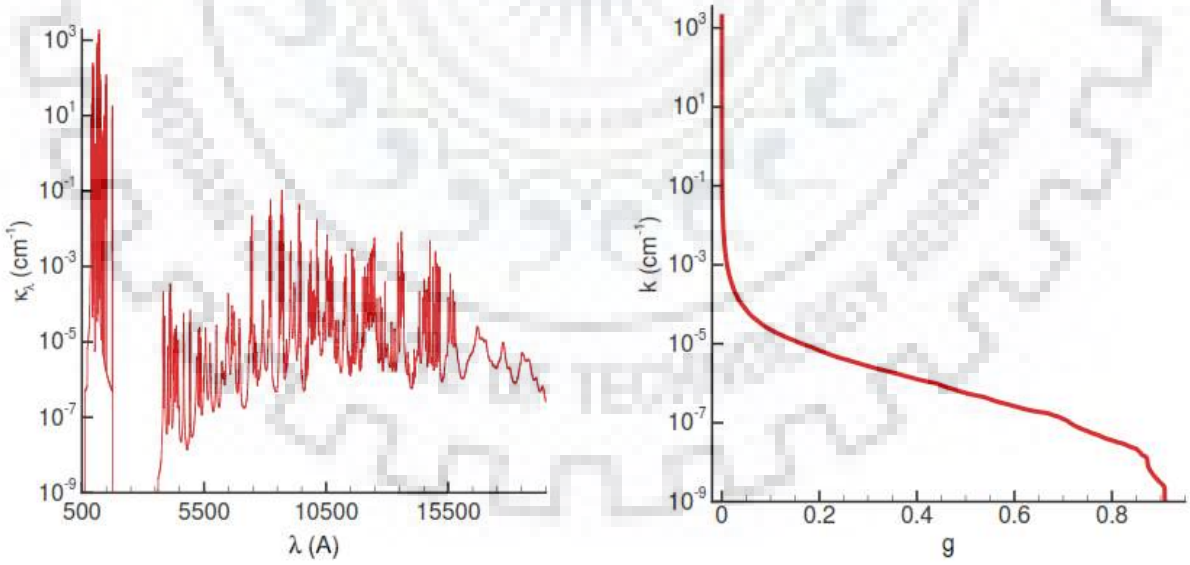

Figure 6.5 Absorption spectrum (left) and transformed Full-spectrum k-distribution (right)

6.3.2 Exchange Areas for non-grey medium

In the foregoing discussion, it was assumed that the medium and the surfaces are grey, although all equations are equally valid, on a spectral basis, for a non-grey enclosure with a non-grey medium.

Surface-to-Surface Energy Exchange: The direct energy transfer from one surface zone to other within an inhomogeneous absorbing medium can be defined as

$$Q_\lambda = \epsilon_i I_{b\lambda}(T_{si}) \int_{A_i} \int_{A_j} e^{-\kappa_\lambda S} \frac{\cos\theta_i \cos\theta_j}{\pi S^2} dA_j dA_i \qquad 6.23$$

$$Q_\lambda = \epsilon_i I_{b\lambda}(T_{si}) \left[\overline{s_i s_j}\right]_\lambda \qquad 6.24$$

where T_{si} is the temperature of surface zone *i* and $I_{b\lambda}$ is the Planck blackbody function. Now, multiplying the above equation by the Dirac delta function, $\delta\big(k - \kappa_\lambda(\varphi_0)\big)$ and integrating over the entire spectrum we get

$$\int_0^\infty Q_\lambda \delta(k-\kappa_\lambda) d\lambda = \epsilon_i \int_0^\infty \pi I_{b\lambda}(T_{si}) \delta(k-\kappa_\lambda) \int_{A_i} \int_{A_j} e^{-\kappa_\lambda S} \frac{\cos\theta_i \cos\theta_j}{\pi S^2} dA_j dA_i \, d\lambda \qquad 6.25$$

$$Q_k = \epsilon_i \pi I_b(T_{si}) f(k, T_{si}, \varphi_0) \int_{A_i} \int_{A_j} e^{-k^*(\varphi) S} \frac{\cos\theta_i \cos\theta_j}{\pi S^2} dA_j dA_i \qquad 6.26$$

provided that at every wavelength across the entire spectrum, where $\kappa_\lambda(\varphi_0) = k$, we also have a unique value of $\kappa_\lambda(\varphi) = k^*$ everywhere within the medium. Note that the absorption coefficient in the Dirac-delta function is evaluate at a reference state, φ_0 while the absorption coefficient in the attenuation term $e^{-\kappa_\lambda S}$ is evaluated at local state, φ. The reordered heat exchange term is given as

$$Q_k = I_b\big(T_{gi}\big) f\big(k, T_{gi}, \varphi_0\big) \int_{V_i} \int_{A_j} e^{-k^*(\varphi) S} \frac{\cos\theta_j}{\pi S^2} k^*(\varphi_i) dA_j dV_i \qquad 6.27$$

and the Plank-function-weighted full-spectrum *k*-distribution is given by

$$\boldsymbol{f(k, T_{si}, \varphi_0) = \frac{1}{I_b(T_{si})} \int_0^\infty I_{b\lambda}(T_{si}) \delta\big(k - \kappa_\lambda(\varphi_0)\big) d\lambda} \qquad 6.28$$

The full-spectrum *k*-distribution in Eq. 6.28 is a function of local surface temperature T_{si} through the blackbody function $I_b(T_{si})$, and of the reference gas state through the absorption coefficient, $\kappa_\lambda(\varphi_0)$, The *k*-distribution, can be considered a probability density function (PDF), giving the probability that the absorption coefficient will attain a value *k*.

It is clear from the above analysis, that we have transformed the spectral dependence of the problem from λ-space to *k*-space (the probability density function space). However, it is even more convenient, to transform the *k*-distribution (PDF) into a much smoother *g*-space (cumulative probability density

function). Now, dividing the Eq. 6.28 by $f(k, T_0, \varphi_0)$, i.e., full-spectrum *k*-distribution at reference absorption coefficient spectrum and at reference Planck function temperature we get

$$Q_g = \epsilon_i \pi I_b(T_{si}) a(T_0, T_{si}, \varphi_0)_g \int_{A_i} \int_{A_j} e^{-k^*(\varphi) S} \frac{\cos\theta_i \cos\theta_j}{\pi S^2} dA_j dA_i \qquad 6.29$$

where $a(T_0, T_{si}, \varphi_0)_g$ is the weight function, quite. similar to (but much more accurate) weights of WSGG model. The point to note here is that in comparison to weights in the WSGG model, the weights of the FSSK model are much more accurate. The cumulative full spectrum *k*-distribution is given by

$$g(k, T_0, \varphi_0) = \int_0^k f(k, T_0, \varphi_0)\, dk \qquad 6.30$$

where the value of g varies from 0 to 1. The smoothly varying one such *k*-distribution is given in Figure 6.5. Since the cumulative *k*-distribution has a very smooth distribution, a very efficient Gaussian quadrature scheme can be used for integration in the *g*-space. Eq. 6.29 can be written as

$$Q_g = \left[\overline{S_i S_j}\right]_g a(T_0, T_{si}, \varphi_0)_g \, E_{si} \qquad 6.31$$

with

$$E_{si} = \pi I_b(T_{si}) \qquad 6.32$$

and

$$\left[\overline{S_i S_j}\right]_g = \epsilon_i \int_{A_i} \int_{A_j} e^{-k^*(\varphi) S} \frac{\cos\theta_i \cos\theta_j}{\pi S^2} dA_j dA_i \qquad 6.33$$

Thus, the radiative energy transfer from surface *i* to surface *j* can be calculated just be weighting the emissive power by the *a*-function, and evaluating $k^*(\varphi, g)$ using the scaling function. The total spectrally integrated energy transfer is calculated by integrating the spectral heat transfer rate over the *g*-space as:

$$Q = \int_0^1 Q_g \, dg \qquad 6.34$$

Where *Q* is now the spectrally integrated heat exchange rate. The integral in the *g*-space is carried out using an appropriate quadrature scheme, such as Gauss-Legndre, Gauss Chebychev and Gauss-Lobatto, utilizing at most 8 quadrature points. We will employ a 8-point Gaussian quadrature scheme to evaluate the integral in Eq. 6.34 in this work.

The *k*-distribution method is exact for a homogeneous medium (reaching accuracy of the line-by-line method). For inhomogeneous path, assumption of scaling approximation has to be made. In the scaling function, it is assumed that the wavelength and local gas state dependence of absorption coefficient can be separated as

$$\mathrm{k}^*(\varphi) = k(\varphi_0)u(\varphi, \varphi_0) \tag{6.35}$$

where φ_0 is some reference gas state and $u(\varphi, \varphi_0)$ is the scaling function, to be evaluated later.

Volume-to-Surface Energy Exchange: Similarly, energy transfer directly from a volume zone to a surface zone is written as

$$Q_\lambda = \int_{V_i}\int_{A_j} e^{-\kappa_\lambda S}\frac{\cos\theta_j}{\pi S^2}\kappa_\lambda(\varphi_i)I_{b\lambda}(T_{gi})dA_j dV_i \tag{6.36}$$

Now, multiplying the above equation by the Dirac delta function, $\delta\big(k-\kappa_\lambda(\varphi_0)\big)$ and integrating over the entire spectrum we get

$$\int_0^\infty Q_\lambda\delta(k-\kappa_\lambda)d\lambda = \int_0^\infty \int_{V_i}\int_{A_j} e^{-\kappa_\lambda S}\frac{\cos\theta_j}{\pi S^2}\kappa_\lambda(\varphi_i)I_{b\lambda}(T_{gi})dA_j dV_i\delta(k-\kappa_\lambda)d\lambda \tag{6.37}$$

$$Q_k = I_b(T_{gi})f\big(k, T_{gi}, \varphi_0\big)\int_{V_i}\int_{A_j} e^{-k^*(\varphi)S}\frac{\cos\theta_j}{\pi S^2}k^*(\varphi_i)dA_j dV_i \tag{6.38}$$

where the Planck function weighted *k*-distribution is now given as

$$f\big(k, T_{gi}, \varphi_0\big) = \frac{1}{I_b(T_{gi})}\int_0^\infty I_{b\lambda}(T_{gi})\delta\big(k-\kappa_\lambda(\varphi_0)\big)d\lambda \tag{6.39}$$

Dividing Eq. 6.38 by $f(k, T_0, \varphi_0)$, we get

$$Q_g = I_b(T_{gi})a\big(T_0, T_{gi}, \varphi_0\big)_g\int_{V_i}\int_{A_j} e^{-k^*(\varphi)S}\frac{\cos\theta_j}{\pi S^2}k^*(\varphi_i)dA_j dV_i \tag{6.40}$$

$$Q_g = I_b(T_{gi})a\big(T_0, T_{gi}, \varphi_0\big)_g\big[\overline{g_i s_j}\big]_g \tag{6.41}$$

Volume-to-Volume Energy Exchange: Finally, the direct energy exchange between two volume zones can similarly be written as

$$Q_g = I_b(T_{gi})a\big(T_0, T_{gi}, \varphi_0\big)_g\int_{V_i}\int_{V_j} e^{-k^*(\varphi)S}\frac{k^*(\varphi_i)k^*\big(\varphi_j\big)}{\pi S^2}dV_j dV_i \tag{6.42}$$

$$Q_g = I_b(T_{gi})a\big(T_0, T_{gi}, \varphi_0\big)_g\big[\overline{g_i g_j}\big]_g \tag{6.43}$$

6.3.3 Correlations for k-Distributions

Denison and Webb have calculated large numbers of *k*-distributions for water vapour and carbon dioxide, using the HITRAN92 database [164,166]. The resulting cumulative *k*-distributions were then presented in the form of relatively straightforward correlations for engineering use. Recently, Modest *et al.* [162,177,178] have provided a new set of correlation constant for CO_2 and H_2O, based on the HITEMP and CDSD-1000 database. These correlations allow efficient and quick evaluation of cumulative *k*-distributions for different gas and Planck function temperatures at atmospheric pressure and unity mole fraction. To evaluate *k*-distributions for a mixture of gases require mixing of the *k* -distributions.

Correlations for CO_2: Following Modest *et al.* the correlation for the cumulative *k*-distribution for CO_2 can be written as

$$g(T_p, T_g, x = 0; k) = \frac{1}{2}\tanh\left[P(T_p, T_g, x = 0; k)\right] + \frac{1}{2} \qquad 6.44$$

where T_P stands for the Planck function temperature and T_g stands for the gas temperature. Since the correlation is for single gas at atmospheric pressure, the concentration of the gas does not enter into the equation. P in the above equation is given by

$$P(T_p, T_g, x = 0; k) = \sum_{l=0}^{3}\sum_{m=0}^{3}\sum_{n=0}^{3} a_{lmn}\left[\frac{T_g}{T_{ref}}\right]^n \left[\frac{T_P}{T_{ref}}\right]^m \left[\log_{10}\left(\frac{k}{k_{ref}}\right)\right]^l \qquad 6.45$$

where T_{ref}=1000 K, k_{ref} = 1 $cm^{-1}bar^{-1}$ are reference values for temperature and pressure- based absorption coefficient, and a_{lmn} are parameters found from the least-mean-square-error fit. The value of these parameters is given in Table 1. The above equation is valid for air broadening only, where mole fraction of H_2O is negligible. Since CO_2 does not show strong self-broadening effects, the correlation is essentially independent of the CO_2 mole-fraction, which has thus been neglected.

Correlations for H_2O: Expression given in Eq. 6.44 and Eq. 6.45 can also be employed for water vapour with a different set of coefficients, given in Table 2. However, water vapour is a strong self-broadener, and thus above equation needs to be modified to account for the different broadening in the presence of substantial amount of water vapour. Here, we will use a approach suggested by Modest *et al.* for finding the *k*-distribution of water vapour under strong self-broadening mechanism. For a fixed value of the cumulative *k*-distribution, ***g*** (and thus for a fixed *P*), the absorption coefficient *k* (with broadening) and k_0 (without broadening) are related with the following correlation:

$$\log_{10}\left(\frac{k_0}{k_{ref}}\right) = \log_{10}\left(\frac{k}{k_{ref}}\right) + \sum_{l=0}^{2}\sum_{m=0}^{2}\sum_{n=0}^{1} b_{lmn}\left[\log_{10}\left(\frac{k}{k_{ref}}\right)\right]^n \left[\frac{T_g}{T_{ref}}\right]^l [x]^{m+1} \qquad 6.46$$

6.3.4 *k-Distributions for mixture of gases*

Often in the combustion product a number of gases would be simultaneously present, which may absorb in different spectral ranges. The spectral absorption coefficients of these gases may overlap or may not have significant overlap. Since the correlations described in the previous section are for single species only. There should be some mechanism to combine these *k* -distribution into one for a given gas mixture. It is highly desirable to quickly construct *k*-distribution for arbitrary gas mixtures from individual gas *k*-distribution. Mixture distributions from those for individual species has proven problematical [179]. A number of approximate mixing schemes have been discussed by Webb *et al*. [170,172]. The two schemes that have effectively been used are: superposition and random-overlap models.

Scaling *k* -distribution for non-unity mole fraction: Considering a gas whose absorption coefficient is linearly dependent on its partial pressure, i.e., a gas whose line broadening is unaffected by its own partial pressure.

$$\kappa_\lambda(T_g, x) = \; x\, \kappa_\lambda(T_g) \tag{6.47}$$

where *x* is the mole fraction of the gas in a mixture. According to Modest., the *k* vs. *g* behaviour is independent of mole fraction. The *k*-*g* plot is simply vertically displaced by a factor of *x*.

$$g(T_p, T_g, ; k) = g(T_p, T_g, x; k_x) \tag{6.48}$$

where $k_x = xk$.

Superposition Method: Here we consider a mixture of *M* different absorbing gases, whose absorption coefficients do not overlap each other anywhere across the entire spectrum. Under such conditions the *k*-distributions of the individual species are unaffected by the others.

$$g_{mix}(\varphi, k) = (1 - M) + \sum_{m=1}^{M} g_m(\varphi, k) \tag{6.49}$$

Multiplication Method: Based on the observation by Taine and Soufiani [180], that very accurate values of transmissivities of gas mixtures can be obtained by multiplying transmissivities of individual gas species. If one treats the absorption coefficients of the *M* species as statistically independent random variables, the *k*-distributions are said to be statistically uncorrelated. When considering the entire spectrum, the cumulative *k*-distributions are multiplicative [170]

$$g_{mix}(\varphi, k) = \prod_{m=1}^{M} g_m(\varphi, k) \tag{6.50}$$

In general, the multiplication method yields more accurate results than the superposition method. Both the models described above predict the correct distribution very well for large values of *k*. For very small values of *k* substantial overlap between species is to be expected, and the superposition method fails. The product method, on the other hand, appears to give good accuracy for nearly all conditions. Furthermore, adding non-grey particle absorption backgrounds (such as soot) to FSK distributions is not possible.

6.3.5 *Weighted-Sum-of-Gray Gases*

The weighted-sum-of-gray-gases model implemented in this work is based on the work of [149]. This model assumes three gray gases and one clear gas. The absorption coefficients are assumed to be constant, and do not depend on temperature; however, the weights for emissivity and absorptivity are allowed to depend on wall and gas temperatures. These weights are evaluated from curve fit parameters proposed by Smith *et al.* [162]. The disadvantage of WSGG parameters is that they are given for fixed ratio of gas concentration.

The total emissivity for the WSGG model is evaluated from the following expression:

$$\varepsilon = \sum_{i=0}^{I=3} a_{\varepsilon i}(T_g)[1 - e^{-k_i ps}] \qquad 6.51$$

where a represents the emissivity weighting factor for the i-th gray gas, k_i represents the absorption coefficient, p is the sum of partial pressures of absorbing gases and s is the path length. The model used in the work assumes three gray gases and one clear gas, having absorption coefficient equal to zero. The weighting factors, just like in the case of k-distribution model, represent the fraction of black body energy in the spectrum represented by the gray gas. The above coefficient are allowed to depend on gas temperature as

$$a_{\varepsilon i}(T_g) = \sum_{j=1}^{J=4} b_{i,j} T_g^{j-1} \qquad \text{i=1→3} \quad 6.52$$

$$a_{\varepsilon 0}(T_g) = 1 - \sum_{i=1}^{I=3} a_{\varepsilon i}(T_g) \qquad 6.53$$

The coefficient $b_{i,j}$ used are given in Appendix. Similarly, for the emission from the wall, the absorptivity is defined is as

$$\alpha = \sum_{i=0}^{I=3} a_{\alpha i}(T_g, T_s)[1 - e^{-k_i ps}] \qquad 6.54$$

where the coefficient $a_{\alpha i}$ are function of surface as well as gas temperature are defined as

$$a_{\alpha i}(T_g, T_s) = \sum_{j=1}^{J=4}\left[\sum_{k=1}^{K=4} c_{i,j,k} T_s^{k-1}\right] T_g^{j-1} \qquad \text{i=1→3} \quad 6.55$$

$$a_{\alpha 0}(T_g, T_s) = 1 - \sum_{i=1}^{I=3} a_{\alpha i}(T_g, T_s) \qquad 6.56$$

6.3.6 *Treatment of Particles*

In combustion chambers, soot, pulverized coal, char, and fly-ash are the particulates to be considered. Nearly all flames are visible to the human eye and are, therefore, called luminous (sending out light). There is some radiative emission from within the flame at wavelengths where no molecular band radiates. This luminous emission is known to come from tiny char (almost pure carbon) particles, called soot, which are generated during the combustion process. In the presence of particles, the spectral properties of the combustion gases may be suppressed.

The higher the soot content, the more luminous the radiation is. Soot particles are produced in fuel-rich flames, or fuel-rich parts of flames, as a result of incomplete combustion of hydrocarbon fuels. Soot particles are generally small and spherical, ranging in size between approximately 50 $\dot{A}$ and 800 $\dot{A}$ [149]. Soot is one of the most important contributors to radiation heat transfer in practical systems. Mainly because it's small size, scattering of radiation by soot is negligible in comparison to absorption. Since soot particles are very small, they are generally at the same temperature as the flame and, therefore, strongly emit thermal radiation in a continuous spectrum over the infrared region. Experiments have shown that soot emission often is considerably stronger than the emission from the combustion gases. In order to predict the radiative properties of a soot cloud, it is necessary to determine the amount, shape and distribution of soot particles, as well as their optical properties, which depend on chemical composition and particle porosity. Of course, this analysis is extremely complicated and requires extensive computational resource.

Soot radiation has mostly been treated using the optically-thin approximation with the assumption of grey soot. Non-grey soot has been investigated by Solovjov and Webb [181] using the SLW method and by Wang *et al.* [182], who employed the single-scale FSK method [182]. Solovjov and Webb treated non-grey soot as an additional non-grey gas species and the multi-component gas mixture with soot was treated as a single gas within the SLW method [181]. In the full-spectrum format, soot must be treated as grey and its spectrally averaged mean property (a constant) can then be added directly to full-spectrum *k*-distributions of the gas mixture. However, it must be emphasised that the non-grey soot radiation is very important, even more important than the non-grey gas radiation. The non-grey treatment of soot strongly influences flame temperatures and is essential for accurate predictions of NO_x formation in sooty flames. In this work, the Planck mean absorption coefficient would be used for modelling absorption from soot particles. This can be calculated as [149]

$$\kappa_P = 3.83 f_v C_o T / C_2 \qquad 6.57$$

where C_2 =1.4388 cm K is the second Planck function constant and C_0 is parameter that depends only on soot complex index of refrection (m-*in*) as

$$C_0 = \frac{36\pi mn}{(m^2 - n^2 + 2)^2 + 4m^2n^2} \qquad 6.58$$

Further, the contribution of fly-ash particles to radiation heat transfer in pulverized-coal flames could be significant and, therefore, attention must be given to the radiative properties of these particles. However, in the absence of reliable radiative properties of fly-ash particles, these particles are not treated in the present model.

Properties of ash: Fly Ash and pulverised coal particles are likely to strongly scatter radiation inside the furnace. The Planck mean properties of these particles are represented through correlations as given below [149]:

$$\frac{1}{\kappa_P^z} = \frac{1}{\left(0.0032\emptyset\left[1 + \left({}^{\emptyset}/_{725}\right)^{1.65}\right]\right)^z} + \frac{1}{\left({}^{13.75}/_{\emptyset^{0.13}}\right)^z} \qquad 6.59$$

$$\frac{1}{\beta_P^z} = \frac{1}{\left(0.0032\emptyset\left[1 + \left({}^{\emptyset}/_{355}\right)^{1.9}\right]\right)^z} + \frac{1}{\left({}^{10.99}/_{\emptyset^{0.02}}\right)^z} \qquad 6.60$$

where

$$\emptyset = \frac{\int_0^\infty r^3 n(r)dr}{\int_0^\infty r^2 n(r)dr} T \qquad 6.61$$

6.4 The Method of Spherical Harmonics (P_l – approximation)

Chapter 7
UNCOUPLED DSMC/RADIATION MODEL

In this section, results are presented for radiative heat fluxes and radiative heat source terms inside the furnace. Two different cases are considered. In the first case, the gas temperature and concentration are kept realistic to actual conditions and *k*-distribution model is applied to calculate the absorption coefficient of the gas. The accuracy and efficiency of the Imaginary plane method and the zonal method are compared. The wall heat flux is plotted along the front wall, starting from the bottom most zone and going towards the top zone. The radiative source term represents the values inside one of the four zones in a vertical layer. Due to symmetry, the values, inside all the zones in a layer will be same.

3.1 Effect of cell discretization on heat flux

In this case, a single cubical cell of side 0.1 m with homogeneous gas and surface properties is considered. The cubical cell is assumed to contain a hypothetical grey gas at temperature 1500 K. The grey gas absorption coefficient *k* is varied from 0.001 to 1 m^{-1}. Through the case the accuracy of the IPM solver is validated against the analytical results. Zero gradient boundary conditions are applied to side walls of the cube, while top and bottom walls are assumed to be cold and black. This case represents plane parallel slab for which analytical solution is available and is given as:

$$Q = \left(1 - 2E_3(kL)\right) \times \sigma(T_g^4 - T_w^4) \qquad (1)$$

Where $E_3(kL)$ is the exponential integral of order three [149]. The heat flux, Q (W/m^2) is compared in Table 7.1.

Table 7.1 ***Heat flux value calculated using IPM method***

k (m^{-1})	Q_{IPM} (W/m^2)	$Q_{Analytical}$ (W/m^2)	Error %	$Q_{P1\text{-}Analytical}$ (W/m^2)	Error %
1	49,540.75	48,059.68	3.081	52,073.42	8.3515
0.1	5640.62	5,582.24	1.046	5683.86	1.8204
0.01	570.83	571.83	0.174	573.55	0.3007
0.001	57.32	57.412	0.160	57.38	0.0557

The results show that the IPM model for this simplest case is agreeing well with the analytical results. This partly validates our solver. For the same case, the analytical results for the P_1 method are also given in Table 1. The analytical result for the non-dimensional heat flux obtained with the P_1 method is given as [149]:

$$\psi = \frac{Q_{Analytical(P1)}}{\sigma(T_g^4 - T_w^4)} = \frac{2\sinh\gamma\tau}{\sinh\frac{1}{2}\gamma\tau_L + \frac{1}{2}\sqrt{\frac{3 - A_{1\omega}}{1-\omega}}\cosh\frac{1}{2}\gamma\tau_L} \qquad (2)$$

where the value of single scattering albedo (ω) is taken as zero and γ is calculated as $\gamma = \sqrt{(1-\omega)(3 - A_1\omega)} = \sqrt{3}$.

Next, we study the effect of domain discretization on the accuracy of the IPM method as wells as on the numerical P_1 method. Both the studies are done in OpenFOAM. We consider three cases with number of cells in each direction taken as two, five and ten. The partial differential equation for the P_1 method is discretized with the central differencing scheme. Marshak boundary condition is applied to the top and bottom walls, while the side walls are set with the zero gradient boundary condition. Results for the two methods are compared in **Error! Reference source not found.**.

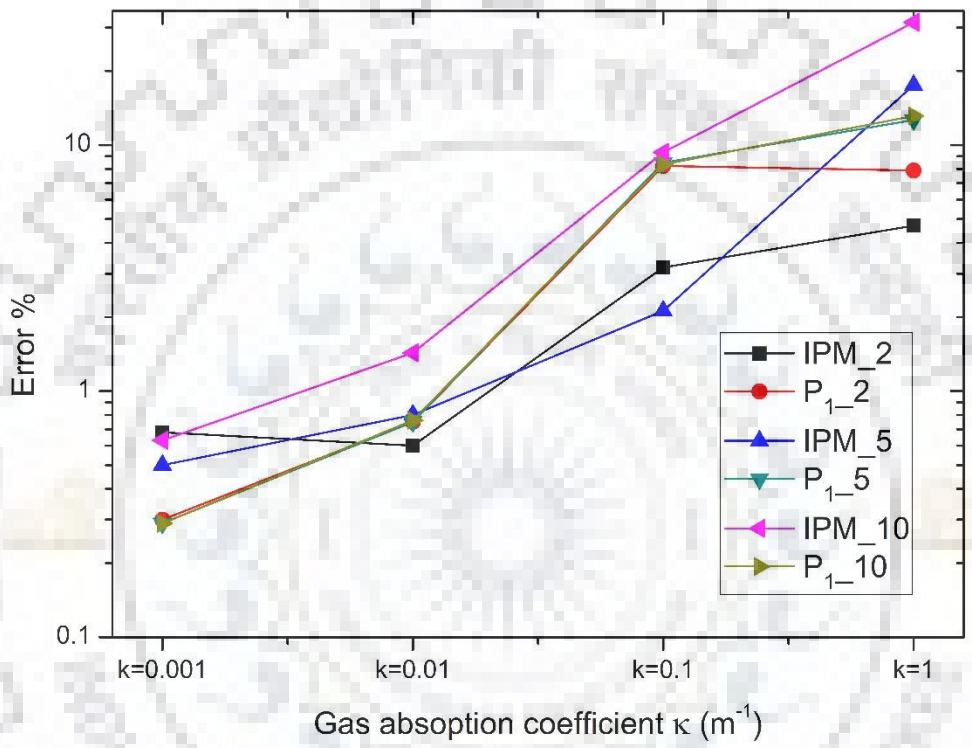

Figure 7.1 Error in the calculation of heat flux with the gas absorption coefficient and discretization

The value of gas absorption coefficient is varied from 0.001 to 1 m^{-1}. Figure 7.1 shows the percentage error in the evaluation of radiative heat flux. Since this case represents the plane parallel slab problem, the reference for comparison are again taken as the analytical results. Since the flux on the top wall in the numerical results would vary from cell to cell, we have taken average over the cells for comparison. For optically thin case, both the methods perform equally well with error of around 1%. However, the error incurred in numerical evaluation increases with optical thickness for both the methods. For coarse discretization, the IPM method performs slightly better than the P_1 method. On the other hand, at finer discretization, the IPM method incurs higher error.

3.2 Application on concentric cylinder:

The P_1 and IPM model is applied on concentric cylinder, where the outer cylinder temperature is 2 K and inner cylinder kept at 1500 K temperature shown in **Error! Reference source not found.**. The outer cylinder radius is 1 m, inner cylinder radius is 0.5 m, and the length of the cylinder in the z direction is taken as 1 m. The space between the cylinders is filled with gray gas at equilibrium temperature 1203 K temperature calculated at 0.25 m distance from the inner cylinder from the equation given as:

$$\frac{T^4 - T_1^4}{T_2^4 - T_1^4} = \frac{\ln(\tau/\tau_1)}{\ln(\tau_2/\tau_1)} \qquad (61)$$

The gas absorptivity constant is varied from 0.001 m^{-1} to 1 m^{-1} and, heat flux on the surface of inner cylinder calculated. For the IPM method the mesh is simplified as the error in the IPM method occurs when the number of cell discretization increases. The heat flux on the surface are averaged and, shown result in Table 2. The comparison of non-dimensional heat flux for the P_1 and exact method is given in the book by Modest [149], which shows the high error in heat flux by P_1 method when the gas absorption coefficient is very low.

κ (m^{-1})	Q_{IPM} (W/m^2)	$Q_{P1\text{-}Analytical}$ (W/m^2)	E_{xact} (W/m^2)	*Error in IPM*	*Error in P_1*
1	205686	284,722.6	243,297.6	15.45	17.02
0.5	220187	326,774.3	264,843.8	16.86	23.38
0.1	236970	370,557.5	282,080.7	16.00	31.36
0.01	241694	382,075.8	285,959.1	15.47	33.61
0.001	242191	383,267.2	286,346.9	15.42	33.84

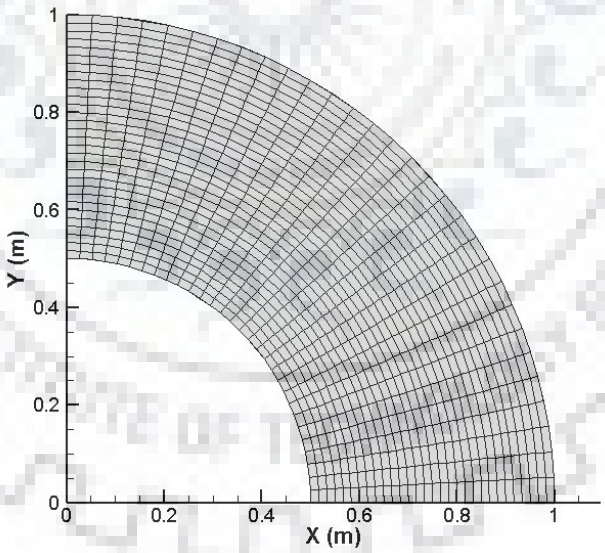

Figure 7.2 Mesh of concentric cylinder for P1 model

Chapter 8
SUMMARY AND CONCLUSIONS

8.1 Summary

8.2 Future Work

Appendix A

Appendix B

References

[1] Longo, J. M. a., Hannemann, K., and Hannemann, V., 2007, "The Challenge of Modeling High Speed Flows," Proc. EUROSIM 2007.

[2] Cercignani, C., Crighton, D. G., and Ablowitz, M. J., 2000, *Rarefied Gas Dynamics: From Basic Concepts to Actual Calculations*, Cambridge University Press.

[3] Rapaport, D. C., 2004, *The Art of Molecular Dynamics Simulation*, Cambridge University Press, Cambridge.

[4] Frenkel, D., and Smit, B., 2002, *Understanding Molecular Simulation*, Academic Press, San Diego.

[5] Jr, J. D. A., 1969, "An Engineering Survey of Radiating Shock Layers," AIAA J., **7**(9), pp. 1665–1675.

[6] Park, C., 2004, "Stagnation-Point Radiation for Apollo 4," J. Thermophys. Heat Transf., **18**(3), pp. 349–357.

[7] Olynick, D. R., Henline, W. D., Chambers, L. H., and Candler, G. V., 1995, "Comparison of Coupled Radiative Flow Solutions with Project Fire II Flight Data," J. Thermophys. Heat Transf., **9**(4), pp. 586–594.

[8] Sutton, K., 1974, *Heating Analysis for the Pioneer Venus Multiprobe Mission*.

[9] Florence, D. E., 1981, "Aerothermodynamic Design Feasibility of a Mars Aero- Capture / Aeromaneuver Vehicle," AIAA 19th Aerosp. Sci. Meet., p. 16.

[10] Park, C., Howe, J. T., Jaffe, R. L., and Candler, G. V, 1994, "Review of Chemical-Kinetic Problems of Future NASA Missions, II: Mars Entries," J. Thermophys. Heat Transf., **8**(1), pp. 9–23.

[11] Kudryavtsev, N. N., Kuznetsova, L. A., and Anaheim, J., 2001, "Kinetics and Nonequilibrium Radiation of CO2 -N2 Shock Waves," 32nd AIAA Plasmadynamics Laser Conf., (2728), pp. 1–11.

[12] Tauber, M. E., and Wakefield, R. M., 1971, "Heating Environment and Protection during Jupiter Entry," J. Spacecr. Rockets, **8**(6), pp. 630–636.

[13] Matsuyama, S., Shimogonya, Y., Ohnishi, N., Sawada, K., and Sasoh, A., 2002, "Numerical Simulation of Galileo Probe Entry Flowfield with Radiation," 8th AIAA/ASME Jt. Thermophys. Heat Transf. Conf., **19**(1).

[14] Tiwari, S. N., and Subramanian, S. V., 1981, *Influence of Nonequilibrium Radiation and Shape Change on Aerothermal Environment of a Jovian Entry Body*.

[15] Hollis, B. R., Wright, M. J., Olejniczak, J., Takashima, N., Sutton, K., and Prabhu, D., 2004, "Preliminary Convective-Radiative Heating Environments for a Neptune Aerocapture Mission," AIAA Atmos. Flight Mech. Conf. ans Exhib., **2**(August), pp. 1040–1051.

[16] Lockwood, M. K., Edquist, K. T., Starr, B. R., Hollis, B. R., Hrinda, G. A., Bailey, R. W., Hall, J. L., Spilker, T. R., Noca, M. A., Kongo, N. O., Haw, R. J., Justus, C. G., Duvall, A. L., Keller, V. W., Sutton, K., and Dyke, R. E., 2006, *Aerocapture Systems Analysis for a Titan Mission*.

[17] Olejniczak, J., Wright, M., Prabhu, D., Takashima, N., Hollis, B., Vincent Zoby, E., and Sutton, K., 2003, "An Analysis of the Radiative Heating Environment for Aerocapture at Titan," 39th AIAA/ASME/SAE/ASEE Jt. Propuls. Conf. Exhib., (July).

[18] Silva, M. L., and Beck, J., 2011, "Contribution of CO2 IR Radiation to Martian Entries Radiative Wall Fluxes," 49th AIAA Aerosp. Sci. Meet. Contrib. CO2 IR Radiat. to Martian, (January), pp. 1–15.

[19] Wright, M. J., Tang, C. Y., Edquist, K. T., Hollis, B. R., Krasa, P., and Campbell, C. H. A., 2010, "A Review of Aerothermal Modeling for Mars Entry Missions," 48th AIAA Aerosp. Sci. Meet. Incl. New Horizons Forum Aerosp. Expo., (January), pp. 1–39.

[20] Rouzaud, O., Tessé, L., Soubrié, T., Soufiani, A., Rivière, P., and Zeitoun, D., 2008, "Influence of Radiative Heating on a Martian Orbiter," J. Thermophys. Heat Transf., **22**(1), pp. 10–19.

[21] Wright, M. J., Bose, D., and Olejniczak, J., 2004, "The Impact of Flowfield-Radiation Coupling on Aeroheating for Titan Aerocapture," AIAA Pap., **19**(1), pp. 1109–1123.

[22] Baillion, M., Taquin, G., and Soler, J., 1995, "Huygens Radiative Probe Environment," *Proceedings*

Ofthe 19th International Symposiumon ShockWaves, Springer-Verlag, Berlin, pp. 339–346.

[23] Ozawa, T., Wang, A., Levin, D. A., and Modest, M., 2008, "Development of a Coupled DSMC - Particle Photon Monte Carlo Method for Simulating Atomic Radiation in Hypersonic Reentry Flows," 40th Thermophys. Conf., (June), pp. 23–26.

[24] Olynick, D., Chen, Y., Tauber, M. E., Chen, ¤ Y.-K, and Tauber, M. E., 1999, "Aerothermodynamics of the Stardust Sample Return Capsule," J. Spacecr. Rockets, **36**(3), pp. 12–15.

[25] Gupta, R. N., "Aerothermodynamic Analysis of Stardust Sample Return Capsule with Coupled Radiation and Ablation," J. Spacecr. Rockets, **37**(4).

[26] Park, C., 2005, "Calculation of Stagnation-Point Heating Rates Associated with Stardust Vehicle," *43rd AIAA Aerospace Science Meeting and Exhbit , Reno, Nevada*.

[27] Liu, Y., Ames, N., Field, M., Prabhu, D., Corp, E., Trumble, K., Ames, N., and Field, M., 2008, "Radiation Modeling for the Reentry of the Stardust Sample Return Capsule," *46th AIAA Aerospace Science Meeting and Exhibit, Reno, Nevada*, p. 2008.

[28] Bansal, A., Feldick, A., and Modest, M., 2012, "Simulation of Hypersonic Flow and Radiation over a Mars Reentry Vehicle Using OpenFOAM," 50th AIAA Aerosp. Sci. …, (January), pp. 1–18.

[29] Bose, D., McCorkle, E., Thompson, C., Bogdanoff, D., Prabhu, D., Allen, G., and Grinstead, J., 2008, "Analysis and Model Validation of Shock Layer Radiation in Air," 46th AIAA Aerosp. Sci. Meet. Exhib., (January), pp. 1–14.

[30] Bose, D., McCorkle, E., Bogdanoff, D., and Allen, G. A., 2009, "Comparisons of Air Radiation Model with Shock Tube Measurements," *47th AIAA Sciences Meeting Including the New Horizons Forum and Aerospace Exposition*, pp. 1–21.

[31] Osawa, H., Matsuyama, S., Ohnishi, N., and Sawada, K., 2006, "Comparative Computation of Radiative Heating Environment for Huygens Probe Entry Flight," Collect. Tech. Pap. - 9th AIAA/ASME Jt. Thermophys. Heat Transf. Conf. Proc., **4**(June), pp. 2299–2309.

[32] Pace, A. E., Ruffin, S. M., and Bose, D., 2009, "A Loosely-Coupled Approach for Shock-Layer Radiation Modeling in DPLR," 41st AIAA Thermophys. Conf., (June), pp. 1–10.

[33] Park, C., 1999, "Interaction of Spalled Particles with Shock Layer Flow," *37th AIAA Aerospace Science Meeting and Exhibit*, p. 12.

[34] Hoshizaki, H., and Lasher, L. E., 1969, "Convective and Radiaitive Heat Transfer to an Ablating Body," AIAA J., **6**(8), pp. 1441–1449.

[35] Coleman, W. D., and Hearne, F., 1968, "A Study of the Effect of Environemental and Ablator Performance Uncertainities on Heat Shielding Requirements for Blunt and Slender Hyperbolic-Entry Vehices," *6th AIAA Aerospace Science Meeting*, p. 25.

[36] Sutton, K., and Falanga, R. A., 1973, "Stagnation Region Radiative Heating with Steady-State Ablation during Venus Entry," J. Spacecr. Rockets, **10**(2), pp. 155–157.

[37] Moss, J. N., Zoby, E. V., and Sutton, K., 1977, "A Study of Aerothermal Environment for the Pioneer Venus Multiprobe Mission," *12th AIAA Thermophysical Conference*, p. 15.

[38] Moss, J. N., and Simmonds, A. L., 1982, "Galileo Probe Forebody Flowfield Predictions during Jupiter Enrty," *AIAA/ASME 3rd Joint Thermophysics, Fluids, Plasma and Heat Transfer Conference*, p. 23.

[39] Finkbeiner, J., Dunlap, P., Steinetz, B., and Daniels, C., 2012, "Apollo Seals: A Basis for the Crew Exploration Vehicle Seals," (July).

[40] Ozawa, T., Fedosov, D., Levin, D. A., and Gimelshein, S. F., 2005, "Quasi-Classical Trajectory Modeling of OH Production in Direct Simulation Monte Carlo," J. Thermophys. HEAT Transf., **19**(2), pp. 235–244.

[41] Gimelshein, N. E., Gimelshein, S. F., Levin, D. A., Ivanov, M. S., and Wysong, I. J., 2003, "Reconsideration of DSMC Models for Internal Energy Transfer and Chemical Reactions," *23rd International Symposium*, pp. 349–357.

[42] Xue, H., Fan, Q., and Shu, C., 2000, "Prediction of Micro-Channel Flows Using Direct Simulation Monte Carlo," Probabilistic Eng. Mech., **15**(2), pp. 213–219.

[43] Scanlon, T. J., White, C., Borg, M. K., Palharini, R. C., Farbau, E., Boyd, I. D., Reesetf, J. M., Browntt, R. E., Farbar, E., Boyd, I. D., Reese, J. M., and Brown, R. E., 2015, "Open-Source Direct Simulation Monte Carlo Chemistry Modeling for Hypersonic Flows," AIAA J., **53**(4), pp. 1670–1680.
[44] Boyd, I. D., 2007, "Modeling Backward Chemical Rate Processes in the Direct Simulation Monte Carlo Method," Cit. Phys. Fluids, **19**(12), p. 126103.
[45] Liechty, D. S., and Lewis, M. J., 2014, "Extension of the Quantum-Kinetic Model to Lunar and Mars Return Physics," Phys. Fluids, **26**(2), p. 27106.
[46] Bird, G. A., 1994, *Molecular Gas Dynamics and the Direct Simulation of Gas Flows*, Clarendon Press.
[47] Boyd, I. M. D. M., and Boyd, I. D., 1990, "Assessment of Chemical Nonequilibrium in Rarefied Hypersonic Flow," *28th Aerospace Science Meeting*, p. 12.
[48] G. Candler, 1990, "Computation of Thermo-Chemical Nonequilibrium Martian Atmospheric Entry Flows," *AIAA 90-1695 5th Joint Thermophysics and Heat Transfer Conference*, pp. 1–10.
[49] Fishburne, E. S., Bilwakesh, K. R., and Edse, R., 1967, *Chemical Kinetics of Entry into the Martian Atmosphere*.
[50] Gallis, M. A., Bond, R. B., and Torczynski, J. R., 2009, "A Kinetic-Theory Approach for Computing Chemical-Reaction Rates in Upper-Atmosphere Hypersonic Flows," J. Chem. Phys., **131**(12311), pp. 1–13.
[51] Gallis, M. A., Bond, R. B., and Torczynski, J. R., 2009, *Molecule-Based Approach for Computing Chemical-Reaction Rates in Upper Atmosphere Hypersonic Flows*.
[52] Bird, G. A., 2011, "Chemical Reactions in DSMC," *AIP Conference Proceedings*, pp. 1195–1202.
[53] Liechty, D. S., and Lewis, M. J., 2011, "Extension of a Kinetic-Theory Approach for Computing Chemical-Reaction Rates to Reactions with Charged Particles," AIP Conf. Proc., **1333**(1), pp. 1239–1244.
[54] Gimelshein, S. F., and Wysong, I. J., 2019, "Bird's Total Collision Energy Model: 4 Decades and Going Strong," Phys. Fluids, **31**(7).
[55] Palharini, R. C., White, C., Scanlon, T. J., Brown, R. E., Borg, M. K., and Reese, J. M., 2015, "Benchmark Numerical Simulations of Rarefied Non-Reacting Gas Flows Using an Open-Source DSMC Code," Comput. Fluids, **120**, pp. 140–157.
[56] Casseau, V., Espinoza, D. E. R., Scanlon, T. J., and Brown, R. E., 2016, "A Two-Temperature Open-Source CFD Model for Hypersonic Reacting Flows, Part Two: Multi-Dimensional Analysis," Aerospace, **3**(4).
[57] White, C., Borg, M. K., Scanlon, T. J., and Reese, J. M., 2013, "A DSMC Investigation of Gas Flows in Micro-Channels with Bends," Comput. Fluids, **71**, pp. 261–271.
[58] Scanlon, T. J., Roohi, E., White, C., Darbandi, M., and Reese, J. M., 2010, "An Open Source, Parallel DSMC Code for Rarefied Gas Flows in Arbitrary Geometries," Comput. Fluids, **39**(10), pp. 2078–2089.
[59] Dongari, N., White, C., Scanlon, T. J., Zhang, Y., and Reese, J. M., 2013, "Effects of Curvature on Rarefied Gas Flows between Rotating Concentric Cylinders," Phys. Fluids, **25**(5).
[60] Kumar, R., 2016, "Numerical Investigation of Gas-Surface Interactions Due to Ablation of High-Speed Vehicles," J. Spacecr. Rockets, **53**(3), pp. 538–548.
[61] Chinnappan, A. K., and Kumar, R., 2016, "Modeling of High Speed Gas-Granular Flow over a 2D Cylinder in the Direct Simulation Monte-Carlo Framework," Granul. Matter, **18**(3), pp. 1–10.
[62] Ge, W., Marquez, R., Modest, M. F., and Roy, S. P., 2015, "Implementation of High-Order Spherical Harmonics Methods for Radiative Heat Transfer on OPENFOAM," J. Heat Transfer, **137**(5), pp. 1–9.
[63] Ren, T., Modest, M. F., and Roy, S., 2018, "Monte Carlo Simulation for Radiative Transfer in a High- Pressure Industrial Gas Turbine Combustion Chamber," J. Eng. Gas Turbines Power, **140**(5).
[64] Roy, S. P., Cai, J., and Modest, M. F., 2017, "Development of a Multiphase Photon Monte Carlo Method for Spray Combustion and Its Application in High-Pressure Conditions," Int. J. Heat Mass

Transf., **115**(December), pp. 453–466.
[65] Ren, T., and Modest, M. F., 2013, "A Hybrid Wavenumber Selection Scheme for Line-By-Line Photon Monte Carlo Simulations in High-Temperature Gases," J. Heat Transfer, **135**(8), p. 084501.
[66] Singh, N., and Schwartzentruber, T., 2018, "Nonequilibrium Internal Energy Distributions during Dissociation," Proc. Natl. Acad. Sci. U. S. A., **115**(1), pp. 47–52.
[67] Schwartzentruber, T. E., Grover, M. S., and Valentini, P., 2018, "Direct Molecular Simulation of Nonequilibrium Dilute Gases," J. Thermophys. Heat Transf., **32**(4), pp. 892–903.
[68] Feldick, A. M., Modest, M., and Levin, D. A., 2008, "Closely Coupled Flowfield-Radiation Interactions for Flowfields Created during Hypersonic Reentry," 40th Thermophys. Conf., (June), pp. 1–12.
[69] Li, Z., Sohn, I., Levin, D. A., and Modest, M. F., 2011, "Application of DSMC Electronic Excitation Modeling to Radiation Calculation of Hypersonic Reentry Flows," AIP Conf. Proc., **1333**(PART 1), pp. 1118–1123.
[70] Sohn, I., Bansal, A., Levin, D. A., and Modest, M., 2010, "Advanced Radiation Calculations of Hypersonic Reentry Flows Using Efficient Databasing Schemes," J. Thermophys. Heat Transf., **24**(3), pp. 623–637.
[71] Bhagat, A., Gijare, H., and Dongari, N., 2019, "Implementation of Knudsen Layer Phenomena in Rarefied High-Speed Gas Flows," J. Aerosp. Eng., **32**(6), p. 04019100.
[72] Gijare, H., Bhagat, A., and Dongari, N., 2019, "Effect of Knudsen Layer on the Heat Transfer in Hypersonic Rarefied Gas Flows," Int. J. Therm. Sci., **142**(August 2018), pp. 134–141.
[73] Kumar, R., and Chinnappan, A. K., 2017, "Development of a Multi-Species, Parallel, 3D Direct Simulation Monte-Carlo Solver for Rarefied Gas Flows," Comput. Fluids, **159**, pp. 204–216.
[74] Gavasane, A., Agrawal, A., and Bhandarkar, U., 2018, "Study of Rarefied Gas Flows in Backward Facing Micro-Step Using Direct Simulation Monte Carlo," Vacuum, **155**(March), pp. 249–259.
[75] Bird, G. A., 2013, *The DSMC Method*.
[76] Bansal, A., 2011, "K-Distribution Models For Gas Mixture in Hypersonic Nonequilibrium Flows," The Pennsylvania State University.
[77] Borgnakke, C., and Larsen, P. S., 1975, "Statistical Collision Model for Monte Carlo Simulation of Polyatomic Gas Mixture," J. Comput. Phys., **18**, pp. 405–420.
[78] Burn, R., 2012, *High Temperature Phenomena in Shock Waves*.
[79] Liechty, D. S., 2014, *Extension of a Kinetic Approach to Chemical Reactions to Electronic Energy Levels and Reactions Involving Charged Species with Application to DSMC Simulations*.
[80] Bird, G. A., 2012, "Setting the Post-Reaction Internal Energies in Direct Simulation Monte Carlo Chemistry Simulations," Phys. Fluids, **24**(12), p. 127104.
[81] Liechty, D. S., and Lewis, M. J., 2011, "Extension of a Kinetic-Theory Approach for Computing Chemical-Reaction Rates to Reactions with Charged Particles," *27th International Symposium on Rarefied Gas Dynamics*, pp. 1239–1244.
[82] Bird, G. A., 2011, "The Q-K Model for Gas-Phase Chemical Reaction Rates," Phys. Fluids, **23**(10), p. 106101.
[83] Boyd, I. D., and Schwartzentruber, T. E., 2017, *Nonequilibrium Gas Dynamics and Molecular Simulation*, Cambridge University Press, Cambridge.
[84] Goldsworthy, M., and Macrossan, M., 2009, *Vibrational Degrees of Freedom in the Total Collision Energy DSMC Chemistry Model*, Brisbane.
[85] Tseng, K.-C., Wu, J.-S., and Boyd, I. D., 2006, "Simulations of Re-Entry Vehicles by Using DSMC with Chemical-Reaction Module," 14th AIAA/AHI Sp. Planes Hypersonic Syst. Technol. Conf.
[86] Dhurandhar, S. N., and Bansal, A., 2017, "Relaxation and Reaction Model for Gases in Rarefied Flows," Proc. 24th Natl. 2nd Int. ISHMT-ASTFE Heat Mass Transf. Conf. (IHMTC-2017),.
[87] Kumbhakarna, N., Chowdhury, A., and Thynell, S. T., 2009, "Modeling of RDX/TAGzT Propellant Combustion with Detailed Chemical Kinetics," 45th AIAA/ASME/SAE/ASEE Jt. Propuls. Conf. Exhib., (August), pp. 1–14.
[88] Braun, R. D., and Manning, R. M., 2007, "Mars Exploration Entry, Descent, and Landing

Challenges," J. Spacecr. Rockets, **44**(2), pp. 310–323.
[89] D. E. Florence, 1981, "Aerothermodynamic Design Feasibility of a Generic Planetary Aerocapture/Aeromaneuver Vehicle," AlAA 16th Thermophys. Conf., pp. 1–18.
[90] Takehiko, S., 1972, *Tables of Molecular Vibrational Frequencies Consolidated Volume I*.
[91] Atkins, P. W., and De Paula, J., 2006, *Atkins' Physical Chemistry*, W.H. Freeman.
[92] Dietrich, S., and Boyd, I. D., 1996, "Scalar and Parallel Optimized Implementation of the Direct Simulation Monte Carlo Method," J. Comput. Phys., **126**(2), pp. 328–342.
[93] Ivanovt, M. S., Markelovf, G. N., and Gimelshein, S. F., 1998, "Statistical Simulation of Reactive Rarefied Flows: Numerical Approach and Applications," 7th AIAA/ASME Jt. Thermophys. Heat Transf. Conf., pp. 1–19.
[94] LeBeau, G. J., and Lumpkin, F. E., 2001, "Application Highlights of the DSMC Analysis Code (DAC) Software for Simulating Rarefied Flows," Comput. Methods Appl. Mech. Eng.
[95] Wu, J. S., Tseng, K. C., Lee, U. M., and Lian, Y. Y., 2005, "Development of a General Parallel Three-Dimensional Direct Simulation Monte Carlo Code," AIP Conf. Proc., **762**, pp. 559–564.
[96] Matsumoto, Y., and Tokumasu, T., 1997, "Parallel Computing of Diatomic Molecular Rarefied Gas Flows," Parallel Comput., **23**(9), pp. 1249–1260.
[97] Koura, K., and Matsumoto, H., 1991, "Variable Soft Sphere Molecular Model for Inverse-Power-Law or Lennard-Jones Potential," Phys. Fluids A, **3**(10), pp. 2459–2465.
[98] Boyd, I. D., 2002, "Relaxation of Discrete Rotational Energy Distributions Using a Monte Carlo Method," Phys. Fluids A Fluid Dyn., **5**(9), pp. 2278–2286.
[99] Parker, J. G., 1959, "Rotational and Vibrational Relaxation in Diatomic Gases," Phys. Fluids Fluids, **2**(4), pp. 449–462.
[100] Millikan, R. C., and White, D. R., 1963, "Systematics of Vibrational Relaxation Systematics of Vibrational Relaxation," J. Chem. Phys., **38**, pp. 3209–3213.
[101] Park, C., 1984, "Problems of Rate Chemistry in the Flight Regimes," AlAA 19th Thermophys. Conf., pp. 1–11.
[102] Gimelshein, S. F., Gimelshein, N. E., Levin, D. A., Ivanov, M. S., and Wysong, I. J., 2004, "On the Use of Chemical Reaction Rates with Discrete Internal Energies in the Direct Simulation Monte Carlo Method," Phys. Fluids, **16**(7), pp. 2442–2451.
[103] Bondar, Y., and Ivanov, M., 2007, "DSMC Dissociation Model Based on Two-Temperature Chemical Rate Constant," 45th AIAA Aerosp. Sci. Meet. Exhib., (January), pp. 1–21.
[104] Bird, G. A., 2005, "The DS2V/3V Program Suite for DSMC Calculations," AIP Conf. Proc., **762**(1), pp. 541–546.
[105] Moss, J. N., Glass, C. E., and Greene, F. A., 2006, "DSMC Simulations of Apollo Capsule Aerodynamics for Hypersonic Rarefied Conditions," 9th AIAA/ ASM Thermophys. Heat Transf. Conf., (June), pp. 5–8.
[106] Ozawa, T., Zhong, J., Levin, D. A., Boger, D., and Wright, M., 2007, "Modeling of the Stardust Reentry Flows with Ionization in DSMC," 45th AIAA Aerosp. Sci. Meet. Exhib., (January), pp. 9–12.
[107] Lebé, A., hot, Echegut, P., Dudeck, M., Renault, T., Pellerin, S., and Lago, V., 2008, "Entry Conditions in Planetary Atmospheres: Emission Spectroscopy of Molecular Plasma Arcjets," J. Thermophys. Heat Transf., **15**(2), pp. 168–175.
[108] Da Silva, M. L., Passarinho, F., and Dudeck, M., 2006, "Modelling of a CO2-N2 Plasma Flow in a Supersonic Arcjet Facility," J. Thermophys. Heat Transf., **20**(4), pp. 680–688.
[109] Barbosa, E., Lopez, B., Dudeck, M., Kaminska, A., Izrar, B., Dudeck, E. B. B. L. M., Kaminska, B. I.-A., and E. Barbosa, B. L. M. D., 2007, "Numerical Simulation of Nonequilibrium Hypersonic Flow in an Arcjet Nozzle: Application to Mars Atmosphere Entry Simulation," 8th Int. Symp. Exp. Comput. Aerothermodyn. Intern. Flows, p. 10.
[110] Glass, C. E., and Gnoffo, P. A., 2001, "A 3-D Coupled CFD-DSMC Solution Method with Application to the Mars Sample Return Orbiter," AIP Conf. Proc., **585**, pp. 723–729.
[111] Cheatwood, F. M., and Gnoffo, P. A., 1996, "User's Manual for the Langley Aerothermodynamic

Upwind Relaxation Algorithm (LAURA)," NASA Tech. Memo., **4674**.
[112] Drake, D. J., and Popovi, S., 2009, "Kinetic Description of Martian Atmospheric Entry Plasma," IEEE Trans. PLASMA Sci., **37**(8), pp. 1646–1655.
[113] Nizenkov, P., Pfeiffer, M., Mirza, A., and Fasoulas, S., 2017, "Modeling of Chemical Reactions between Polyatomic Molecules for Atmospheric Entry Simulations with Direct Simulation Monte Carlo," Phys. Fluids, **29**(7), p. 077104.
[114] Sebastião, I. B., and Alexeenko, A., 2016, "Consistent Post-Reaction Vibrational Energy Redistribution in DSMC Simulations Using TCE Model," Phys. Fluids, **28**(10), p. 107103.
[115] White, C., Borg, M. K., Scanlon, T. J., Longshaw, S. M., John, B., Emerson, D. R., and Reese, J. M., 2017, "DsmcFoam+: An OpenFOAM Based Direct Simulation Monte Carlo Solver," Comput. Phys. Commun., **224**, pp. 22–43.
[116] Hindelang, F. J., 1967, "Coupled Vibration and Dissociation Relaxation Behind Strong Shock Waves in Carbon Dioxide," Nasa Tr R-253, (February 1967).
[117] Thorne, L. R., Branch, M. C., Chandler, D. W., Kee, R. J., and Miller, J. A., 1986, "Hydrocarbon/Nitric Oxide Interactions in Low-Pressure Flames," Symp. Combust., **21**(1), pp. 965–977.
[118] Johnston, H. S., 1968, *Gas Phase Reaction Kinetics of Natural Oxygen Species*.
[119] Dunn, M. G., and Kang, S.-W., 1973, *Theoretical and Experimental Studies of Reentry Plasmas*.
[120] Park, C., and Menees, G. P., 1978, "Odd Nitrogen Production by Meteoroids," J. Geophys. Res., **83**(C8), p. 4029.
[121] Hanson, R. K., and Baganoff, D., 1971, "Shock-Tube Study of Nitrogen Dissociation Rates Using Pressure Measurements," 4th Fluid Plasma Dyn. Conf., **10**(2), pp. 211–215.
[122] Koshi, M., Bando, S., Saito, M., and Asaba, T., 1979, "D I S S O C I a T I O N of Nitric O X I D E in S H O C K Waves," Symp. Combust. Elsevier, **17**, pp. 553–562.
[123] Thielen, K., and Roth, P., 1984, "Resonance Absorption Mesurement of N and O Atoms in High Temperature NO Dissociation and Formation Kinetics," Symp. Combust., **20**(1), pp. 685–693.
[124] Tsang, W., and Herron, J. T., 1991, "Chemical Kinetic Data Base for Propellant Combustion I. Reactions Involving NO, NO2, HNO, HNO2, HCN and N2O," J. Phys. Chem. Ref. Data, **20**(4), pp. 609–663.
[125] Hanson, R. K., 1974, "Shock-Tube Study of Carbon Monoxide Dissociation Kinetics," J. Chem. Phys., **4970**, pp. 4970–4976.
[126] CHACKERIAN, and Jr., C., 1971, "The Dissociation of Shock Heated Carbon Monoxide Studied by Two Wavelength Infrared Emission," Proc. 8th Int. Shock Tube Symp. 1971, **40**.
[127] Burmeister, M., and Roth, P., 1990, "ARAS Measurements on the Thermal Decomposition of CO2 behind Shock Waves," AIAA J., **28**(3), pp. 402–405.
[128] Davies, W. O., 1965, "Carbon Dioxide Dissociation at 6000° to 11 000°K," J. Chem. Phys., **43**(8), pp. 2809–2818.
[129] G.G.Chernyi, 2004, "Physical and Chemical Processes in Gas Dynamics: Cross Sections and Rate Constants for Physical and Chemical Processes Volume I," AIAA J., **197**, pp. 85–121.
[130] Baulch, D. L., Pilling, M. J., Cobos, C. J., Cox, R. A., Frank, P., Hayman, G., Just, T., Kerr, J. A., Murrells, T., Troe, J., Walker, R. W., and Warnatz, J., 2005, "Evaluated Kinetic Data for Combustion Modeling. Supplement II," J. Phys. Chem. Ref. Data, **34**(3), pp. 1–641.
[131] Ibragimova, L. B., 1991, "Recommended Rate Constants of CO + O2 - Reversible - CO2 + O Reactions," Khim. Fiz., **10**, pp. 307–310.
[132] Charles Baber, S., and Dean, A. M., 1974, "Reaction of Atomic Oxygen with Carbon Dioxide behind Reflected Shock Waves," J. Chem. Phys., **60**(1), pp. 307–313.
[133] Warnatz, J., 1984, *Rate Coefficients in the C/H/O System*, Springer, New York, NY.
[134] Gupta, R. N., Yos, J. M., and Thompson, R. A., 1989, "A Review of Reaction Rates and Thermodynamic and Transport Properties for the 11-Species Air Model for Chemical and Thermal Nonequilibrium Calculations to 30000 K," Nasa Tech. Memo., (February), p. 69.
[135] Bortner, M. H., 1969, "A Review of Rate Constants of Selected Reactions of Interest in Re-Entry

Flow Fields in the Atmosphere," Bur. Stand. (U.S.), Tech. Note, **484**.
[136] Monat, J. P. J., Hanson, R. K., and Kruger, C. H. C., 1979, "Shock Tube Determination of the Rate Coefficient for the Reaction N 2+ O→ NO+ N," Symp. Combust., **17**(1), pp. 543–552.
[137] Suzuki, T., Furudate, M., and Sawada, K., 2002, "Trajectory-Based Heating Analysis for the Stardust Sample Return Capsule," 40th AIAA Aerosp. Sci. Meet. Exhib., (January).
[138] Park, C., 2007, "Calculation of Stagnation-Point Heating Rates Associated with Stardust Vehicle," J. Spacecr. Rockets, **44**(1), pp. 24–32.
[139] Beerman, A. F., Lewis, M. J., Starkey, R. P., and Cybyk, B. Z., 2009, "Significance of Nonequilibrium Surface Interactions in Stardust Return Capsule Ablation Modeling," J. Thermophys. Heat Transf., **23**(3), pp. 425–432.
[140] Johnson, J. E., Starkey, R. P., and Lewis, M. J., 2007, "Aerothermodynamic Optimization of Reentry Heat Shield Shapes for a Crew Exploration Vehicle," J. Spacecr. Rockets, **44**(4), pp. 849–859.
[141] Otsu, H., Suzuki, K., Fujita, K., and Abe, T., 1998, "Radiative Heating Analysis around the MUSES-C Reentry Capsule at a Superorbital Speed," 7th AIAA/ASME Jt. Thermophys. Heat Transf. Conf., (1).
[142] Kim, M., Keidar, M., and Boyd, I. D., 2008, "Analysis of an Electromagnetic Mitigation Scheme for Reentry Telemetry through Plasma," J. Spacecr. Rockets, **45**(6), pp. 1223–1229.
[143] Zuppardi, G., 2018, "Effects of Chemistry in Mars Entry and Earth Re - Entry," Adv. Aircr. Spacecr. Sci., **5**(5), pp. 581–594.
[144] Ilyoup Sohn, 2011, "Modeling and Simulation of Radiation From Hypersonic Flows With Monte Carlo Methods," The Pennsylvania State University.
[145] Xu, M., Azevedo, J. L. T., and Carvalho, M. G., 2001, "Modeling of a Front Wall Fired Utility Boiler for Different Operating Conditions," Comput. Methods Appl. Mech. Eng., **190**(28), pp. 3581–3590.
[146] Vuthaluru, R., and Vuthaluru, H. B., 2006, "Modelling of a Wall Fired Furnace for Different Operating Conditions Using FLUENT," Fuel Process. Technol., **87**(7), pp. 633–639.
[147] Lautenberger, C. W., 2002, "CFD Simulation of Soot Formation and Flame Radiation."
[148] Bordbar, M. H., and Hyppänen, T., 2007, "Modeling of Radiation Heat Transfer in a Boiler Furnace," Adv. Stud. Theor. Phys., **1**(12), pp. 571–584.
[149] Modest, M. F., 2003, *Radiative Heat Transfer*, Academic Press, California.
[150] Siegel, R., and Howell, J. R., 1992, "Thermal Radiation Heat Transfer," Hemisph. Publ. Corp.
[151] Hottel, H. C., and Cohen, E. S., 1958, "Radiant Heat Exchange in a Gas-Filled Enclosure: Allowance for Nonuniformity of Gas Temperature," AIChE J., **4**(1), pp. 3–14.
[152] Hottel, H. C., and Sarofim, A. F., 1967, *Radiative Transfer*, McGraw-Hill Book Company, New York, NY.
[153] Díez, L. I., Cortés, C., and Campo, A., 2005, "Modelling of Pulverized Coal Boilers: Review and Validation of on-Line Simulation Techniques," Appl. Therm. Eng., **25**(10), pp. 1516–1533.
[154] Charette, A., Erchiqui, F., and Kocaefe, Y. S., 1989, "The Imaginary Planes Method for the Calculation of Radiative Heat Transfer in Industrial Furnaces," Can. J. Chem. Eng., **67**(3), pp. 378–384.
[155] Charette, A., Larouche, A., and Kocaefe, Y. S., 1990, "Application of the Imaginary Planes Method to Three-Dimensional Systems," Int. J. Heat Mass Transf., **33**(12), pp. 2671–2681.
[156] Andras Haidekker, 1991, "Radiation Modelling in Complex Three Dimensional Enclosures," Bibliotheque Paul-Emile Boulet.
[157] Rothman, L. S., Barbe, A., Benner, D. C., Brown, L. R., Camy-Peyret, C., Carleer, M. R., Chance, K., Clerbaux, C., Dana, V., Devi, V. M., Fayt, A., Flaud, J. M., Gamache, R. R., Goldman, A., Jacquemart, D., Jucks, K. W., Lafferty, W. J., Mandin, J. Y., Massie, S. T., Nemtchinov, V., Newnham, D. A., Perrin, A., Rinsland, C. P., Schroeder, J., Smith, K. M., Smith, M. A. H., Tang, K., Toth, R. A., Vander Auwera, J., Varanasi, P., and Yoshino, K., 2003, "The HITRAN Molecular Spectroscopic Database: Edition of 2000 Including Updates through 2001," J. Quant. Spectrosc. Radiat. Transf., **82**(1–4), pp. 5–44.

[158] Rothman, L. S., Gordon, I. E., Barber, R. J., Dothe, H., Gamache, R. R., Goldman, A., Perevalov, V. I., Tashkun, S. A., and Tennyson, J., 2010, "HITEMP, the High-Temperature Molecular Spectroscopic Database," J. Quant. Spectrosc. Radiat. Transf., **111**(15), pp. 2139–2150.
[159] Modest, M. F., 1991, "The Weighted-Sum-of-Gray-Gases Model for Arbitrary Solution Methods in Radiative Transfer," J. Heat Transfer, **113**(3), pp. 650–656.
[160] Ströhle, J., 2004, *Spectral Modelling of Radiative Heat Transfer in Industrial Furnaces*, Shaker.
[161] Taylor, P. B., Foster, P. J., and Technology, F., 1974, "The Total Emissivity of Luminous Flames," Int. J. Heat Mass Transf., **17**, pp. 1591–1605.
[162] Smith, T. F., Shen, Z. F., and Friedman, J. N., 1982, "Evaluation of Coefficients for the Weighted Sum of Gray Gases," J. Heat Transfer, **104**(November 1982), pp. 603–608.
[163] Taylor P. B., and Foster, P. J., 1975, "Some Gray Gas Weighting Coefficients for CO2-H2O-Soot Mixtures," Int. J. Heat Mass Transf., **18**, pp. 1331–1332.
[164] Denison, M. K., and Webb, B. W., 1995, "The Spectral-Line Weighted-Sum-of- Gray-Gases Model for H20/CO2 Mixtures," J. Heat Transfer, **117**(August 1995), pp. 788–792.
[165] Denison, M. K., and Webb, B. W., 1995, "The Spectral Line-Based Model in Nonisothermal Nonhomogeneous Media," J. Heat Transfer, **117**(May 1995), pp. 359–365.
[166] Denison, M. K., and Webb, B. W., 1994, "K-Distributions and Weighted-Sumof-Grey Gases: A Hybrid Model," *Tenth International Heat Transfer Conference*, Taylor & Francis, pp. 19–24.
[167] Denison, M. K., and B. W. webb, 1993, "Aa Absorption-Line Blackbody Distribution Total Gas Radiative Transfer," J. Quant. Spectrosc. Radiat. Transf., **50**(5), pp. 499–510.
[168] Denison, M. K., and Webb, B. W., 1993, "A Spectral Line-Based Weighted- Sum-of-Gray-Gases Model for Arbitrary RTE Solvers," J. Heat Transfer, **115**(November 1993), pp. 1004–1012.
[169] Zhang, H., and Modest, M. F., 2002, "Full-Spectrum k -Distribution Correlations for Carbon Dioxide Mixtures," *8th AIAA/ASME Joint Thermophysics and Heat Tran*, St. Louis, Missouri, pp. 1–8.
[170] Solovjov, V. P., and Webb, B. W., 2000, "SLW Modeling of Radiative Transfer in Multicomponent Gas Mixtures," J. Quant. Spectrosc. Radiat. Transf., **65**, pp. 655–672.
[171] Modest, M. F., and Mehta, R. S., 2004, "Full Spectrum k -Distribution Correlations for CO 2 from the CDSD-1000 Spectroscopic Databank," Int. J. Heat Mass Transf., **47**, pp. 2487–2491.
[172] Denison, M. K., and B. W. webb, 1996, "The Spectral Line Weighted-Sum-of-Grey-Gases Model—a Review," *First International Symposium on Radiation Transfer*, Begell House, Kusadasi, Turkey, pp. 193–208.
[173] Modest, M. F., 2002, "The Full-Spectrum Correlated-k Distribution for Thermal Radiation From Molecular Gas-Particulate," J. Heat Transfer, **124**(February 2002), pp. 30–38.
[174] Modest, M. F., 2003, "Narrow-Band and Full-Spectrum k -Distributions for Radiative Heat Transfer — Correlated- k vs . Scaling Approximation," J. Quant. Spectrosc. Radiat. Transf., **76**(76), pp. 69–83.
[175] Strom, B., 1980, "A Simple Heat Transfer Model for Fumaces Based on the Zoning Method," Warm-und Stoffubertragung, **13**, pp. 47–52.
[176] Maruyama, S., 1993, "Radiation Heat Transfer between Arbitrary Three-Dimensional Bodies with Specular and Diffuse Surfaces," Numer. Heat Transf. Part A Appl., **24**(2), pp. 181–196.
[177] Bansal, A., Modest, M. F., and Levin, D. A., 2011, "Multi-Scale k-Distribution Model for Gas Mixtures in Hypersonic Nonequilibrium Flows," J. Quant. Spectrosc. Radiat. Transf., **112**(7), pp. 1213–1221.
[178] Bansal, A., and Modest, M. F., 2013, "Modeling of Radiative Heat Transfer in Carbonaceous Atmospheres," J. Thermophys. Heat Transf., **27**(January), pp. 217–225.
[179] Bansal, A., and Modest, M., 2011, "Multiscale Part-Spectrum k-Distribution Database for Atomic Radiation in Hypersonic Nonequilibrium Flows," J. Heat Transfer, **133**(12), p. 122701.
[180] J., T., and A., S., 1999, "Gas IR Radiative Properties : From Spectroscopic Data to Approximate Models," Adv. Heat Transf., **33**, pp. 295–414.
[181] Solovjov, V. P., and Webb, B. W., 2015, "An Efficient Method for Modeling Radiative Transfer in

Multicomponent Gas Mixtures," J. Heat Transfer, **123**(June 2001), pp. 451–457.
[182] Wang, L., Modest, M. F., Haworth, D. C., Turns, S. R., Modest, M. F., Haworth, D. C., and Modeling, S. R. T., 2005, "Modeling Nongray Gas-Phase and Soot Radiation in Luminous Turbulent Nonpremixed Jet Flames," Combust. Theory Model., **9**(4), pp. 673–691.